UNIVERSIDAD CARLOS III DE MADRID

TESIS DOCTORAL

New Optoacoustic Spectroscopy System to Quantify and Characterize Absorbers in Turbid Media. Experimental Measurements and Analysis of Gold Nanoparticles for Biomedical Applications

Autor:
Vincent Cunningham

Director:
Horacio Lamela Rivera

DEPARTAMENTO DE TECNOLOGÍA ELECTRÓNICA

Leganés, Octubre 2010

TESIS DOCTORAL

NEW OPTOACOUSTIC SPECTROSCOPY SYSTEM TO QUANTIFY AND CHARACTERIZE ABSORBERS IN TURBID MEDIA. EXPERIMENTAL MEASUREMENTS AND ANALYSIS OF GOLD NANOPARTICLES FOR BIOMEDICAL APPLICATIONS

Autor: Vincent Cunningham

Director: Horacio Lamela Rivera

Firma del Tribunal Calificador:

Firma

Presidente:

Vocal:

Vocal:

Vocal:

Secretario:

Calificación:

Leganés, de de

Acknowledgements

I would first like to express my sincere gratitude to my thesis director, Professor Horacio Lamela, who has been my supervisor since the beginning of my work here in the Universidad Carlos III de Madrid. He has provided me with numerous and crucial scientific and technical discussions, important advice and constant encouragement without which I would not have been able to carry out the work presented here. I appreciate all his contributions of time and ideas.

The members of the optoelectronics and laser technology group have contributed immensely to my professional time at the Carlos III university, especially fellow group members and postgraduate students Rui Lemos, Cristina de Dios and Daniel Gallego who have stuck it out with me and have been a source of kindness and friendship.

I would also like to thank all personnel of the Department of Tecnología Electroníca, at the Universidad Carlos III de Madrid, where I have carried out my teaching activities.

I am indebted to both my Irish and Spanish families, to my parents Denis & Padrigin and Francisco & Reyes for their constant and unequivocal support and encouragement. To my brothers and sisters John, Frank, Francis, Oscar, Jennifer, Deirdre and their partners, to my nieces Emily, Julia, Beibhinn and especially my godson Jack.

Finally, I would like to express special thanks to my wife and best friend Virginia for her love, patience and encouragement whom has lived through this experience with me. Without you, I would never be in the position I am today.

Agradecimientos

Primero me gustaría agradecer sinceramente a mi director de tesis Profesor Horacio Lamela, el cual ha supervisado y dirigido para mí este gran reto desde que empecé a trabajar aquí en la Universidad Carlos III de Madrid. Ya que gracias a innumerables charlas y reuniones científicas-técnicas, las cuales han conllevado grandes consejos y su apoyo constante. Que en su total conjunto como resultado ha sido este trabajo. Siento un gran reconocimiento por su dedicación, su tiempo y sus ideas.

A los miembros del grupo de Optoelectrónica y Tecnología Láser que han contribuido ayudándome profesionalmente en mi tiempo en la Universidad. Especialmente a mis compañeros del postgraduado Rui Lemos, Cristina de Dios y Daniel Gallego los cuales han compartido conmigo estos años y han sido una fuente de compañerismo y amistad.

Me gustaría también dar gracias al personal del Departamento de Tecnología Electrónica de la Universidad Carlos III, donde he realizado mis actividades de docencia.

Quería decir a mi familia Irlandesa y Española que estoy en deuda con ellos por el apoyo incondicional que me han mostrado. A mis padres Denis & Padrigin y Francisco & Reyes por su constante y alentadora fuerza y firmeza. A mis hermanos y hermanas John, Frank, Francis, Oscar, Jennifer, Deirdre, y a sus parejas, a mis sobrinas Emily, Julia, Beibhinn y especialmente mi ahijado Jack.

Finalmente, me gustaría expresar mi sincera gratitud a mi mujer y mejor amiga Virginia, por su amor, paciencia y apoyo, quien ha vivido esta experiencia junto a mi. Sin ti no estaría donde estoy hoy.

Abstract

The limited penetration depth of optical energy in biological media is primarily due to the high level of optical scattering. This optical attenuation places an upper limit on optical, diagnostic, and therapeutic techniques for in *in-vivo* applications. The optoacoustic technique combines the unique advantages of light and sound, providing high levels of contrast, while maintaining the spatial resolution of acoustic techniques. The importance of colloidal gold solutions, as optical contrast agents in optoacoustic biomedical applications, is to increase the absorption of optical energy in areas where scattering is dominant and has prompted the study presented in this thesis on their characterization and quantification.

It has been demonstrated that the acoustic transients generated from the optical irradiation are directly proportional to the wavelength dependent absorbed optical energy. Advantage has been taken of this fact to design two separate optoacoustic schemes. The first has been implemented to quantify the optical absorption, at a single laser wavelength, of spherical gold nanoparticles embedded within a medium that simulates the high scattering nature of soft tissue. The second has been designed to obtain the spectroscopic profile of such gold nanostructures. The results obtained from the optoacoustic analysis are compared to those from a reference measurement scheme, based on collimated optical transmission, which is in parallel and under the same conditions. This comparative analysis has confirmed the interest for the proposed technique of optoacoustics for laser spectroscopy of gold nanoparticles.

In this thesis results obtained, for the first time, on the quantification and spectroscopic analysis of gold nanoparticles embedded in a liquid phantom using the optoacoustic technique are presented. The results have been confirmed by the reference measurement scheme and an offline commercial spectrophotometer. To further demonstrate the potential of the optoacoustic technique, information regarding the position and dimensions of the absorbing solutions have been extracted from measurements. The spectroscopic analysis has been carried out in steps of 5 nm over the complete wavelength range from 450 nm to 650 nm for a spherical gold nanoparticle solution and 410 nm to 1000 nm for a gold nanorod solution. This research work has opened up new lines of investigation in the field of monitorization of nanoparticle contrast agents embedded in biological media for optoacoustic diagnostics and biomedical applications.

Resumen

La limitación que existe en la profundidad de penetración de la energía óptica en medios biológicos se debe en principalmente al alto nivel de scattering (dispersión) óptico que éstos presentan. Esta atenuación óptica impone un límite superior que condiciona el uso de técnicas ópticas tanto en el campo del diagnóstico como en aplicaciones terapéuticas *in vivo*. La técnica optoacústica combina las ventajas que tienen la luz y el sonido, ofreciendo altos niveles de contraste, a la vez que garantiza la resolución temporal que ofrecen las técnicas acústicas. Las soluciones coloidales de oro permiten aumentar la absorción de la energía óptica. Este efecto puede ser utilizado como agente de contraste óptico en las técnicas optoacústicas donde hay medios con un alto nivel de scattering óptico. Este fenómeno ha motivado su caracterización y cuantificación en esta tesis.

En esta tesis se ha demostrado que los transitorios acústicos generados a partir de la irradiación óptica son directamente proporcionales a la energía óptica absorbida y a su longitud de onda. Aprovechando este hecho, se ha diseñado dos sistemas optoacústicos. El primero se ha implementado con el objetivo de cuantificar la absorción óptica, en una única longitud de onda, de las nanopartículas esféricas de oro embebidas en un medio con alto nivel de scattering que modela las propiedades ópticas de tejidos blandos. El segundo esquema ha sido diseñado para conseguir el perfil espectroscópico de dichas nanopartículas de oro. Los resultados obtenidos del análisis optoacústico se han comparado con los resultados proporcionados por un sistema de medida de referencia, basado en la transmisión óptica, que funciona en paralelo con el sistema optoacústico y bajo las mismas condiciones experimentales. Este estudio comparativo ha confirmado el interés de las técnicas optoacústicos para aplicaciones en espectroscopia laser para nanopartículas.

En este trabajo de tesis se presenta por primera vez resultados sobre la cuantificación y el análisis espectroscópico de nanopartículas de oro embebidas en un fantom liquido utilizando técnicas optoacústicos. Los resultados han sido confirmados por las medidas de referencia y también por los datos ofrecidos por un espectrofotómetro comercial. Para profundizar en el potencial de la técnica optoacústica, se ha conseguido extraer información relacionada con las dimensiones y posición de la solución absorbente partiendo de las medidas realizadas. El análisis espectroscópico se ha llevado a cabo realizando adquisiciones en pasos de 5 nm a lo largo del rango de longitudes de onda que va desde los

450 nm hasta los 650 nm para nanopartículas esféricas y en el rango que se extiende entre los 410 nm y los 1000 nm para la solución de nanorods de oro en un medio de alto nivel de scattering óptico. Este trabajo de tesis doctoral ha abierto nuevas líneas de investigación en el campo de la monitorización de nanopartículas como agentes de contraste óptico embebidos en medios biológicos para el diagnóstico mediante técnicas optoacústicos y aplicaciones biomédicas.

Chapter 3

Chapter 4

Chapter 1.

Introduction

The optoacoustic affect was first reported by Alexander Graham Bell in 1881 [1.1], stating *"…thin disks of very many substances emitted sounds when exposed to the action of a rapidly interrupted beam of sunlight…"*. The sound produced by the materials resulted from the absorption of solar energy.

Since Bell's first discovery of the optical to acoustic energy conversion process, the so called, optoacoustic signal generation has found a wide range of applications in diverse sectors for material characterization of solids [1.2], liquids [1.3] and gases [1.4-1.5]. Over the past 15 years the use of optoacoustics in biomedical applications has generated considerable interest [1.6-1.9]. This is due to current demands, within this sector, for harmless, real time and non-invasive diagnostic procedures which provide efficient therapeutic procedures.

A quantitative analysis of the optical properties of biological media provides essential physiological information required for effective diagnosis. To date the most commonly used methods to determine the optical properties require invasive procedures and *in-vitro* offline techniques based on attenuation using spectrophotometry [1.10], reflectance [1.11], fluorescence spectroscopy [1.12], Raman spectroscopy [1.13] and photoacoustics [1.14]. The principal reason for this *in-vitro* quantification is due to the embedded nature of the analytes of interest and the harsh optical environment that surrounds them. The potential benefits of an *in-vivo* non-invasive method would be significant and help speed up therapeutic response times.

Absorption and scattering are the two physical phenomenons that affect light propagation in biological media. Although both parameters are important, scattering is the dominant mechanism in healthy soft tissue [1.15]. Both of these optical attenuation parameters in biomaterials are wavelength dependent [1.16]. This is because the

absorption spectrum in tissues by chromophores is a result of their molecular composition; molecules absorb photons when the photons energy matches an interval between internal energy states. Owing to this fact, each chromophore has a unique spectral signature which provides spectroscopic calibration and allows changes in the absorption spectrum to be related to changes in their concentration [1.17].

In-vivo quantification of the spectral characteristics of tissue chromophores has been performed using *Diffuse Optical Spectroscopy* (DOS). This method can simultaneously measure both light absorption and scattering in turbid media and biomaterials [1.18-1.22]. The DOS technique is generally carried out within the visible to near-infrared (NIR), where a diagnostic optical window exists that contains the most important chromophores. DOS has provided information regarding the concentration of functional tissues, hemodynamics, water content, and bulk lipids. Clinical trials using this technique for the detection of breast cancer have been reported for penetration depths of up to 1 cm [1.23]. Such procedures, based on homodyne and heterodyne detection schemes, rely on detecting both the amplitude and phase of a highly attenuated modulated optical signal using high sensitive optical detectors (photomultiplier tubes PMT's or avalanche photodiodes APD's). The optical attenuation of multiple-scattering healthy tissue imposes the main obstacle to the penetration depth, thus limiting the scope of this technique [1.23].

One of the major advantages of optoacoustics over the aforementioned technique is that the penetration depth is within the centimeter range [1.24], with reports of depths beyond 5 cm in chicken breast optical phantoms [1.8]. Non-invasive *in-vivo* trials have been reported on the visualization of the dynamic and functional properties of the nervous system on rat models [1.25]. Clinical trials using optoacoustic tomography were capable of visualizing 18 out of 20 malignant lesions suspected from mammography and ultrasound images which were confirmed after biopsy [1.26]. Recent *in-vivo* advances in optoacoustic imaging have demonstrated three-dimensional whole body imaging of mice [1.27-1.28].

Optoacoustic image contrast relies on the difference between the optical absorption properties of tissue abnormalities and the surrounding healthy tissue. For early cancer detection during the vascularization process, commonly referred to as angiogenesis, the optical properties of healthy and unhealthy tissue are similar, thus hampering the

detection process [1.29-1.30]. With the aid of cancer targeted optical contrast agents that increase the absorption of the laser energy, the optoacoustic signal can be enhanced [1.31-1.33]. *In-vivo* trials using a combination of optoacoustics and gold nanorods have been performed on mice and have demonstrated this increase in image contrast [1.34-1.36].

The most important feature of gold nanoparticle solutions is based on their optical properties where this is dependent on their geometrical structure [1.37-1.38]. During synthesis, the absorption or scattering of the particle solutions can be tuned to specific wavelengths within the visible and near infrared (NIR) [1.39-1.40]. The majority of results presented to date are qualitative, and there is a lack of *in-vivo* quantitative studies on the optical properties, thus concentration of nanoparticle contrast agents. This shortage of information has been highlighted in [1.41] and has motivated the research work presented in this thesis. This limitation has also been emphasized for other biological chromophores embedded within healthy soft tissue [1.42-1.43].

The ultimate goal of *in-vivo* quantitative optoacoustic spectroscopic imaging is to provide maps of the absolute concentration of chromophores, or externally administered optical contrast agents. This knowledge is of prime interest for cancer diagnosis, prognosis and therapy optimization [1.44-1.45]. Recent attempts at *in-vivo* nanorod mapping within a rat model using optoacoustic spectroscopy have been reported in [1.35], this spectral analysis has been limited to three different wavelengths (757 nm, 807 nm and 820 nm). The feasibility of the procedure has been confirmed, however, no quantitative information has been extracted.

The research work presented in this thesis is dedicated to the quantification and spectral characterization of the optical properties of gold nanoparticles embedded within a medium that simulates the high scattering nature of soft tissue. This study has involved the design of optoacoustic based characterization schemes that both quantify, and spectrally resolve, the optical absorption of nanoparticles over the wavelength range from 410 to 1000 nm in steps of 5 nm. The results obtained are compared to those from a collimated optical transmittance scheme.

In the following Chapter 2 the conceptual background of the optoacoustic measurement schemes will be presented. This includes a study of optical energy propagation in attenuating media. A discussion on optical absorption and scattering along with the key

parameters which characterize them, will be provided. This will be followed by a review of the conditions required for efficient generation of optoacoustic signals, which is based on the thermoelastic expansion caused by the optical absorption. Also in this chapter, a description is provided on both the temporal and spectral characteristics of the acoustic transients generated during optical irradiation of absorbers.

The gold nanoparticle solutions which have been characterized in this thesis will be presented in Chapter 3. The most important parameters responsible for their spectral behavior will be identified, along with a review of the most commonly used theoretical approaches, to model their behavior. Results from a numerical analysis based on Mie theory will be presented for homogeneous spherical gold nanoparticles, and, from an extension to Mie Theory derived by Gans for gold nanorods. The dependence of the particle's dimensions on the optical properties will be shown. This theoretical analysis has provided crucial experimental design parameters required to efficiently characterize the nanostructures.

In Chapter 4 the concepts behind the quantification of the optical properties of gold nanostructures using the optoacoustic signals generated will be presented. This is followed by a description of the optical phantom used. This chapter contains a descriptive review on the design of the optoacoustic based characterization schemes. The experimental setups presented make use of an additional reference collimated optical transmission measurement scheme, in parallel, and under the same experimental conditions. This has been used to provide a comparative analysis of the results obtained, and to ensure the feasibility of the optoacoustic measurements. A review of the experimental protocols for each measurement will also be made available here.

In Chapter 5 results from preliminary experimental trials on the quantification of a known pure absorber will be presented. These have been performed to demonstrate the feasibility of the optoacoustic quantification technique. This is then followed by a quantitative analysis of a specifically synthesized spherical gold nanoparticle solution, containing an absorption peak close to that of the 532 nm emission wavelength of the laser source. Finally the results from a similar nanostructure absorber, embedded within a highly scattering media which simulates the scattering properties of healthy soft tissue, will be presented. Good agreement has been observed between the results from

the optoacoustic and reference schemes, thus enforcing the feasibility of the technique. The results obtained and presented in this chapter have been recently published [1.46].

In Chapter 6 the results from the optoacoustic spectroscopic analysis of a spherical gold nanoparticle solution, and a gold nanorod solution embedded in a liquid tissue scattering phantom, are presented. The accuracy of the optoacoustic technique to spectrally resolve the nanostructure absorbers has been demonstrated, where agreement is again observed between the optoacoustic, and reference measurement scheme. To further corroborate the results obtained, a comparative analysis with an offline commercial spectrophotometer is presented. The optoacoustic spectroscopic results from the spherical gold nanoparticles have recently been published in [1.47], and those from the nanorod solutions in [1.48]. Finally, a quantitative estimation of the spectral properties based on the properties of the system components will be presented. This thesis concludes with chapter 7 which contains a summary of the research presented, and an overview of future approaches within this field of investigation.

Chapter 2.

Tissue Optics and Optoacoustic Signal Generation Concepts

2.1. Introduction

The basic concepts surrounding the generation of acoustic transients from short pulsed optical excitation of absorbing media will be examined in this chapter. It will be shown how the properties of the optoacoustic signals are a consequence of the wavelength dependent optical attenuation of the media being irradiated. To fully understand the process of optical to acoustic conversion of embedded absorbers, such as biological abnormalities surrounded by healthy tissue, it is essential to identify the behavior of the interaction of light with such media.

Considering this, the next section of this chapter will deal with the two principal physical phenomena affecting the propagation of light. Here the key parameters associated with each process will be defined and are used to describe the diffuse nature of optical transmission in biological materials such as soft tissue. The objective of this review not only serves to introduce the mechanisms required to understand the optoacoustic signal generation process, but will also be applied in Chapter 3 to describe the tunable optical properties of optical contrast agents based on colloidal gold solutions.

It will be demonstrated that the optical properties of a medium form a crucial role in determining the conditions required for efficient conversion from optical to acoustic energy. This review will indicate the conceptual background which has formed part of the design and implementation of measurement schemes based on optoacoustics and presented in Chapter 4 of this thesis. An analysis of both the temporal and spectral properties of the acoustics transients generated will be included. Finally, this chapter concludes with a description of the most commonly used short pulsed laser sources used in optoacoustic biomedical applications.

2.2. Propagation of Optical Energy in Turbid Media

As light travels its attenuation is primarily caused by the absorption and/or scattering properties of the media, where both of these parameters are wavelength dependent. In this section, the mechanisms behind the aforementioned phenomena will be discussed, where emphasis will be placed on the propagation of light in biological media. In order to understand this process, a review of the coefficients of absorption and scattering will be presented and defined. Also included will be a description of the diffuse nature of optical propagation in media, such as biological tissues, which present multiple scattering events.

2.2.1. Optical Absorption

2.2.1.1. Light Matter Interaction

The absorption of electromagnetic radiation is the way by which the energy of a photon is taken up by matter. Absorption produces the transition of an atom, or molecule, to a higher energy level. This transition from a lower to higher level involves excitation to an excited state and requires the absorption of energy, $E = h\nu$, equal to the difference in energy, ΔE, between the two levels (see Figure 2.1).

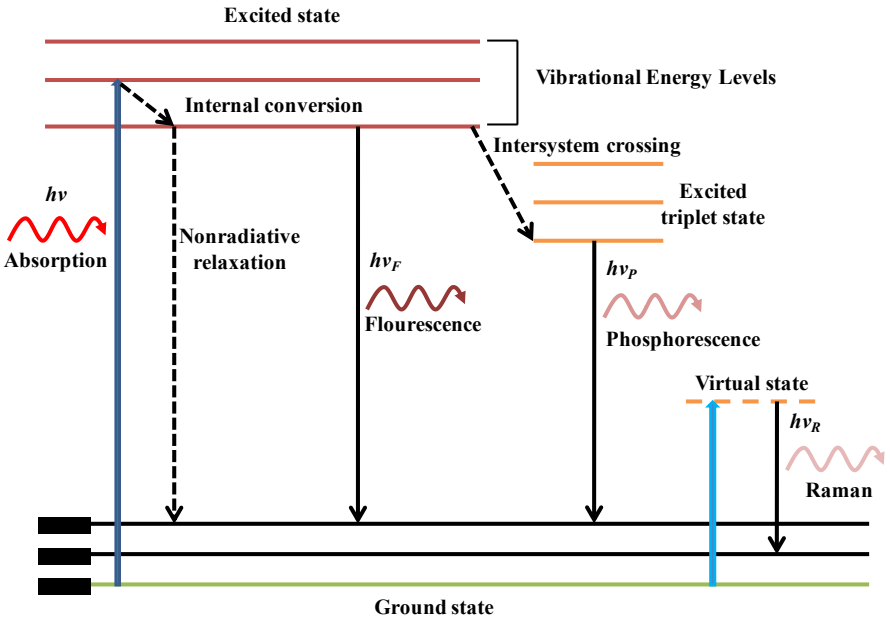

Figure 2.1 Jablonski energy level diagram showing the different energy levels and the transition from the ground state to an excited state caused by photon absorption [2.1].

When an electron is raised to an excited state, there are several routes by which it can return to the ground state. The excited electron may relax to the ground state and give off energy in the form of luminescence, i.e. another photon, producing *fluorescence* or *phosphorescence* which depends on the lifetime of the excited electron, or may also give off heat in a process known as *nonradiative relaxation*. A Jablonski energy level diagram explaining this transition between energy states is presented in Figure 2.1 [2.1]. The energy levels represent both the absorption and emission bands. The energy states can be grouped into two broad categories, *singlet states* and *triplet states*. A singlet state is one in which all of the electrons in the molecule have their spins paired. Triplet states are those in which one set of electron spin have become unpaired. Triplet states and singlet states differ significantly in their properties as well as in their energies. A triplet state will always lie lower in energy than its corresponding singlet state.

In Figure 2.1 it may be seen that fluorescence involves three different events that have differing timescales [2.1]. The excitation by a photon takes place in femtoseconds ($\sim 10^{-15}$ s) where this time is short relative to the time required for all other electronic processes and nuclear motion. The vibrational relaxation, commonly referred to as *internal conversion*, to the lowest vibrational energy level in the excited state lasts for picoseconds ($\sim 10^{-12}$ s) and does not result in the emission of a photon, i.e. nonradiative. Fluorescence emission takes in the order of nanoseconds ($\sim 10^{-9}$ s).

The phosphorescence process is similar to fluorescence, the main difference here is that the molecule makes a further transition from the lowest excited state to a metastable state by a process known as intersystem crossing (see Figure 2.1) [2.1]. Once intersystem crossing has occurred the molecule undergoes the usual internal conversion process (10^{-13} to 10^{-11} s) and falls to the zeroth vibrational level of the triplet state. Because relaxation from the metastable state to the ground state is spin-forbidden, emission occurs only when thermal energy raises the electron to a state where relaxation is allowed. As a result of this process, phosphorescence depends on temperature and has a long lifetime (10^{-4} to 10 s).

There are two types of photon scattering by a molecule, elastic and inelastic, the latter is commonly referred to as Raman scattering. Elastic scattering involves no energy exchange between the photon and the molecule, whereas Raman scattering does. In

Raman scattering, the molecule is excited to a virtual state before relaxing to an energy level of the ground state emitting a photon.

2.2.1.2. Absorption process

The absorption process is characterized by the wavelength dependent *absorption cross section*, σ_{abs} (cm^2), and the *absorption coefficient*, μ_{abs} (cm^{-1}). The former is defined as the power absorbed, P_{abs} (W), from an initially uniform plane wave with irradiance or intensity, I_0 (W/cm^2), and is given as:

$$\sigma_{abs} = \frac{P_{abs}}{I_0} \tag{2.2.1}$$

A medium with a uniform distribution of identical absorbing particles is commonly characterized by the absorption coefficient μ_{abs} (cm^{-1}) as:

$$\mu_{abs} = N\sigma_{abs} \tag{2.2.2}$$

Here N (cm^{-3}) is the number density of absorbers in the media. The absorption coefficient determines how far into a material light at a specific wavelength can penetrate before it is absorbed. The mean free path travelled by a photon prior to being absorbed is given by:

$$L_a = \frac{1}{\mu_{abs}} \tag{2.2.3}$$

Where L_a (cm) is commonly referred to as the *absorption mean free path* or *characteristic linear dimension* of the absorbing material.

Homogeneous Optically Absorbing Medium

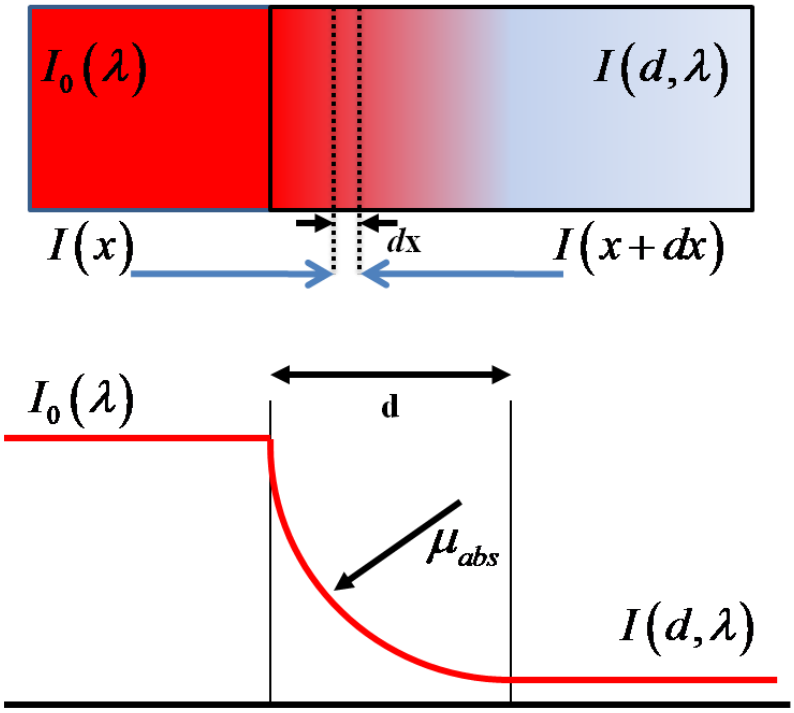

Figure 2.2 Propagation of light in a homogeneous absorbing medium with absorption coefficient μ_{abs}.

A description of the propagation of light in a homogenous absorbing medium is presented in Figure 2.2. The fraction of light intensity attenuated by the medium dI/I_0 is found experimentally to be directly proportional to the thickness of the medium where the constant of proportionality is the absorption coefficient μ_{abs} and can be expressed as:

$$\frac{dI}{I_0} = -\mu_{abs} dx \tag{2.2.4}$$

Thus, the light intensity absorbed in the interval from x to $x+dx$ is proportional to the absorption coefficient, μ_{abs}, and the optical path distance dx. The minus sign indicates a decrease in intensity. Integrating this over the thickness of the medium d,

$$\int_{I_0}^{I(d)} \frac{dI}{I} = \int_0^d -\mu_{abs} dx \tag{2.2.5},$$

gives the well known Beer's law which relates the transmitted light intensity in terms of the absorption coefficient, μ_{abs}, and the optical path distance, d [2.2]:

$$I(d) = I_0 \exp(-\mu_{abs} d) \tag{2.2.6}$$

2.2.1.3. Absorption in biological media

In biological matter the process of absorption occurs from a mixture of several different absorbers, commonly referred to as chormophores. From a spectral analysis of these chromophores, the chemical composition and concentration can be obtained providing vital diagnostic information [2.3-2.6]. By means of optical absorption, the optoacoustic technique has been used to investigate the saturation of oxygenated blood, a clear symptom of cancer growth formation [2.7-2.8] and for glucose monitoring [2.9-2.10]. Many advances are being made in therapeutic techniques based on the optical absorption of high energy laser light producing photothermal ablation of tumor cells [2.11-2.13]. In Appendix A Section A.2 more details regarding the absorption properties of human soft tissue are presented.

2.2.2. Optical Scattering

In the same manner as for absorption, the wavelength dependent scattering cross section, σ_{sca} (cm^2), and scattering coefficient, μ_{sca} (cm^{-1}), are used to quantify this process. Where the former is the ratio of scattered power, P_{sca} (W), to the intensity, I_0 (W/cm^2), of a uniform plane wave, given as:

$$\sigma_{sca} = \frac{P_{sca}}{I_0} \tag{2.2.7}$$

For a medium with a uniform distribution of identical scatterers the scattering coefficient is commonly used, where:

$$\mu_{sca} = N\sigma_{sca} \tag{2.2.8},$$

where N (cm^{-3}) is the number density of scatterers. The scattering coefficient determines how far into a material light at a specific wavelength will penetrate before it is scattered. The mean free path travelled by a photon prior to being scattered is thus given by μ_{sca}^{-1},

this is commonly referred to as the *scattering mean free path* of the material volume L_s (cm).

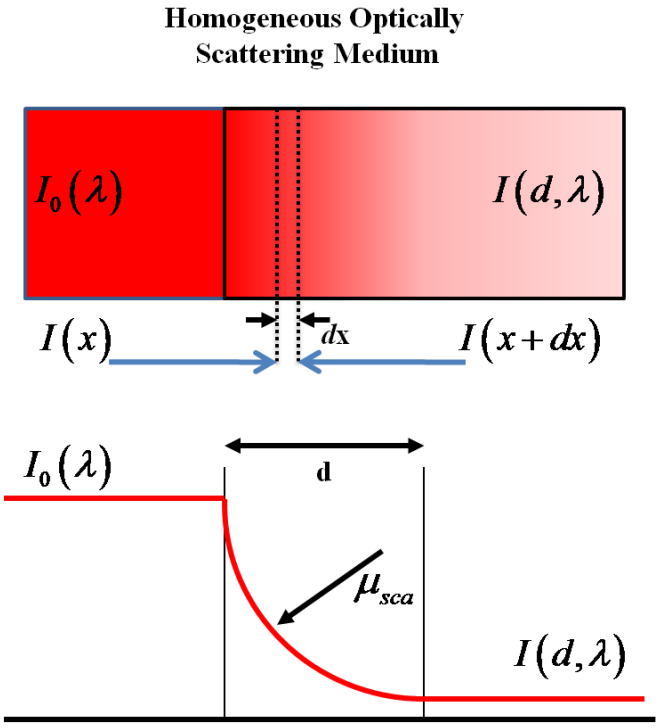

Figure 2.3 Propagation of light in a homogeneous scattering medium with scattering coefficient μ_{sca}.

An analysis of the attenuation of light in a homogeneous scattering medium, (i.e. $\mu_{sca} \gg \mu_{abs}$), may be carried out in a similar manner as before by using Beer's law for scattering as [2.14]:

$$I(d) = I_0 \exp(-\mu_{sca} d) \qquad (2.2.9).$$

2.2.2.1. Light Anisotropy

The scattering of electromagnetic radiation is directionally dependent, the angle at which the incident light is scattered is a function of the size and shape of the particle as well as the wavelength and angle of incidence. In more general terms, each type of particle will have a different scattering profile. This profile is commonly referred to as the phase function, $p(\hat{s},\hat{s}')$, and describes the amount of light scattered from the direction of the incident photon trajectory, $\hat{s}$, into the direction $\hat{s}'$, see Figure 2.4. The phase function may be treated as a probability distribution, thus the normalization

condition requires the integral of the phase function over all angles to equal unity, such that:

$$\int_{4\pi} p(\hat{s},\hat{s}')d\Omega = 1 \qquad (2.2.10),$$

where $p(\hat{s},\hat{s}')d\Omega$ is the probability that a photon incident from the $\hat{s}$ direction will leave in the differential unit of solid angle $d\Omega$ in the $\hat{s}'$ direction. The phase function will differ in general from particle to particle. For simplicity an average phase function which adequately describes the most important features of the scattering process is used. This average phase function is further constrained by assuming that the probability of scattering from one direction into another is only a function of the angle between the two directions, thus:

$$p(\hat{s},\hat{s}') = p(\hat{s}\cdot\hat{s}') = p(\cos(\theta)) \qquad (2.2.11).$$

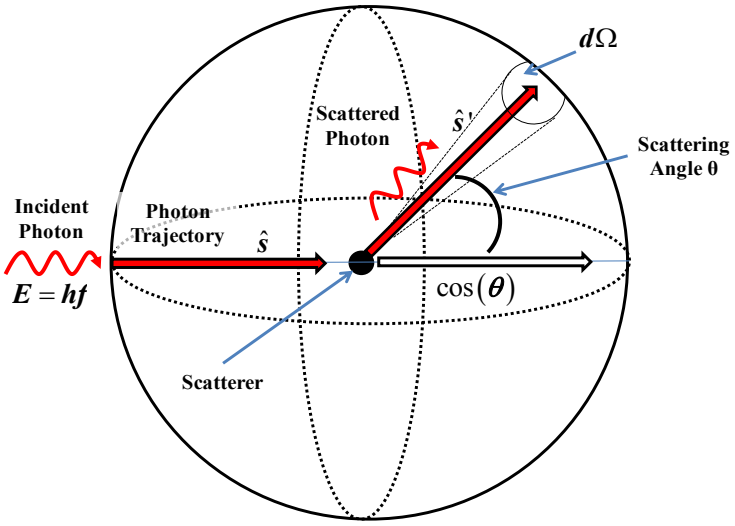

Figure 2.4 Elastic scattering of a photon.

A measure of the scattering anisotropy is given by the coefficient of anisotropy, g, which represents the average value of the cosine of the scattering angle $g = \langle\cos(\theta)\rangle$ see Figure 2.4. Using equation (2.2.11) the anisotropy parameter can be expressed as:

$$g = \langle\cos(\theta)\rangle = \int_{-1}^{1} \cos(\theta)\cdot p(\cos(\theta))\,d(\cos(\theta)) \qquad (2.2.12).$$

Values for the anisotropy factor g approaching 1, 0, and -1 describe extremely forward, isotropic, and backward scattering, respectively. Combining the scattering coefficient and the anisotropy factor gives the transport or reduced scattering coefficient:

$$\mu_{sca}^{'} = \mu_{sca}\left(1-g\right) \tag{2.2.13}.$$

This expression relates the number of anisotropic scattering steps, given by $m = 1/1-g$ required for one isotropic event. For example, if the anisotropy factor is $g = 0.9$, a typical value in biological materials, it will take an average of $m = 10$ scattering events for a population of photons to disperse isotropically, this can be seen graphically in Figure 2.5, which shows the mean free path, *mfp*, random walk of a photon over 10 different steps.

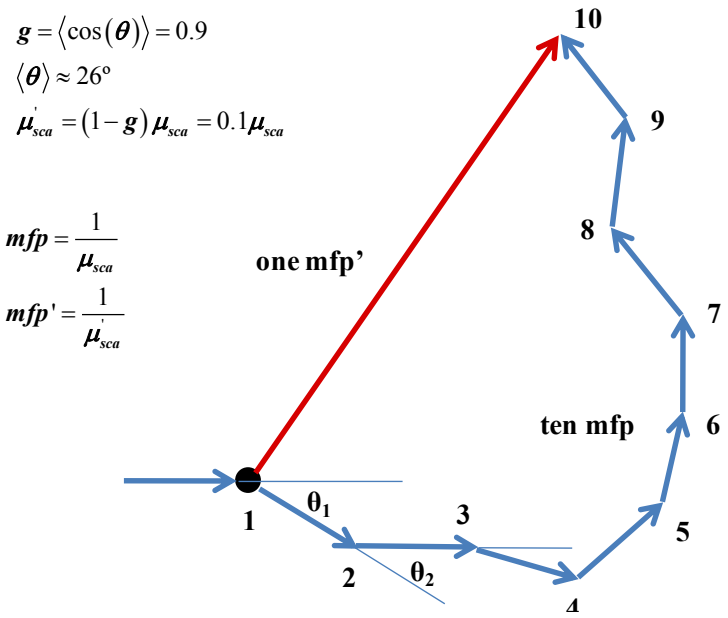

Figure 2.5 Graphical representation of the random walk of a photon in a scattering dominant medium.

The definition of the reduced scattering coefficient allows an expression for the transport attenuation, $\mu_t^{'}$ (cm^{-1}), to be defined,

$$\mu_t^{'} = \mu_{abs} + \mu_{sca}^{'} \tag{2.2.14},$$

where the reciprocal of this is the mean free transport path, $L_t = \mu_t^{'-1}$ (cm).

2.2.2.2. Scattering in Biomaterials

The optical scattering in biological tissues occurs as a result of refractive index mismatches at the boundaries of different biological tissues and fluids. Typical values for the anisotropy factor, *g*, in the majority of biological tissues ranges from 0.8 to 0.99 in the visible and near infrared [2.15-2.16]. The reduced scattering coefficient of healthy female breast tissue has been measured using a Ti:sapphire and streak camera at 800 nm and ranges from 7.2 cm^{-1} to 13.5 cm^{-1} [2.17]. The reduced scattering of a breast tumor at 690 nm and 825 nm has been measured to be 15 cm^{-1} and 12.7 cm^{-1}, respectively [2.18]. To emphasize the wavelength dependence of this attenuation term Table 2.1 has been included which indicates the reduced scattering coefficient for healthy and diseased breast tissue at three different wavelengths [2.19]. In Appendix A further details regarding the anisotropy factor and scattering coefficient in biological tissue can be found.

Tissue Type	$\mu_{sca}^{'}$ at 540 nm	$\mu_{sca}^{'}$ at 700 nm	$\mu_{sca}^{'}$ at 900 nm
Glandular (3)	24.4 ± 5.8	14.2 ± 3.0	9.9 ± 2.0
Adipose (7)	10.3 ± 1.9	8.6 ± 1.3	7.9 ± 1.1
Fibrocystic (8)	21.7 ± 3.3	13.4 ± 1.9	9.5 ± 1.7
Fibroadenoma (6)	11.1 ± 3.0	7.2 ± 1.7	5.3 ± 1.4
Carcinoma (9)	19.0 ± 5.1	11.8 ± 3.1	8.9 ± 2.6

Table 2.1 Mean and standard deviation of the reduced scattering coefficient for five different types of breast tissue at three different wavelengths. The number in the parenthesis indicates the number of tissue specimens examined for each tissue type [2.19].

2.2.3. Light Propagation Models in Biological Media

In the previous sections a discussion on the physical basis for the absorption and scattering of optical energy has been presented. This discussion has included an outline of the biological material responsible for these events. Thus far it has been assumed that the number density of particles is small enough so that the scattering fields do not interact with each other. However, in biological tissue, the scattering particle density is high so that the interaction of scattered waves between particles cannot be ignored, and multiple scattering is said to occur.

The propagation of photons in biological tissue which both absorbs and scatters light can be investigated using *Radiative Transfer Theory* (RTT). This describes the behavior of the energy radiance $L(\vec{r},t,\hat{s})$ (W m^{-2} sr^{-1}) which is defined as the energy flow per unit area per unit solid angle per unit time, where $\vec{r}$ denotes the position moving in the $\hat{s}$ direction per unit time, *t*, see Figure 2.6.

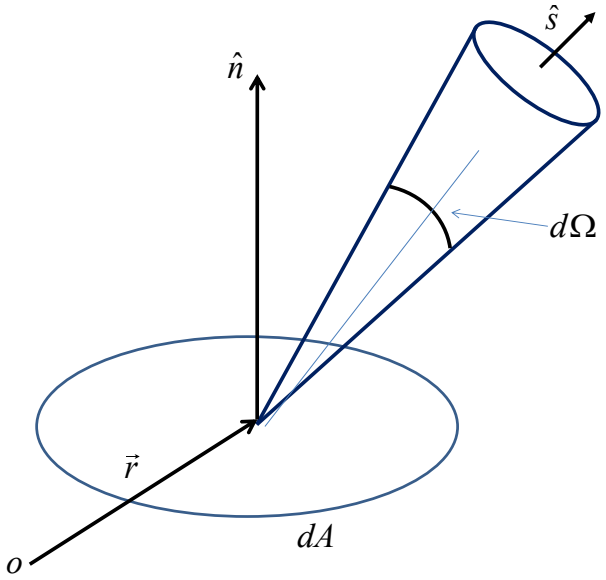

Figure 2.6 Energy flow through a differential area *dA* within a differential solid angle $d\Omega$

By integrating the energy radiance over the complete 4π solid angle the fluence rate (or Intensity) F (W m^{-2}) is obtained, which is defined as the energy flow per unit area per unit time regardless of the energy flow direction and is given as:

$$F(\vec{r},t)=\int_{4\pi} L(\vec{r},\hat{s},t)\,d\Omega \qquad (2.2.15).$$

The *Radiative Transport Equation* (RTE), also known as the Boltzmann equation, is derived using the conservation of energy law and considers all possible contributions to the energy change [2.1, 2.20]:

$$\frac{1}{v}\frac{\partial}{\partial t}L([redacted])=-\hat{s}\cdot\nabla L([redacted])-(\mu_{abs}+\mu_{sca})L([redacted])+\mu_{sca}\int_{4\pi} L(r,\hat{s}',t)\,p(\hat{s}',\hat{s})\,d\Omega'+S(r,\hat{s},t)$$

(2.2.16)

This equation can be described by considering the stationary volume shown in Figure 2.7, where ds is the differential length element of the cylinder along the propagation direction $\hat{s}$ and dA is the differential area element perpendicular to the direction $\hat{s}$. It can be seen that there are four different contributions to changes in the energy radiance $L(\vec{r},t,\hat{s})$ in the volume within a differential solid angle $d\Omega$ around the direction of propagation $\hat{s}$, these are

1. The rate of change of the energy radiance is given by $\frac{1}{v}\frac{\partial}{\partial t}L(\vec{r},\hat{s},t)$, where v is the speed of light in the medium.
2. Divergence – the loss in energy from divergence of the beam out of the solid angle, i.e. $-\nabla L(r,t,\hat{s})$,
3. Extinction – the energy loss due to absorption and scattering within the element volume, i.e. $-(\mu_{abs}+\mu_{sca})L(r,t,\hat{s})$.
4. Scattering – the energy increase within the volume occurs due to scattering from any direction $\hat{s}'$ into $d\Omega$, i.e. $+\mu_{sca}\int_{4\pi} L(\vec{r},\hat{s}',t)\,p(\hat{s}',\hat{s})\,d\Omega'$,
5. Source – the energy produced by a source in the volume element, i.e. $+S(r,t,\hat{s})$.

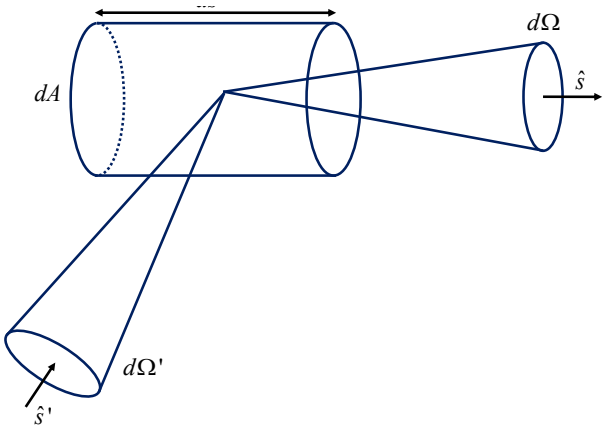

Figure 2.7 Schematic of a stationary differential cylinder volume element [2.1].

Solving the RTE equation is a complex process due to the high number of independent variables. Analytical solutions to the RTE equation that explain photon migration are commonly derived using the diffusion approximation, explained in the next section.

2.2.3.1. The Diffusion Approximation

The diffusion approximation is generally used in tissue optics as it assumes that the medium is scattering dominant (i.e. $\mu_{sca} \gg \mu_{abs}$). The scattering of photons is considered to be almost isotropic after a sufficient amount of scattering events. The theory behind the *Diffusion Limit* is important as it states that photons are able to propagate through highly scattering media, such as soft tissue, even though scattering disperses the light in a random fashion. In the diffusion process, the photons that move through a medium, do so in a series of steps of random length and direction (i.e. random walk). Each step begins with a scattering event that is equally likely to occur in any direction. When the number of photons undergoing this random walk process is large, then the density of photons can be described as a continuous function in space whose dynamics are described by the diffusion approximation.

The radiance can be expanded on a basis of spherical harmonics, where in the diffusion approximation the radiance is expanded to the first order as [2.20],

$$L(\vec{r},\hat{s},t) \approx \sum_{n=0}^{1}\sum_{m=-n}^{n} L_{n,m}(\vec{r},t)Y_{n,m}(\hat{s}) \qquad (2.2.17),$$

where $L_{n,m}$ are the expansion coefficients. The radiance is expressed using 4 terms, one for $n=0$, this is the isotropic term, and 3 terms for $m,n=1$, the anisotropic terms. Using properties of the spherical harmonics and the definitions for the fluence rate $F(\vec{r},t)$ and current density $\vec{J}(\vec{r},t)$, the isotropic and anisotropic terms are expressed as follows [2.1]:

$$L_{0,0}(\vec{r},t)Y_{0,0}(\hat{s}) = \frac{1}{4\pi}F(\vec{r},t) \qquad (2.2.18),$$

$$\sum_{m=-1}^{1} L_{1,m}(\vec{r},t)Y_{1,m}(\hat{s}) = \frac{3}{4\pi}\vec{J}(\vec{r},t)\cdot\hat{s} \qquad (2.2.19),$$

hence, using equation (2.2.17) the radiance can be approximated as,

$$L(\vec{r},\hat{s},t) = \frac{1}{4\pi}F(\vec{r},t) + \frac{3}{4\pi}[redacted]\cdot\hat{s} \qquad (2.2.20).$$

Substituting the diffusion expansion in equation (2.2.20) into the radiative transfer equation (2.2.16) and integrating over the full 4π solid angle gives the following scalar differential equation[2.21],

$$\frac{1}{v}\frac{\partial F(\vec{r},t)}{\partial t} + \mu_{abs} F(\vec{r},t) - [redacted] = S(r,t) \qquad (2.2.21).$$

Using a second assumption of diffusion theory, the fractional change in the current density $\vec{J}(\vec{r},t)$ over one transport mean free path is negligible. The vector representation of the diffusion theory reduces to Fick's law which defines the current density in terms of the gradient of fluence rate as,

$$\vec{J}(\vec{r},t) = \frac{-\nabla F(\vec{r},t)}{3\left(\mu_{abs} + \mu_{sca}^{'}\right)} \qquad (2.2.22).$$

Substitution of Fick's law into equation (2.2.21) gives the classical diffusion equation [2.20, 2.21],

$$\frac{1}{v}\frac{\partial F(\vec{r},t)}{\partial t} + \mu_{abs} F(\vec{r},t) - [redacted] = S(r,t) \qquad (2.2.23)$$

Where F is the fluence, see equation (2.2.15) and D is the diffusion constant given by [2.15]:

$$D = \frac{1}{3\left(\mu_{abs} + \mu_{sca}^{'}\right)} = \frac{1}{3\left(\mu_{abs} + (1-g)\mu_{sca}\right)} \qquad (2.2.24)$$

Here g is the anisotropy factor described in equation (2.2.12). The model takes into account the anisotropic nature of the scattering using an isotropic model. Under the condition that $\mu_{sca}^{'} \gg \mu_{abs}$ the light can be considered to propagate diffusely through the scattering medium beyond a depth d from the optical source. The solution of the diffusion equation for an infinitely short-pulsed point source, $S(\vec{r},t) = \delta(\vec{r},t)$, shows that the fluence rate presents an exponential decay with increasing depth into the medium, given as:

$$F(d,\lambda) = F_0 \exp\left(-\mu_{eff}(\lambda) d\right) \qquad (2.2.25)$$

Where the decay constant, predicted by diffusion theory, is known as the effective attenuation coefficient, μ_{eff} , and is given as [2.7]:

$$\mu_{eff} = \sqrt{\left(3\mu_{abs}\left(\mu_{abs} + \mu'_{sca}\right)\right)} \qquad (2.2.26).$$

The light penetration depth in tissues is defined as $L_{eff} = \mu_{eff}^{-1}$ (cm).

2.2.4. Diagnostic Window

A summary of the impact optically attenuating media commonly found in biological tissues is presented in Figure 2.8 over the wavelength range from 300 nm to 1200 nm. This particular region within the electromagnetic spectrum is commonly referred to as the *therapeutic window* or *diagnostic window* for optical based technologies and contains the typical spectroscopic profile of each chormophore which is important for many diagnostic purposes. Within this wavelength range, scattering is dominant over absorption, and so the propagating light becomes diffuse. The major absorbing components in soft tissues are water, lipids, oxyhaemoglobin and deoxyhaemoglobin. In the following subsections a brief description of each chormophore will be presented.

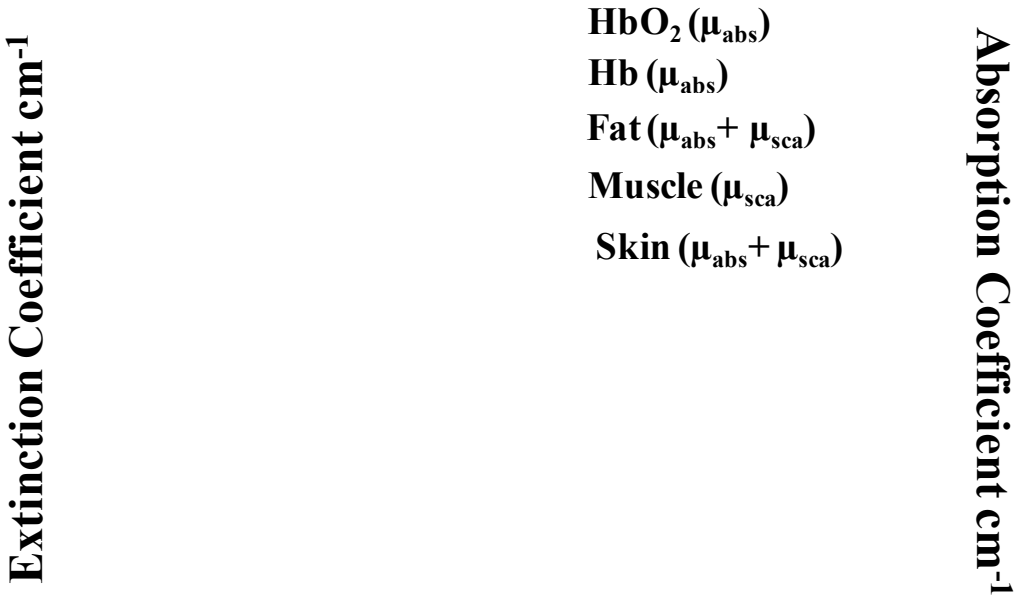

Figure 2.8 Optical absorption, μ_{abs} , and extinction, $\mu_{abs} + \mu_{sca}$ coefficients of various tissue [22].

2.2.4.1. Water

Due to the high volume of water in most biological tissues, it is considered as one of the most important chromophores. The relation between the absorption coefficient (cm^{-1}) for water versus wavelength is presented in Figure 2.9. Here it may be observed that attenuation due to water absorption is low within the visible to NIR wavelength range from 300 nm to 900 nm. Beyond 900 nm absorption rises sharply with increasing wavelength, with a spectral peak located at 970 nm. This sets an upper limit for spectroscopic and imaging methods and defines the maximum penetration depth of light in tissue. The value of the absorption coefficient, μ_{abs}, of water at 700 nm is 10^{-2} cm^{-1} and at 475 nm is 10^{-4} cm^{-1} [2.23]. For longer wavelengths the absorption coefficient increases significantly, i.e. at 15 μm it becomes $3x10^{3}$ [2.23].

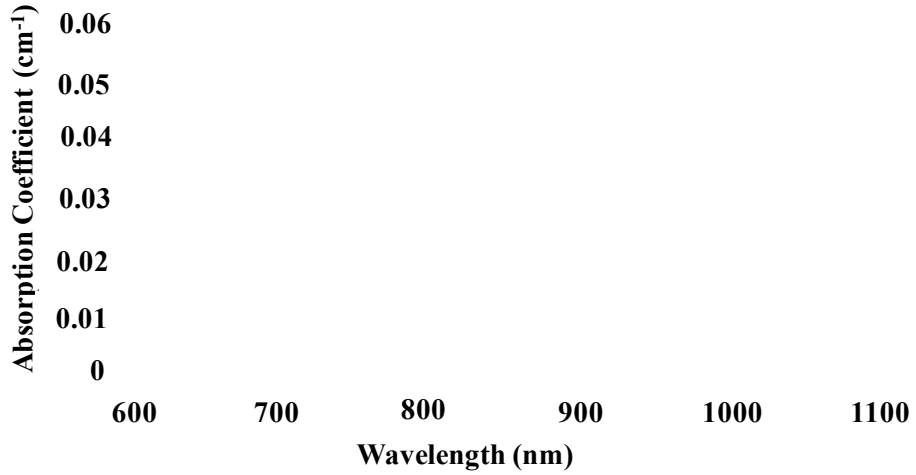

Figure 2.9 Absorption spectrum for pure water from 600 nm to 1050 nm [2.21].

2.2.4.2. Lipids (Fat)

Most of the lipid content in the body exists in the form of triglycerides (neutral fats) and is found in the subcutaneous tissues and around internal organs. The absorption spectrum of lipids is similar to that of water, but is distinguished from it by the sharp absorption band close to 930 nm and the absence of the peak at 970 nm. In Figure 2.10 the spectroscopic profile of pork fat is presented, which is thought to be largely identical to that of human lipids [2.24].

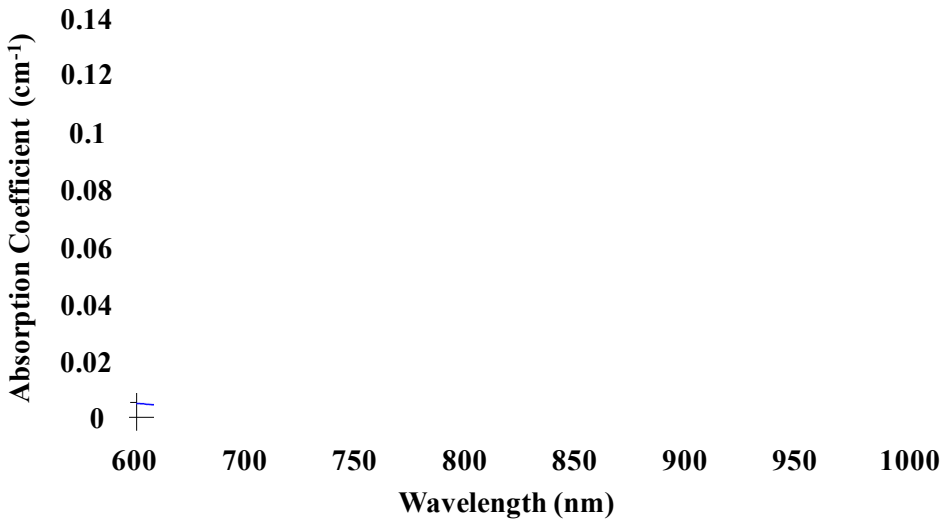

Figure 2.10 Spectrum of pork fat in the NIR from 650 nm to 1000 nm [24].

2.2.4.3. Haemoglobin

An important chormophore within the therapeutic window that is used for the detection and diagnostics of tumour growths is that of blood. In Figure 2.11 the characteristic absorption profile of both oxygenated haemoglobin (HbO_2) and deoxygenated haemoglobin (Hb) is presented. The colour of blood in the oxygenated state is bright red and deoxygenated blood is darker (see Figure 2.12). Owing to this change in colour it is natural to assume that the absorption spectrum between oxygenated and deoxygenated blood will also change.

Blood is a strong absorber for wavelengths up to 600 nm, for wavelengths longer than this the absorption of oxygenated haemoglobin is observed to drop off steeply, remaining low. The absorption of deoxygenated haemoglobin, however, does not drop dramatically. The crossover point between oxygenated and deoxygenated blood at 800 nm is referred to as the *isobestic point*. From a spectroscopic analysis of blood it is possible to calculate the concentration of both the oxyhemoglobin and the deoxyhemoglobin, providing information of the oxygen saturation (SO_2), which is the ratio of the oxyhemoglobin concentration to the total hemoglobin concentration. More details regarding the absorption and scattering of hemoglobin can be found in Appendix A.

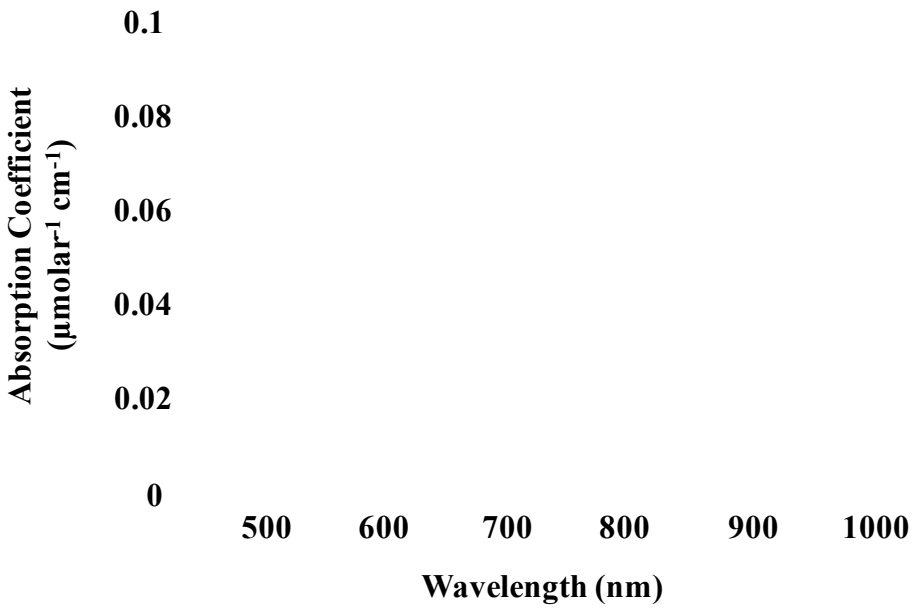

Figure 2.11 Spectrum of oxygenated and deoxygenated blood.

Figure 2.12 Deoxygenated pigs blood on the left and on the right oxygenated pigs blood.

2.3. Optical to Acoustic Energy conversion and Optoacoustic Signal Generation

A graphical description of the conversion from optical energy to acoustic energy by an optical pulse is shown in Figure 2.13. This process involves two different steps, first the optical energy from a short optical pulse is absorbed by an object, which may be any of the chromophores discussed in the previous section, and produces thermal energy. From the thermal energy generated and due to thermoelastic expansion of the embedded absorber pressure waves are induced. In this section the processes and key parameters required in each of the two steps for efficient optoacoustic signal conversion will be described in detail.

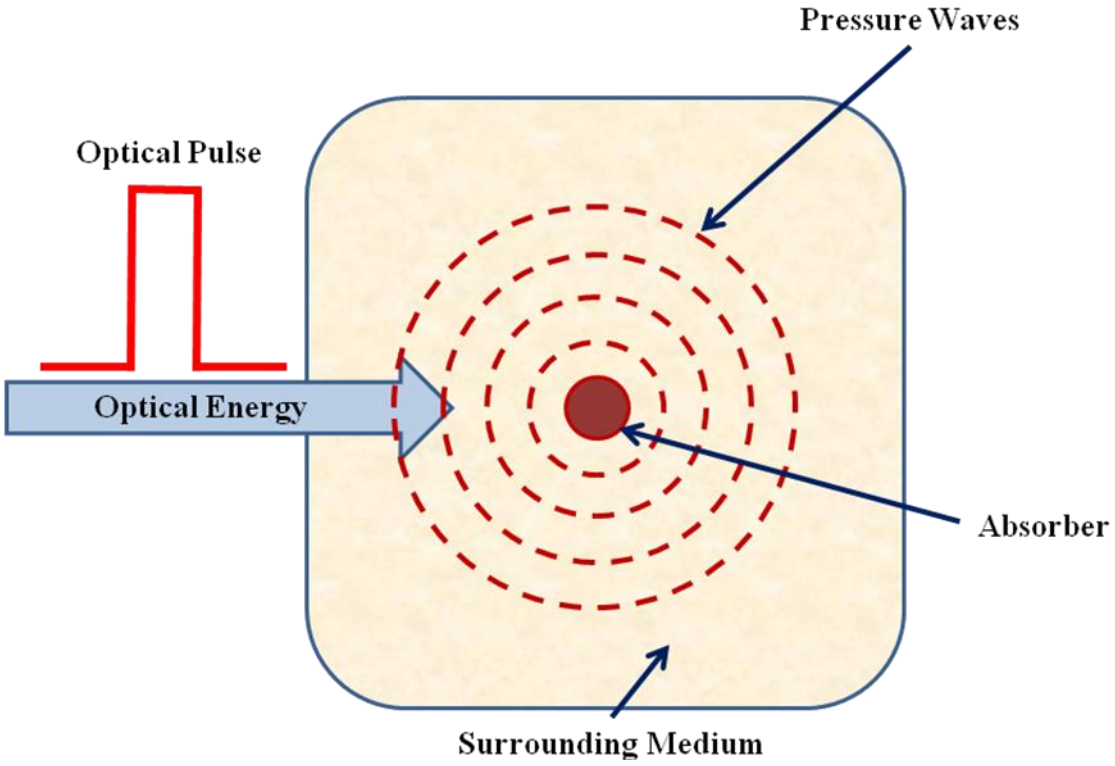

Figure 2.13 General scheme for the production of optoacoustic signals caused by the thermoelastic expansion of an absorber.

2.3.1. Optical to Thermal Energy Conversion

From Beer's law it has been seen that the transmitted light intensity, I_T, by an absorber is related to the initial light intensity, I_0, the absorption coefficient, μ_{abs}, and the optical path distance *d* as (see equation (2.2.6)) [2.2],

$$I_T = I_0 \exp\left(-\mu_{abs} d\right) \tag{2.3.1},$$

thus the absorbed intensity, I_{abs}, can be described by,

$$I_{abs} = I_0 - I_T \tag{2.3.2}.$$

The laser pulse energy absorbed by the medium is $E_{abs} = I_{abs}\tau_p$, where τ_p is the optical pulse duration, determines the amount of thermal energy, E_{th}, induced in the material. The larger the incident laser energy, the more thermal energy is induced into the absorber. From equations (2.3.1) and (2.3.2) it can be seen that the thermal energy is directly related to the absorption of the material, in cases of strong absorption, i.e. $\mu_{abs} r_{spot} \gg 1$, where r_{spot} is the radius of the incident laser spot, acoustic pressure waves will be induced more efficiently [2.25]. The thermal energy generated can be expressed in terms of μ_{abs} and the absorption depth, L_a (see equation (2.2.3)) as,

$$E_{th} \approx E_{abs}\mu_{abs}L_a \tag{2.3.3}.$$

The wavelength dependent thermal energy deposited in the medium per unit volume, $E_{TH}(\lambda)$ (J/cm^3) can be expressed as [2.1-2.2, 2.15]:

$$E_{TH}(\lambda) = \mu_{abs}(\lambda)\frac{E_{abs}}{A} = \mu_{abs}(\lambda)F \tag{2.3.4},$$

where F (J/cm^2) is optical energy density, or fluence, deposited by the laser per unit area A (cm^2). On the surface of the absorber $F_0 = E_0/A$ where the incident optical energy is $E_0(J) = I_0(W)\tau_p(s)$. It can thus be deduced that the optical fluence at a distance *d* (cm) within the media, using Beer's law is [2.26]:

$$F(\lambda, d) = F_0 \exp\left(-\mu_{eff}(\lambda)d\right) \tag{2.3.5}$$

The conversion from the optical energy to thermal energy provokes an increase in the temperature of the medium which can be evaluated using [2.27]:

$$\Delta T(\lambda) = \frac{\mu_{abs}(\lambda) F}{\rho C_V} = \frac{E_{TH}(\lambda)}{\rho C_V} \tag{2.3.6}$$

Where the temperature increase ΔT (ºC) is dependent on the wavelength of the laser source and is given in function of the density of the medium ρ (g/cm^3), the heat capacity at constant volume C_V (J/g ºC) and is directly proportional to the thermal energy deposited by the laser source per unit volume.

To efficiently generate optoacoustic signals a condition referred to as *Thermal Confinement* must be satisfied. The heat generated from the absorbed optical energy is transferred to neighboring molecules. The time scale for heat dissipation of the absorbed energy by thermal conduction is related to the linear volume of the tissue being heated by the optical irradiation. The thermal relaxation time, τ_{th} (sec), of the heated volume can be approximated by [2.28]:

$$\tau_{th} \approx \frac{\rho C_p L^2}{4k} = \frac{L^2}{4\alpha_T} \tag{2.3.7},$$

where L(cm) is the. penetration depth, k $W \cdot K^{-1} \cdot cm^{-1}$ the thermal conductivity, ρ (g/cm^3) the density of the material, and C_p (J/g ºC) the specific heat capacity of the absorber at constant pressure. The thermal diffusivity of the medium is $\alpha_T = k / \rho C_p$. It can be seen from equation (2.3.7) that for high values of α_T the temperature generated in a localized area rapidly adjusts to the temperature of its surroundings. A typical value for the thermal diffusivity in most biological tissues is $\alpha_T \approx 1.4 \cdot 10^{-3}$ (cm^2 s^{-1}) [2.28]. For a material which is dominated by absorption, i.e. $\mu_{abs} \gg \mu_{sca}$ the penetration depth is given by $L = L_a = \mu_{abs}^{-1}$ (see equation (2.2.3)). To fulfill the condition of thermal confinement the optical pulse duration, τ_p, should be short compared to the thermal relaxation time, i.e. $\tau_p < \tau_{th}$, of the heated volume so that there is no heat loss by thermal diffusion during the heating process, see Figure 2.14.

Considering a highly absorbing biological tissue where $\mu_{abs} = 200\,\text{cm}^{-1}$, from equation (2.2.3) $L_a = 50\,\mu\text{m}$ and using equation (2.3.7) the laser pulse width required for efficient thermally confined optoacoustic signal generation must be $\tau_p < \tau_{th} = 4.5\,\text{ms}$, which is easily satisfied.

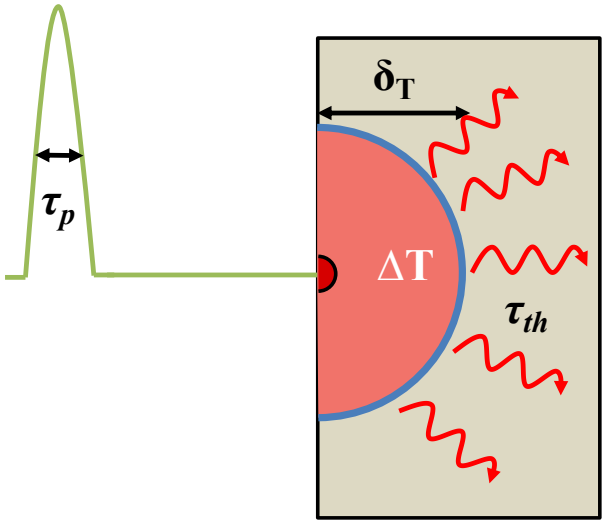

Figure 2.14 Thermal confinement of a short optical pulse incident on an absorbing medium

2.3.2. Thermal to Acoustic Conversion

All materials change in size when subjected to a change in temperature ΔT. The laser – induced thermal energy deposited in the medium leads to an increase in pressure P (Pa) that is determined by the relative change in volume, $\Delta V/V$, the coefficient of thermal expansion β (K^{-1}) and the thermodynamic coefficient of isothermal compressibility of the medium γ (bar^{-1}) and is given by [2.29-2.30]:

$$\Delta P(\lambda) = -\frac{1}{\gamma}\frac{\Delta V}{V} + \frac{1}{\gamma}\beta\Delta T(\lambda) \qquad (2.3.8),$$

where

$$\gamma = \frac{1}{\rho v_{med}^2}\frac{C_p}{C_V} \qquad (2.3.9)$$

here ρ (g/cm^3) is the density, v_{med} (m/sec) is the speed of sound in the medium and C_p (J/g ºC) and C_v (J/g ºC) are the specific heat capacities at constant pressure and volume, respectively. If a short pulse irradiates the tissue and there is no deformation of the

medium, then it can be said that the relative change in volume from equation (2.3.8) $\Delta V/V \approx 0$ thus the change in pressure can be approximated by:

$$\Delta P(\lambda) \approx \frac{1}{\gamma} \beta \Delta T(\lambda) \tag{2.3.10}$$

This approximation is only valid when the condition known as the *Stress Confinement* is satisfied. This requires that the time for deposition of heat in the medium is faster than the time for the material to change in volume in response to the heat, i.e. thermal expansion. To fulfill this condition the optical pulse duration must be shorter than the time taken for the thermoelastic wave to propagate a distance equal to the optical penetration depth (see Figure 2.15), this time is commonly referred to as the stress relaxation time, τ_{stress} (sec). The condition of stress confinement can be expressed in terms of the characteristic linear dimension of the tissue volume being heated L, and the speed of sound in the medium, v_{med}, by [2.27]:

$$\tau_p < \tau_{stress} = \frac{L}{v_{med}} \tag{2.3.11}$$

Taking again $L_p = 50\,\mu\text{m}$ and the speed of sound in biological tissue to be 1.5 mm/μs then the laser pulse width is $\tau_p < \tau_{stress} = 33.3\,\text{ns}$.

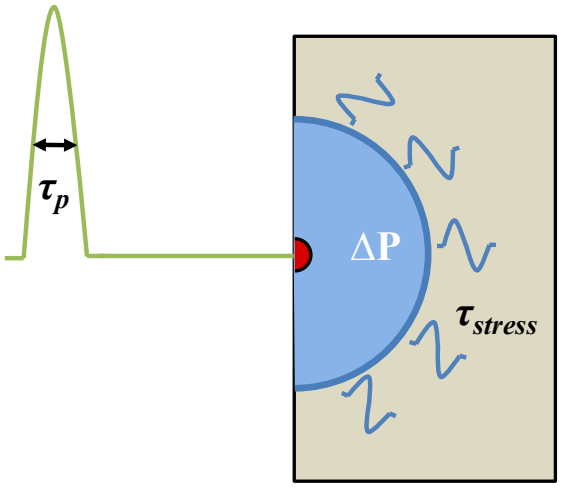

Figure 2.15 Stress confinement of an optical pulse incident on an absorbing medium.

From equation (2.3.10) we can see that the pressure induced is directly proportional to the increase in temperature. It should be highlighted here that the pressure generated

from the optical interaction is dependent on the wavelength of the optical source. Substitution of equation (2.3.6) into equation (2.3.10) gives:

$$\Delta P = \frac{1}{\gamma}\frac{\beta}{\rho C_V} E_{TH} \tag{2.3.12}$$

Using equation (2.3.12) a term for the thermoacoustic efficiency can be defined which is commonly referred to as the *Grüneisen Parameter*. This parameter indicates the ratio of the laser energy that is available for conversion into acoustic energy and is given by [2.1, 2.30]:

$$\Gamma = \frac{1}{\gamma}\frac{\beta}{\rho C_V} = \frac{\beta v_{med}^2}{C_P} \tag{2.3.13}$$

The Grüneisen parameter is a dimensionless and temperature dependent factor. For water and aqueous solutions at room temperature, T = 20 ºC, the Grüneisen parameter equals 0.1 [16, 31]. Muscle contains roughly 75 % water, taking this as an example, the volume expansion coefficient $\beta \approx 3.8\times10^{-4}$ (K^{-1}), the heat capacity is $C_p = 3.7$ (mJ/g mK), and the speed of sound in muscle $v_{med} = 1.5$ mm/µs, then from equation (2.3.13) the Grüneisen parameter is calculated as ~ 0.23 in muscle [2.32].

Substitution of equation (2.3.13) into equation (2.3.12) gives:

$$\Delta P = \Gamma E_{TH}(\lambda) = \Gamma \mu_{abs}(\lambda) F_0 \tag{2.3.14}$$

From equation (2.3.14) it can be seen that the initial pressure of the optoacoustic signal generated is directly proportional to the optical energy absorbed which is dependent on the wavelength. This is an important fact when considering optoacoustic spectroscopy where the spectroscopic profile can be obtained using a range of different wavelengths for the generation of the optoacoustic signals.

In Figure 2.16 the pressure generated at a distance *d* from the surface of a material, i.e. biological tissue, with both absorption and scattering is presented. This process may be described by [2.16]:

$$p(d,\lambda) = \Gamma \mu_{abs}(\lambda) F_0 \exp\left(-\mu_{eff}(\lambda) d\right) \tag{2.3.15}$$

Where p is the wavelength dependent pressure at a distance d from the edge of the turbid media.

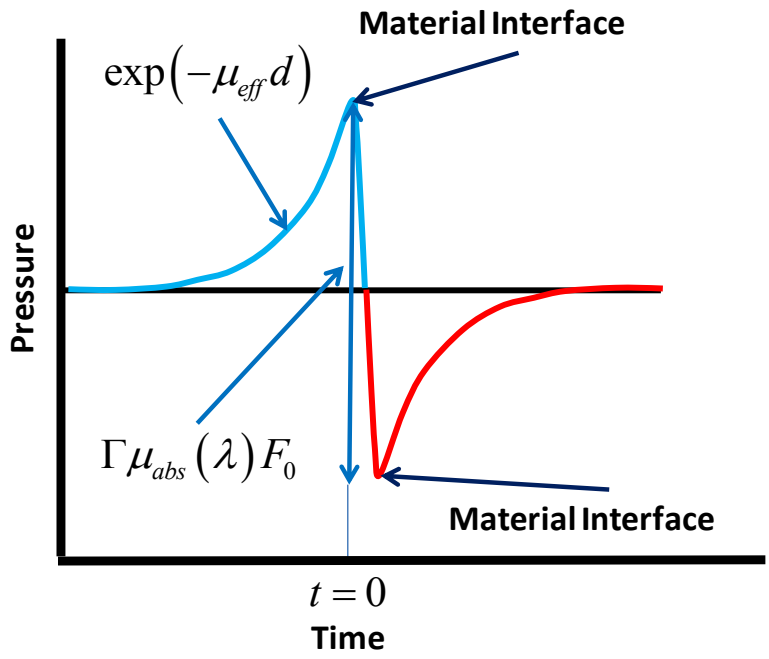

Figure 2.16 Pressure transient generated at the interface of a turbid media.

2.3.3. Temporal Profile of an Optoacoustic Signal

It has been demonstrated that the optoacoustic acoustic transients generated from the optical absorption and thermoelastic expansion contain information on the optical properties of the medium being irradiated. The profile of the optoacoustic signal transmitted by an absorber, such as a cancerous growth, which has a complex geometrical structure, can be represented by the convolution of acoustic waves emitted by a number of small spherical sources.

Considering a sphere of radius r where the absorption coefficient $\mu_{abs} \gg \mu_{sca}$ and that the following conditions are satisfied:

1. Uniform absorption of optical energy, i.e. $\mu_{abs} \ll 1/r$,
2. Thermal confinement, $\tau_p < \tau_{th}$,
3. Stress confinement, $\tau_p < \tau_{stress}$,

4. The acoustic properties of the spherical absorber are identical to the surrounding medium,

then the acoustic pulse generated due to the thermoelastic expansion of the absorber will be launched in all directions (see Figure 2.16) where the pressure generated can be expressed as [2.30]:

$$p'\left(\tau = t - \frac{R}{v_{med}}\right) = \frac{1}{2R}\Gamma\frac{\mu_{abs}F_0}{V_{sph}}\begin{Bmatrix} -v_{med}\tau, |v_{med}\tau| \le r \\ 0, |v_{med}\tau| \ge r \end{Bmatrix} \qquad (2.3.16)$$

Here the volume of the sphere is $V_{sph} = 4\pi r^3/3$, R is the distance from the point of observation to the centre of the spherical absorber, v_{med} is the speed of sound in the medium and F_0 is the laser fluence incident on the sphere.

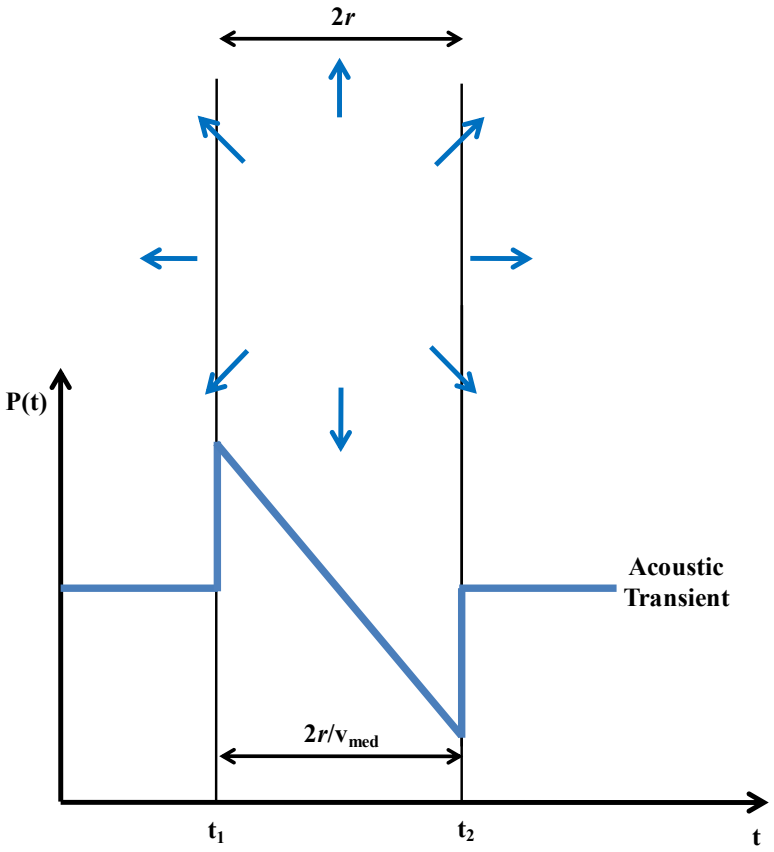

Figure 2.17 Temporal waveform of the optoacoustic signal generated by a sphere of radius *r*, where the speed of sound in the medium is v_{med}.

The optoacoustic wave produced presents the typical N-shape profile with triangle phase compression followed by the antisimmetric tension phase (see Figure 2.17)

[2.30]. The duration of the optoacoustic signal is defined by the speed of sound propagation along the diameter of the sphere, given as:

$$2r = \frac{(t_2 - t_1)v_{med}}{2} \tag{2.3.17}$$

Information on the frequency spectrum of the acoustic signal transients generated from the optical interaction with the sphere is provided from a Fourier Transform of the temporal signal, given as [2.33]:

$$P(\omega) = \int_{-\infty}^{+\infty} p'(\tau)\exp(-i\omega\tau)d\tau \tag{2.3.18}$$

Where the spectrum has the following form [2.33]:

$$p(\omega) \propto \frac{(\omega r/v_{med})\cos(\omega r/v_{med}) - \sin(\omega r/v_{med})}{(\omega r/v_{med})^2} \tag{2.3.19}$$

Where ω is the frequency of the ultrasonic signals, the modulus of this spectrum is presented in Figure 2.18.

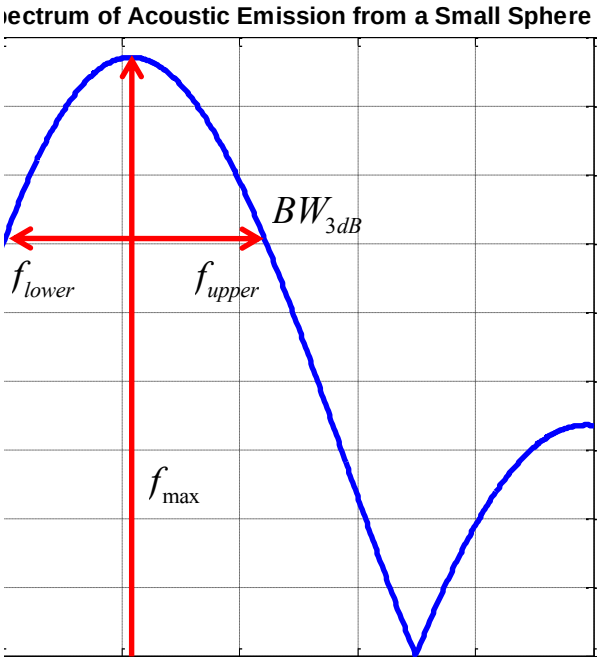

Figure 2.18 Fourier spectrum of acoustic emission from a small sphere as a function of the ultrasonic frequency.

From this Fourier spectrum two valuable pieces of information can be extracted. The first, is the frequency when the spectrum is at a maximum, see equation (2.3.20) and secondly, the bandwidth of the optoacoustic emission, where the calculation from Figure 2.18 is shown in equation (2.3.21).

$$f_{\max} = 0.33\frac{v_{med}}{r} \tag{2.3.20}$$

$$BW_{3dB} = f_{upper} - f_{lower} = 0.51\frac{v_{med}}{r} - 0.16\frac{v_{med}}{r} = 0.35\frac{v_{med}}{r} \tag{2.3.21}$$

The above expression (equation (2.3.21)) describes the acoustic signal bandwidth for an absorbing sphere. However this bandwidth is only suitable for the low frequency part of the acoustic signal that decreases linearly (see *N-shape* Figure 2.17). To detect the rise and fall of the acoustic signal at the boundaries a higher bandwidth is required. However, by increasing the bandwidth the thermal noise in the detection process is also increased, thus a compromise must be made. This is usually done by considering that the rise time of the acoustic signal is 0.3 times the total pulse time, in this case $0.3 \cdot 2r/v_{med}$, which in terms of frequency is equivalent to

$$f_{\max} = 1.5\frac{v_{med}}{r} \tag{2.3.22}$$

In soft tissue spherical particles of many different dimensions may exist, thus it is necessary that the bandwidth of the detector is capable of detecting the temporal profile of each sphere. Consider two spherical tumours embedded in soft tissue with radius 1 mm and 5 mm, where the acoustic velocity in the tumour is 1.5 mm/μs, then the bandwidths of the acoustic signals from each sphere, using equation (2.3.22), are 2.25 MHz for the 1 mm radius sphere and 450 KHz for the 5 mm diameter sphere.

2.3.4. Laser Source for Efficient Optoacoustic Signal Generation.

The optical source is regarded as the key component of any optoacoustic signal generation system. The most efficient optical sources which produce thermoelastic signal generation are based on short pulsed laser sources. Such sources have many advantages over modulated continuous sources. The major advantage is based on the

high energy stored in each pulse, producing strong acoustic signals thus improving the signal to noise ratio.

Pulsed lasers deposit large amounts of energy in a short space of time. It has already been demonstrated that the pulse width of the laser source should be small enough so that the thermal energy generated is not given enough time to disperse into the bulk material, i.e. the thermal confinement condition $\tau_p < \tau_{th}$. Also the optical pulse should be short enough so that the energy deposited does not dissipate acoustically, i.e. stress confinement condition, $\tau_p < \tau_{stress}$. For optoacoustic signal generation in biomedical applications, within the therapeutic window, the main lasers used are:

1. Q-Switched Nd:YAG,
2. Pulsed semiconductor lasers,
3. Q – Switched Nd:YAG Laser Pumped Optical Parametric Oscillator.

Currently there is a lot of interest in diode lasers as sources for optoacoustic signal generation in biomedical applications [2.14, 2.26, 2.34], this is due to their numerous advantages over traditional pulsed laser systems, such as; small size, low cost, wide range of visible and NIR wavelengths and controllable pulse width and repetition rates. However, the main drawbacks to such optical sources arise due to the low peak power available when compared to solid state lasers. The authors of [2.34] have combined the optical power from two high power semiconductor laser stacks (TPGAU3S09, Perkin Elmer) to produce optoacoustic signals in a biomedical phantom. The operating wavelength of these lasers sources was 905 nm producing a maximum peak power between 210 W and 224 W. It has been demonstrated that by using two similar laser sources under the same operating conditions that the optoacoustic signal produced doubles in amplitude. More details regarding this experimental procedure can be found in Appendix B.

The Nd:YAG laser (more precisely Nd^{3+}:YAG, which is an acronym for neodymium – doped yttrium aluminium garnet) is the preferred choice of laser source for the generation of acoustic transients as it efficiently satisfies both the thermal and stress confinement conditions discussed previously [2.35-2.36]. It is commonly used in optoacoustic imaging applications. In [2.37] the authors have designed a novel

optoacoustic imaging system and in [2.38] the authors have studied the brain of in *in-vivo* animal models. As part of the experimental work presented in this thesis, this type of laser source has been used for the optoacoustic measurement scheme designed to quantify the optical properties of pure absorbers located within a highly scattering medium (see Chapter 4).

Another commonly used short pulsed optical source which satisfies the conditions for efficient optoacoustic signal generation by thermal expansion is the high energy multi-wavelength Nd:YAG pumped Optical Parametric Oscillator (OPO). This device operates similarly to that of a laser, containing also a laser cavity, but is based on the gain from parametric amplification in a nonlinear crystal rather than from stimulated emission and produces a wide range of wavelength controllable optical output pulses within the therapeutic window. Advantage has been taken of this fact to determine the spectroscopic properties of both spherical and rod shaped gold nanoparticle solutions.

2.4. Conclusions

In this chapter the key concepts related to tissue optics and optoacoustic signal generation have been presented. This review has begun with a description of the propagation of light. It has been shown here that the attenuation of light is principally governed by absorption and scattering. The transmitted optical intensity is seen to decrease exponentially, according to Beer's law, where the decay is directly related to the wavelength dependent optical absorption and scattering coefficients of the medium, μ_{abs} and μ_{sca}, respectively.

In biological media the scattering of electromagnetic energy from a laser source is directionally dependent, resulting in a reduced scattering coefficient, $\mu_{sca}^{'}$, that is characterized by the anisotropy parameter, *g*. A review of radiative transport theory in soft tissue using the diffusion approximation has provided a clear understanding of diffuse light propagation caused by multiple scattering. From a spectroscopic review of the main biological chromophores used for diagnostic purposes, the optimum wavelength range of the optical source for biomedical applications has been identified.

By examining the behavior of optical energy in attenuating media the chief parameters associated with efficient optical to acoustical conversion process have been obtained. The thermoelastic expansion of a medium, caused by the thermal and stress confinement of absorbed short pulsed optical energy, has allowed the principle characteristics of the acoustic pressure transients generated to be investigated. From this analysis it has been seen that the initial pressure of the acoustic wave is directly related to the wavelength dependent absorption coefficient. Advantage has been taken of this fact to design and implement optoacoustic measurement schemes to quantify and spectrally resolve the optical properties of a pure absorber surrounded by a highly scattering medium.

Chapter 3.

Gold Nanoparticles as Optical Contrast Agents for Optoacoustics, Numerical Study of their Optical Properties

3.1. Introduction

Initially gold nanoparticles (GNP's) were commonly referred to as *Colloidal Gold* and *Nanogold* where their basic definition is the suspension of sub-micron particles in a fluid. Colloidal gold has a long and extensive history [3.1], and was known to intrigue the alchemists [3.2]. One of the first references to modern scientific evaluations did not appear until the 5th of February 1857 [3.3] when Faraday M. discussed and presented results from experiments he performed on their optical and electrical properties. Today, nanotechnology is enabling gold to help address critical global problems such as cancer treatment.

The increasing demand for new techniques to enhance spectroscopic characterization and optical contrast *in-vivo* of unhealthy tissue is at the forefront of new innovations in nanomedicine and has motivated the work presented in this thesis. The most important feature of colloidal nanostructure solutions is based on their optical properties which during synthesis can be tuned to specific wavelengths within the therapeutic window. In this chapter a full description of the origin of the spectroscopic properties and how they are related to the geometric structure of the particles will be presented. This analysis will cover two different gold nanostructures; nanospheres and nanorods.

To gain more insight into the behavior of gold nanostructures, a theoretical analysis based on Mie theory for homogeneous nanospheres [3.4-3.5] and an extension of Mie's Theory presented by Gans for randomly orientated elongated cylinders in the dipole approximation will be presented [3.6]. This numerical analysis will define the optical parameters in function of the most important nanoparticle structural properties. One of the main objectives of this theoretical review is to identify the key parameters required for the design of the optoacoustic characterization schemes presented in Chapter 4. This information includes, the spectral range of interest, the position of the absorption peaks, and the relation between the scattering and absorption of the particles.

3.2. .Surface Plasmon Resonance (SPR)

The chief parameter associated with nanoparticle based colloidal solutions is their wavelength dependant optical properties. A clear understanding of the influence their geometric shape and size has on their optical attenuation is essential for their controlled synthesis and tunability over the wavelength range of interest. To experimentally characterize the optical properties of such nanoparticle solutions a spectroscopic analysis is required. The experimental work performed in this thesis has explored a spectroscopic analysis using the optoacoustic technique.

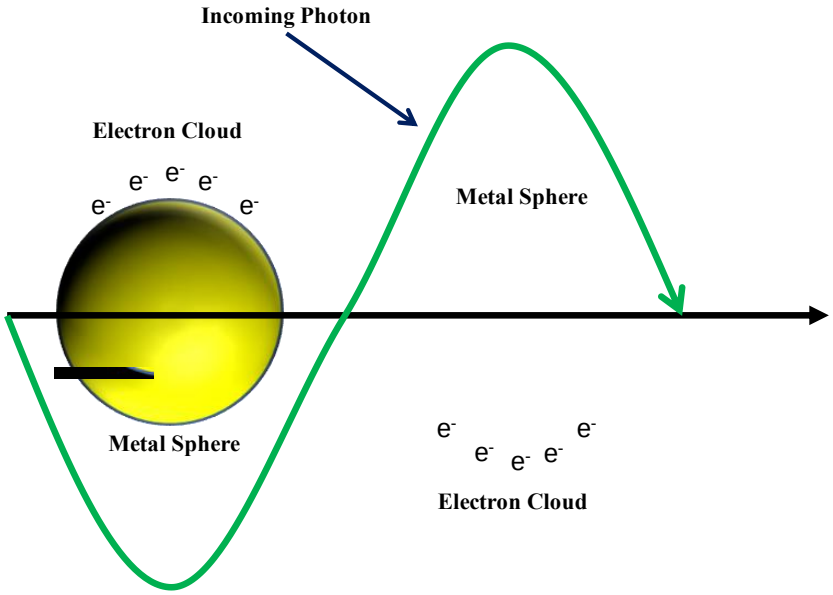

Figure 3.1 Surface plasmon resonance (SPR) induced by the interaction of photons with the free electrons of a metal sphere.

When photons interact with nanoscale semiconductor and metal materials, physical phenomena occur which are not present in their corresponding bulk materials. The key to understanding the optical properties of noble element nanoparticles is based on their *Surface Plasmon Resonance* (SPR). This occurs when the electromagnetic field interacts with the conduction band electrons and induces a coherent oscillation of the free electrons in the metal, see Figure 3.1 . The SPR is the extinction band that results when the collective oscillation of the surface electrons are resonant with the incident photon frequency. Thus, a strong extinction band appears in a specific part of the electromagnetic spectrum which is dependent on the size and geometrical nature of the

nanoparticle. At this resonant frequency two processes occur, first, several of the photons are released with the same frequency in all directions, known as scattering, and secondly, other photons are converted into phonons or vibrations of the lattice via absorption.

In Figure 3.2 the normalized spectral response modeled for a spherical gold nanoparticle over the wavelength range from 300 nm to 700 nm is presented. The extinction band resulting from the resonant properties of the surface electrons peaks at 520 nm.

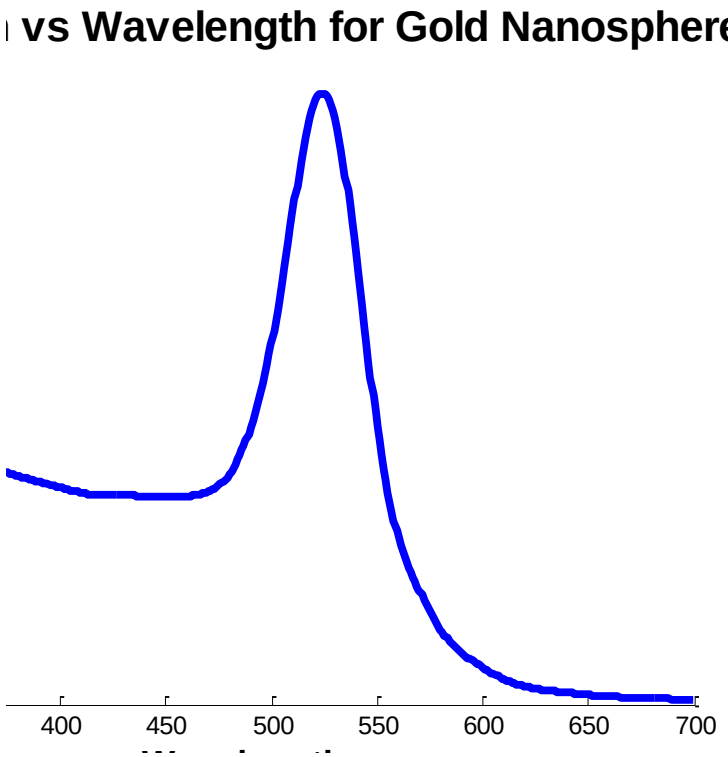

Figure 3.2 Extinction coefficient, $\mu_{ext} = \mu_{abs} + \mu_{sca}$, of a spherical nanoparticle solution demonstrating a peak attenuation associated with the surface plasmon resonance at 520 nm.

Gold nanorods (GNR's) are attractive new nanomaterials which have found a wide range of applications in the biomedical field. The nanorod structure is especially appealing due to its unique optical properties and wavelength tunability within the NIR part of the optical therapeutic window.

The surface plasmon resonance properties of GNRs split into two distinct bands which correspond to the oscillation of the free electrons along and perpendicular to the long axis of the rod. The *transverse surface plasmon* peak, TSP, in gold nanorods typically

demonstrates a resonance peak close to 520 nm. The resonance of the *longitudinal surface plasmon*, LSP, is commonly found between the visible and NIR part of the electromagnetic spectrum. The position of the LSP is dependent on the ratio between the length and width of the nanorod, commonly referred to as the *Aspect Ratio* (R), which is given by $R = L/W$ (see Figure 3.3).

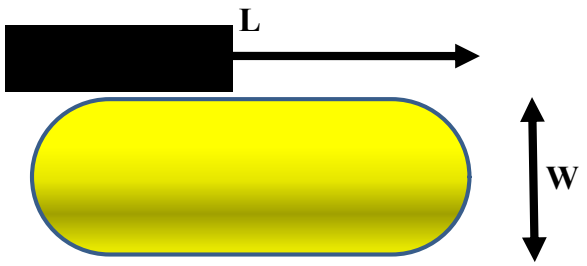

Figure 3.3 Gold nanorod geometrical structure, the Aspect Ratio (AR) of a nanorod is given by

$$AR = L/W$$

In Figure 3.4 the typical spectroscopic response of a GNR solution showing both the TSP and LSP over the wavelength range from 400 nm to 900 nm is presented.

Figure 3.4 Spectral response of nanorod nanostructure showing peaks associated with plasmon oscillations in the longitudinal and transverse directions.

3.3. Optical Properties of Gold Nanostructures.

By controlling the shape and dimensions of nanoparticles during their synthesis the optical scattering and absorption can be tuned to specific wavelengths. This is particularly beneficial when they are used as optical contrast agents in biomedical applications. To understand this process, a numerical analysis based on the light/nanoparticle interaction has been developed to identify both the absorption and scattering properties in function of the nanoparticles dimensions. This procedure provides key information required during their synthesis to control their wavelength tunability and has also provided experimental parameters required for the characterization schemes presented later in this thesis.

Both *Rayleigh theory* and *Mie theory*, which are both based on Maxwell's equations, can be used to model the scattering of a plane monochromatic optical wave by a single spherical particle. The main assumption of both theories is that the particle and its surrounding medium are both homogenous and can be described by their bulk optical refractive index (i.e. by a single refractive index at a given wavelength). In this section Mie theory has been used to explore the dependence the diameter of spherical gold nanoparticles (SGNP's) has on both the absorption and scattering of light separately. This approach has been used by other authors to determine similar optical properties [3.4, 3.7-3.9].

There are two accepted methods to determine the relation between GNR structures and the LSP and TSP peaks. The first, a discrete dipole approximation (DDA), developed by Purcell and Pennypacker [3.10] is a flexible and general technique for calculating the optical properties of particles of arbitrary shapes [3.11-3.12] and has been used to investigate the optical properties of GNRs for biomedical applications [3.7]. The second technique used to model the optical properties of GNRs is Gans's extension to Mie theory, this is based on a dipole approximation [3.9, 3.13]. The latter technique has been used in this thesis to define the dependence of the GNR structural properties on the attenuation of light. In this context, within this section the concepts of both Rayleigh theory and Mie theory will be presented. However, before this a review of the most critical parameter for the numerical analysis will be presented, this is the refractive index of the nanomaterial.

3.3.1. Nanoparticle Refractive Index

The predictive efficiency of the optical behavior of nanoparticles using both Rayleigh and Mie theory is highly dependent on the wavelength dependent refractive index properties of the nanoparticles. To determine the absorption and scattering properties of the particles the complex refractive index must be taken into consideration, where $n_{particle} = n_{real} + in_{imag}$. The real part indicates the speed of the phase and the imaginary part indicates the amount of attenuation due to absorption. Note that both of these terms are wavelength dependent. For particles which scatter and do not absorb light the refractive index is always real, i.e. $n_{imag} = 0$ and vice versa for absorption. Another important term used in both Rayleigh and Mie theory is the relative refractive index, *m*, given as the ratio between the refractive index of the particle, $n_{particle}$, and the surrounding medium, n_{medium}:

$$m = \frac{n_{particle}}{n_{medium}} \tag{3.3.1}$$

The values for both the real and imaginary parts of the refractive index used in the numerical analysis presented in this thesis to study the behavior of both the spherical and rod shaped nanostructures have been taken from experimental work performed by Johnson and Christy [3.14] and Weaver and Frederikse [3.15]. This experimental work for both the real and imaginary refractive indices of gold is presented in Figure 3.5. It can be observed from this graph that the refractive index values from both authors are very similar up to 1000 nm. However, it will be seen later in this chapter that only slight differences in the refractive index change considerably the position of the peak SPR.

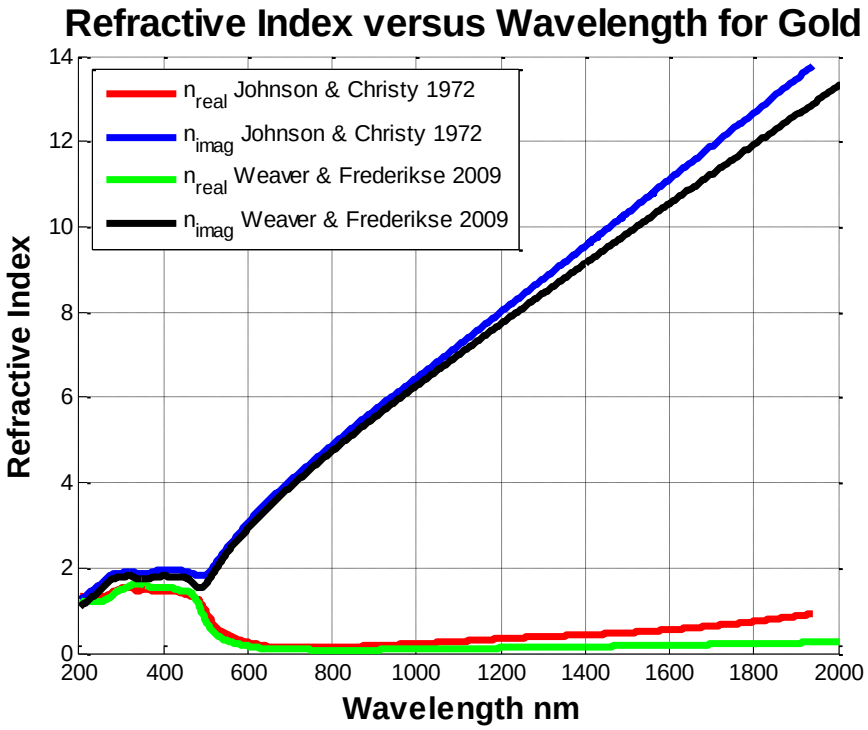

Figure 3.5 Spectral plot of the real (n_{real}) and imaginary (n_{imag}) refractive indices of gold taken from experimental work performed in [3.14-3.15]

3.3.2. Rayleigh Limit

The elastic scattering of light by tissue structures and particles which have dimensions much smaller than that of the incident photon wavelength is commonly described using *Rayleigh Theory*. The size of a scatterer is parameterized by the ratio of the characteristic dimension *r* and the wavelength λ as (see Figure 3.6):

$$x = \frac{2\pi r}{\lambda} \tag{3.3.2}$$

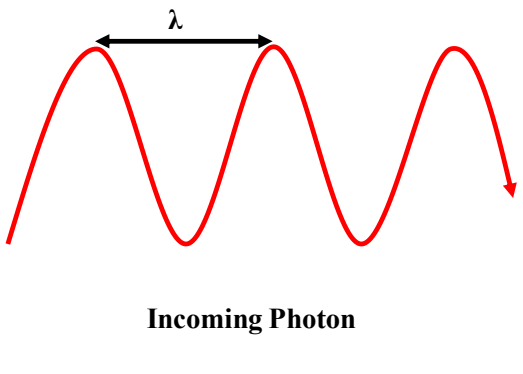

Figure 3.6 illustration of the ratio of the characteristic dimension of a spherical particle to the incoming photon wavelength.

Where Rayleigh theory is used for scattering events for the small size parameter regime $x << 1$. Rayleigh scattering is highly dependent on the size of the particle and the wavelength of the incident light. More specifically, the Rayleigh scattering cross section, $\sigma_{sca-Ray}$, is proportional to the sixth power of the particle size and inversely proportional to the fourth power of the wavelength. The Rayleigh absorption cross section, $\sigma_{abs-Ray}$, is dependent on the third power of the particle radius. Expressions for both of these terms can be written as [3.4, 3.16]:

$$\sigma_{sca-Ray} = \frac{8\pi r^6 k^4}{3}\left|\frac{m^2-1}{m^2+2}\right|^2 \tag{3.3.3}$$

$$\sigma_{abs-Ray} = 4\pi r^3 k \,\mathrm{Im}\left(\frac{m^2-1}{m^2+2}\right) \tag{3.3.4}$$

Here both the scattering and absorption cross sections are given in terms of the radius of the particle, *r*, the relative refractive index *m* (see equation (3.3.1)) and *k* is the wave number, given by:

$$k = \frac{2\pi n_{medium}}{\lambda_0} \tag{3.3.5}$$

Where n_{medium} is the refractive index of the medium surrounding the particle and λ_0 is the wavelength of the incoming light in a vacuum. In expression (3.3.4) *Im* indicates the imaginary part of the complex expression for the relative refractive index, if *m* is real ($n_{imag} = 0$), there is no light absorption and $\mu_{abs-Ray} = 0$.

The spectroscopic response from 300 nm to 700 nm of spherical particles using Rayleigh theory is presented in Figure 3.7 (a) for a 20 nm particle diameter solution and Figure 3.7 (b) for a 15 nm particle diameter solution. These dimensions have been chosen as they have been used in experimental characterization presented later in this thesis.

There are two main disadvantages to using Rayleigh theory, the first is that the model tends to provide poor results when the diameter of the particles increases beyond 10 % of the incident light wavelength. Secondly, Rayleigh theory assumes isotropic scattering. Thus for larger particles which demonstrate forward scattering Mie theory is more appropriate.

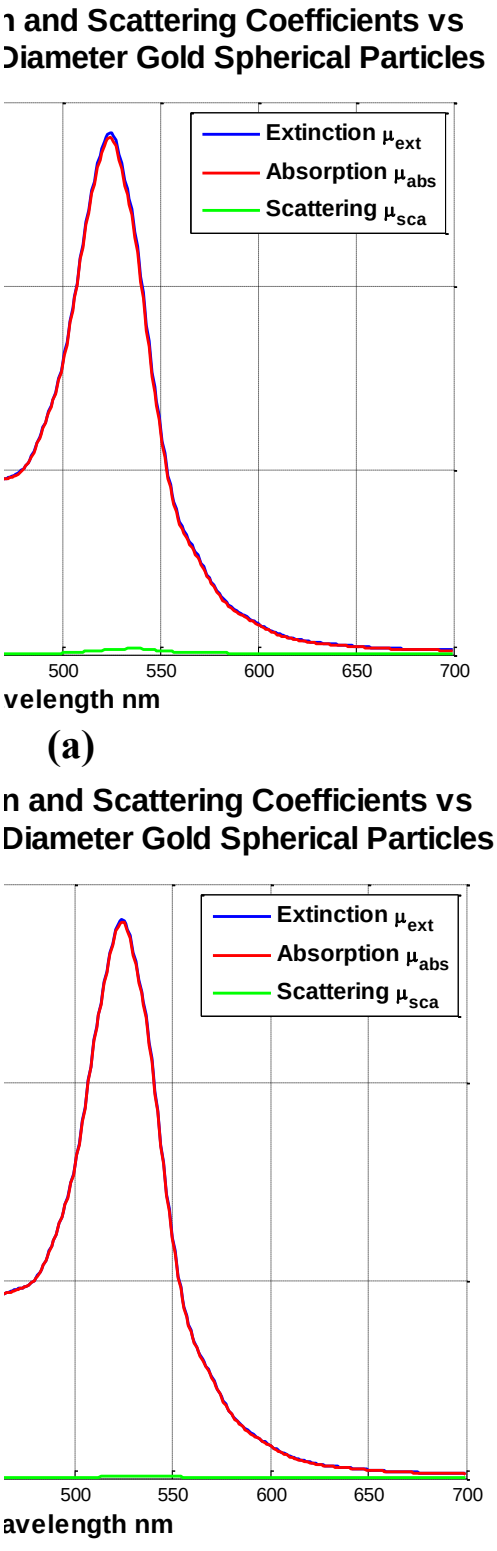

Figure 3.7 The optical absorption coefficient, μ_{abs}, optical scattering coefficient, μ_{sca}, and extinction coefficient, $\mu_{ext} = \mu_{abs} + \mu_{sca}$, for (a) 20 nm spherical gold nanoparticle and (b) 15 nm gold nanoparticle using Rayleigh theory

3.3.3. Mie Regieme

Mie theory can be used to determine the optical properties of particles of any size where the expressions for the absorption and scattering coefficients of a sphere can be described in terms of the scattering and total extinction cross sections using the following equations [3.4, 3.8]:

$$\sigma_{sca} = \frac{2\pi}{k^2}\sum_{n=1}^{\infty}(2n+1)\left(|a_n|^2 + |b_n|^2\right) \tag{3.3.6}$$

$$\sigma_{ext} = \frac{2\pi}{k^2}\sum_{n=1}^{\infty}(2n+1)\,\mathrm{Re}\left(a_n + b_n\right) \tag{3.3.7}$$

Here k is the wave number (see equation (3.3.5)), the total extinction cross section, σ_{ext}, describes the sum of both the scattering and absorption cross sections as:

$$\sigma_{ext} = \sigma_{sca} + \sigma_{abs} \tag{3.3.8}$$

The Mie extinction coefficient is derived in terms of the number density of particles, N, (cm^{-3}) and is given by:

$$\mu_{ext} = \sigma_{ext} N \tag{3.3.9}$$

The key parameters associated with Mie theory calculations are the Mie coefficients a_n and b_n required to compute the amplitude of the scattered fields. These are given by [3.4-3.5]:

$$a_n = \frac{m^2 j_n(mx)\left[xj_n(x)\right]' - \mu_1 j_n(x)\left[mxj_n(mx)\right]'}{m^2 j_n(mx)\left[xh_n^{(1)}(x)\right]' - \mu_1 h_n^{(1)}(x)\left[mxj_n(mx)\right]'} \tag{3.3.10}$$

$$b_n = \frac{\mu_1 j_n(x)\left[xj_n(x)\right]' - j_n(x)\left[mxj_n(mx)\right]'}{\mu_1 j_n(mx)\left[xh_n^{(1)}(x)\right]' - h_n^{(1)}(x)\left[mxj_n(mx)\right]'} \tag{3.3.11}$$

The functions $j_n(z)$ and $h_n^{(1)}(z) = j_n(z) + iy_n(z)$ are spherical Bessel functions of the order n *(n = 1, 2, 3, ...)* and of the given argument $z = x$ or mx, respectively. Where m is the relative refractive index of the sphere (see equation (3.3.1)). More details regarding the Mie coefficients are provided in Appendix C Section C.2.

3.4. Numerical Analysis of the Optical Properties of Gold Nanospheres using Mie Theory

Due to the ratio between the size of the particles and the wavelength of the incoming photons and also the anisotropic nature of the scattered light, Mie Theory (equations (3.3.6) and (3.3.7)) has been used to investigate the dependence of the particle radius on the spectroscopic profile of SGNPs. To perform this numerical spectral analysis both the wavelength dependent real and imaginary parts of the gold particles refractive index have been taken from the experimental data presented by Weaver and Frederikse (see Figure 3.5).

3.4.1. Mie extinction coefficient

The Mie extinction coefficient (i.e. $\mu_{ext} = \mu_{abs} + \mu_{sca}$) for a series of SGNPs ranging in diameter from 20 nm to 300 nm have been analyzed over the wavelength range from 300 nm to 700 nm, where the results are presented in Figure 3.8. From this analysis it may be observed that as the diameter of the spherical nanoparticle increases the SPR peak is observed to shift to longer wavelengths. The optical properties obtained from this analysis are in good agreement with similar work from other authors using the same nanostructure parameters and Mie theory [3.4]

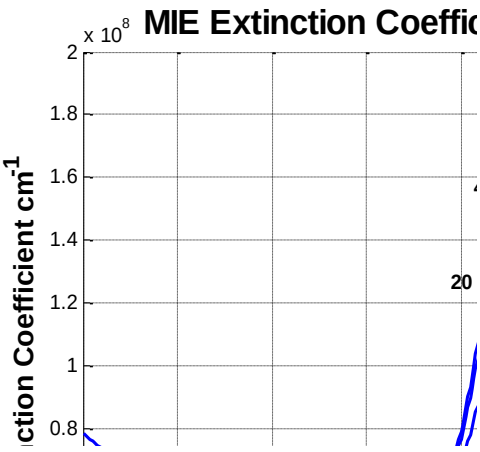

(a)

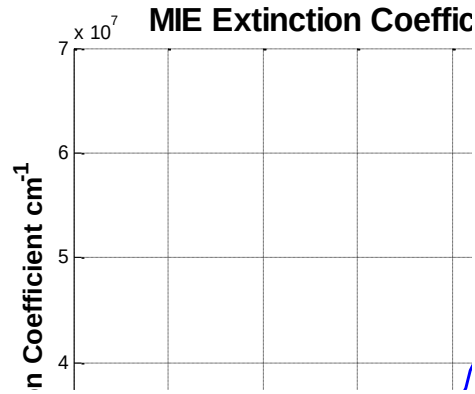

(b)

Figure 3.8 Mie extinction coefficient, μ_{ext}, from Mie theory (see equations (3.3.7) and (3.3.9)) for SGNPs ranging in diameter from (a) 20 nm to 140 nm and (b) 140 nm to 300 nm.

3.4.2. Scattering Coefficient

To investigate the dependence of the particle size on the scattering coefficient the scattering cross section has been calculated for the wavelength range from 300 to 700 nm (see equation (3.3.6)). The refractive index of the gold particle has again been taken from the experimental data obtained by Weaver and Frederikse (see Figure 3.5). The results obtained for the scattering coefficient ($\mu_{sca} = N\sigma_{sca}$) over the wavelength range from 300 nm to 700 nm are presented in the following Figure 3.9 (a) and (b).

From the results obtained and presented in Figure 3.9 (a) it may be observed that the scattering coefficient for smaller spherical particle diameters (20 nm) is small in comparison to particles with larger diameters (100 nm). It is also interesting to observe that the scattering peak shifts to longer wavelengths for larger particles and are seen to decrease in magnitude for particles greater than 100 nm. The evolution of the scattering properties of the spherical gold nanoparticles for diameters ranging from 160 nm to 300 nm is plotted in Figure 3.9 (b) where again it may be observed that the tendency of the scattering peak to shift to longer wavelengths and decrease in magnitude is also evident.

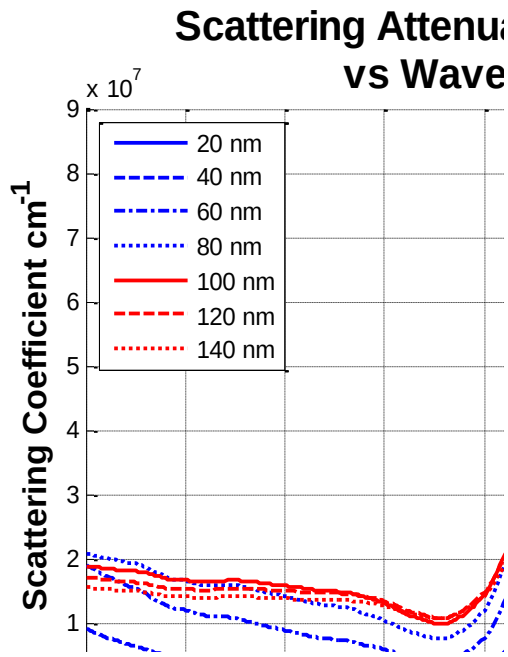

(a)

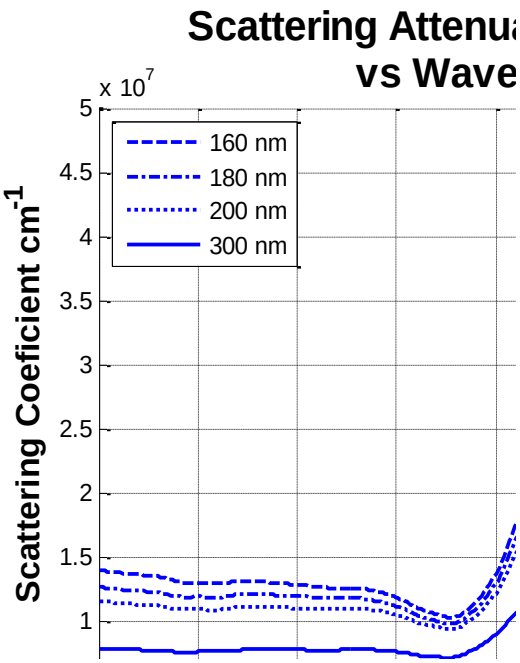

(b)

Figure 3.9 Scattering coefficient, μ_{sca}, from Mie theory (see equations (3.3.6) and (2.2.8)) for SGNPs ranging in diameter from (a) 20 nm to 140 nm and (b) 160 nm to 300 nm.

3.4.3. Absorption Coefficient

The most critical parameter for optoacoustic signal generation is the optical absorption. Thus, to complete this analysis on the homogenous gold spheres the absorption coefficient, μ_{abs}, has been solved over the same wavelength range, i.e. from 300 nm to 700 nm. The absorption coefficient is obtained from the absorption cross section, σ_{abs}, where $\mu_{abs} = N\sigma_{abs}$ (see Chapter 2, equation 2.2.2) and from equation (3.3.8), where:

$$\sigma_{abs} = \sigma_{ext} - \sigma_{sca} \tag{3.4.1}$$

The results for the absorption coefficient versus wavelength are presented in the following Figure 3.10 (a) and (b).

The results show that for the smaller particle diameters (20 nm to 60 nm) absorption is the dominant process, for the SGNP diameter of 80 nm the scattering and absorption components are similar in magnitude. For increasing spherical particle diameters the scattering component is observed to be dominant. To complete the analysis and for comparative purposes, the absorption coefficient was also analyzed for SGNP diameters ranging from 160 to 300 nm, the results are presented in Figure 3.10 (b). Here, and as expected, it may be observed when comparing the response to that presented in Figure 3.9 that the scattering of the particle is dominant.

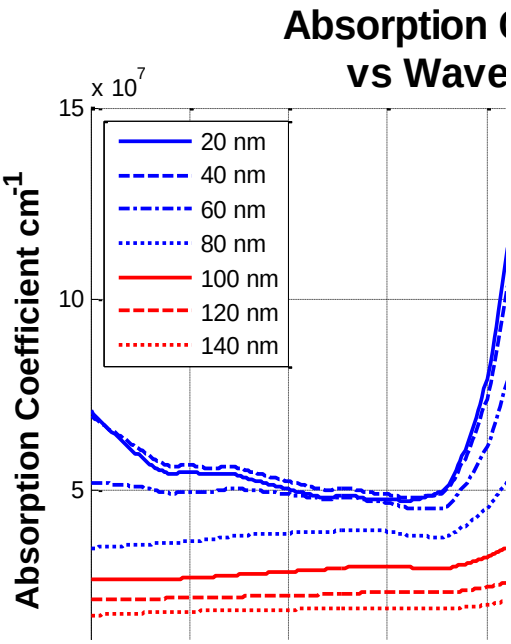

(a)

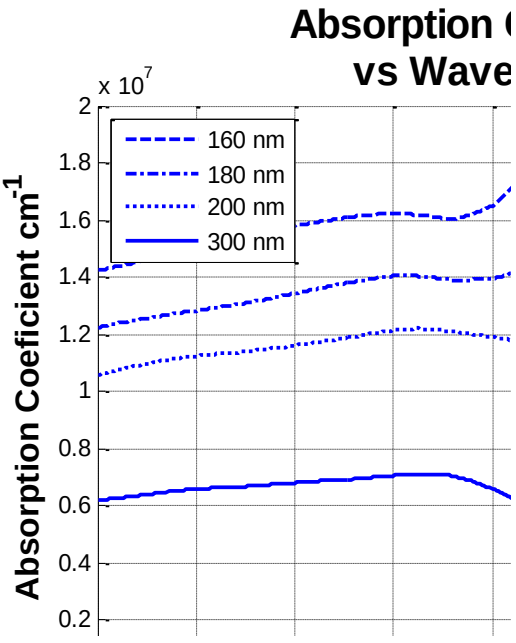

(b)

Figure 3.10 Absorption coefficient, μ_{abs}, from Mie theory (see equations (3.3.6), (3.3.7) and) for SGNPs ranging in diameter from (a) 20 nm to 140 nm and (b) 160 nm to 300 nm.

3.4.4. SGNP Numerical Analysis Discussion

From this theoretical review based on Mie theory, the spectroscopic optical properties of SGNPs have been defined. It may be concluded that for efficient absorption of the optical energy the diameter of the spherical gold particles should ideally be 20 nm or less and that scattering is dominant for particles beyond 80 nm. This analysis has provided the design parameters required for the synthesis of spherical structures that are highly absorbing producing a negligible amount of scattering. Such particles are ideal as contrast agents for enhanced absorption of optical energy producing efficient optoacoustic signal generation.

Other valuable information gained from this theoretical analysis are the experimental parameters required for the design of the laser optoacoustic quantification and characterization schemes, presented in the following Chapter 4 of this thesis. The theoretical analysis has provided the wavelength range of interest for spectroscopic characterization of gold nanospheres, i.e. from 400 nm to 650 nm. For the optical parameter quantification it has been indicated the optimum source wavelength for maximum signal generation should be close to 520 nm.

For the experimental work presented in this thesis, and based on results from Mie theory, the controlled synthesis of two different spherical gold nanoparticles solutions with particle diameters of 20 ± 2 nm and 15 ± 2 nm using the Turkevich method have been performed [3.17-3.18]. More details regarding the synthesis of these particles can be found in Appendix D. Mie theory has again been used to determine the behavior of these particles over the wavelength range from 300 nm to 700 nm where the results are presented in Figure 3.11 (a) for the 20 nm particles and (b) for the 15 nm particles. In both cases it may be seen that the attenuation is dominated by absorption. The ratio of scattered light to absorbed light is calculated in both cases to be 0.01 and 0.008 for the 20 nm and 15 nm particles, respectively. The wavelength peak in both cases is located close to 520 nm. These theoretical findings are in agreement with work performed by other authors in the field of optical parameter characterization of gold nanoparticles [3.7]. Comparing the results from Mie theory in Figure 3.10 to those obtained using Rayleigh theory in Figure 3.7 it can be seen that both theories are in agreement for both the position of the absorption peak and the ratio of scattered to absorbed light at this peak.

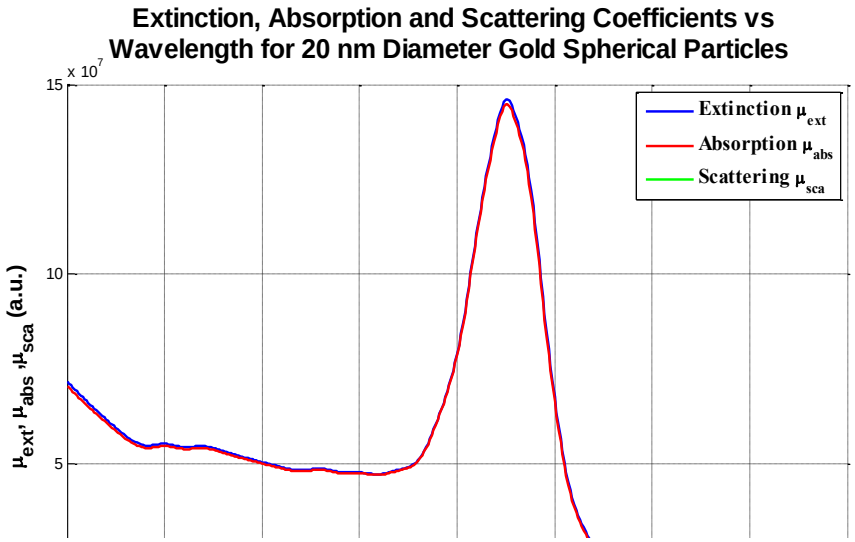

(a)

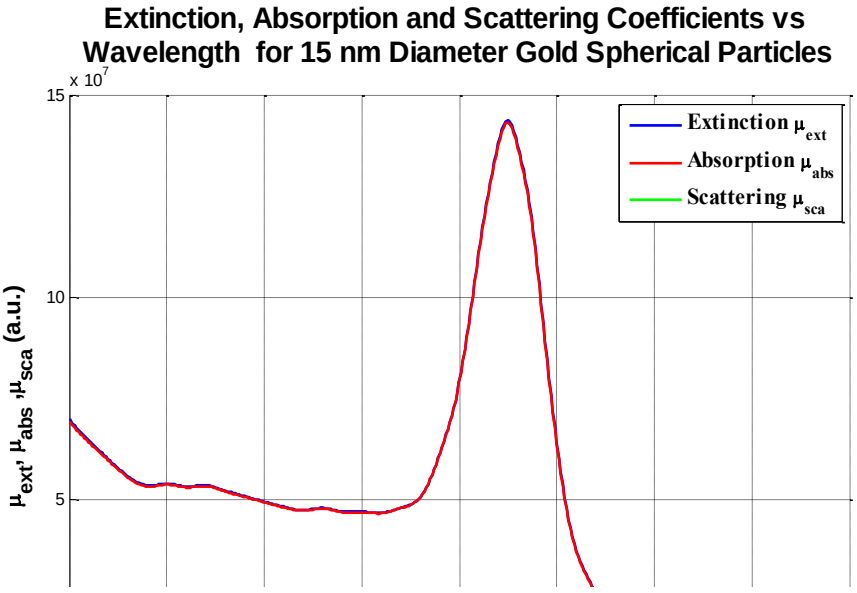

(b)

Figure 3.11 Extinction (blue), Absorption (red) and Scattering (green) coefficients obtained using Mie theory over the wavelength range from 300 nm to 700 nm for a (a) 20 nm and (b) 15 nm gold spherical nanoparticle solution

3.5. Numerical Analysis of the Optical Properties of Gold Nanorods

The analysis performed on the spherical particles using Mie theory has provided more insight into the dependence the size of the particle has on the SPR peaks and has also provided critical sysnthesis and experimental parameters for the characterization schemes developed in this thesis. A similar analysis with the same objective for the optical properties of GNRs is presented in this section.

Mie's theory was developed for particles of a spherical nature only. To study the optical properties of the nanorod structures an extension of Mie theory, first developed by Gans [3.19-3.20], has been adapted and is used to explore the behavior of gold nanorods in the dipole approximation. The dependence of the most critical nanorod parameters, such as: aspect ratio, dielectric constant on the position of the SPR peaks has been investigated. An analysis on the dependence of the absorption and scattering, calculated separately, based on the size of the nanorods has also been carried out. Careful selection of the nanorod properties allows specific wavelength tuning of the optical attenuation peaks and provides critical information for the synthesis of particles used as optical contrast agents that are based on absorption. As in the previous case for the spherical particles, key information for the experimental characterization schemes is also provided.

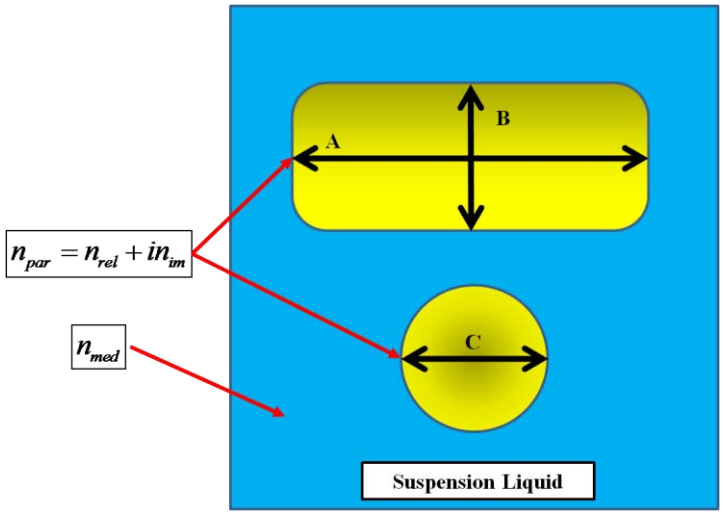

Figure 3.12 GNR of refractive index $n_{par} = n_{rel} + in_{im}$,where the B axis is equal to the C axis and A represents the length of the GNR, in suspension liquid with refractive index n_{med} .

According to Gans, the extinction coefficient of randomly oriented ellipsoidal (or rod) can be modeled by introducing a geometrical factor P_j which corresponds to each axis *A*, *B* and *C* of the particle (see Figure 3.12). The modified formulas for the absorption and scattering cross sections, σ_{abs} and σ_{sca}, respectively, are given as [3.13, 3.19]:

$$\sigma_{abs} = \frac{2\pi V \varepsilon_{med}^{3/2}}{3\lambda_0} \sum_{j=A}^{C} \frac{\left(\frac{1}{P_j^2}\right)\varepsilon_{imag}}{\left[\varepsilon_{real} + \left(\frac{1-P_j}{P_j}\right)\varepsilon_{med}\right]^2 + \varepsilon_{imag}^2} \tag{3.5.1}$$

$$\sigma_{sca} = \frac{8\pi^3 \varepsilon_{med}^2 V^2}{9\lambda_0^4} \sum_{j=A}^{C} \frac{\left(\varepsilon_{real} - \varepsilon_{med}\right)^2 + \frac{\varepsilon_{imag}^2}{P_j^2}}{\left(\varepsilon_{real} + \left(\frac{1-P_j}{P_j}\right)\varepsilon_{med}\right)^2 + \varepsilon_{imag}^2} \tag{3.5.2}$$

Where *V* is the volume of the particle, ε_{med} represents the dielectric constant of the surrounding medium, ε_{real} and ε_{imag} represent the real and imaginary part of the complex dielectric function of gold, respectively. To convert the refractive index to the equivalent dielectric constants the following relations have been used:

$$\varepsilon_{real} = n_{real}^2 - n_{imag}^2 \tag{3.5.3}$$

$$\varepsilon_{imag} = 2 n_{real} n_{imag} \tag{3.5.4}$$

To study the effect of elongated ellipsoids, or rods, the *B* and *C* axis are set equal and correspond to the nanorod short-axis diameter, the *A* term represents the length *L* of the nanorod (see Figure 3.12). The geometrical P_j factors along the A and B/C axis are defined as [3.19]:

$$P_A = \frac{2}{R^2 - 1}\left[\frac{R}{2\sqrt{R^2-1}} \ln\left(\frac{R + \sqrt{R^2-1}}{R - \sqrt{R^2-1}}\right) - 1\right] \tag{3.5.5}$$

$$P_B = P_C = \frac{1 - P_A}{2} \tag{3.5.6}$$

Where *R* is the aspect ratio of the particle and is given by:

$$R = A / B \tag{3.5.7}$$

3.5.1. Influence of Aspect Ratio on LSP wavelength peak

To inspect the affect the aspect ratio has on the optical properties of the gold nanorods, the medium dielectric constant in equations (3.5.1) and (3.5.2) is fixed to $\varepsilon_{med} = 4$ and the aspect ratio, *R*, is varied over the range from 2.6 to 3.6. An additional comparative analysis has also been performed by taking both the real and imaginary dielectric constants from the experimental data provided by both Weaver and Frederikse [3.15] and Johnson and Christy [3.14] separately (see Figure 3.5). The objective of this comparative analysis is to demonstrate the affect slight changes in the refractive index of the gold particles have on the outcome.

The spectroscopic profile for the extinction coefficient, $\mu_{ext} = \mu_{abs} + \mu_{sca}$, over the wavelength range from 400 nm to 900 nm is presented in Figure 3.13 (a) for the data from Weaver and Frederikse and (b) for Johnson and Christy. It can be seen that as the aspect ratio of the nanorod increases the position of the LSP peak shifts to longer wavelengths and increases in amplitude, and that the TSP moves to shorter wavelengths and decreases in amplitude. The effect however, is more dramatic for the LSP peak.

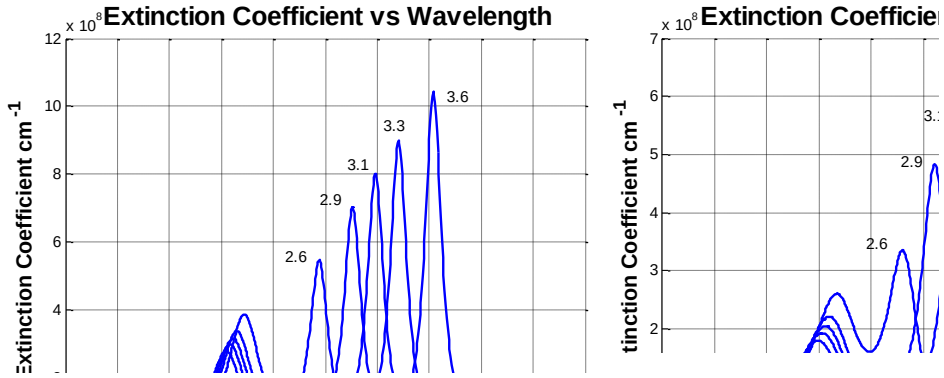

(a) **(b)**

Figure 3.13 Extinction coefficient, $\mu_{ext} = \mu_{abs} + \mu_{sca}$, of GNR for aspect ratios ranging from 2.6 to 3.6 and a constant medium dielectric constant of, $\varepsilon_{med} = 4$ over the wavelength range from 400 nm to 900 nm using particle refractive index from (a) Weaver and Frederikse and (b) Johnson and Christy.

The dependence the aspect ratio has on the position of the LSP peak is presented in Figure 3.14 (a) and (b) using data obtained from Figure 3.13 (a) and (b), respectively. It

may be observed that there is a linear relation between both of these terms. This linear behavior is in agreement with similar work carried out by other authors [3.13, 3.19]. The relation between the wavelength peak, λ_{peak}, and aspect ratio, R, when the refractive index of the surrounding medium, n_{med}, is constant and the refractive index of the gold particles, $n_{particle}$, is taken from Weaver and Frederikse, see Figure 3.5, can be described by:

$$\lambda_{peak} = 110.04R + 357.71 \tag{3.5.8}$$

And when the refractive index of the particle, $n_{particle}$, is taken from experimental work by Johnson and Christy, Figure 3.5, by:

$$\lambda_{peak} = 107.14R + 350.78 \tag{3.5.9}$$

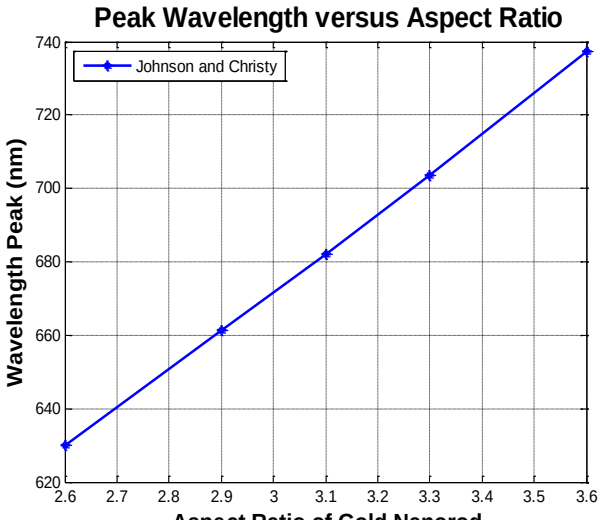

(a) **(b)**

Figure 3.14 Peak wavelength of the LSP versus the aspect ratio extracted from the numerical analysis from (c) Weaver and Frederikse and (d) Johnson and Christy.

From the plots in Figure 3.13 the sensitivity of the spectral response to differences in the refractive index can be appreciated. The position of the LSP, λ_{peak}, from the data supplied by Weaver and Frederikse is observed to be greater than that from Johnson and Christy. A summary of these properties for each aspect ratio analyzed is presented in Table 3.1 where the wavelength difference, $\Delta\lambda_{peak}$, ranges from 14.1 nm to 17.1 nm.

Aspect Ratio R	λ_{peak} (LSP) Weaver and Frederikse	λ_{peak} (LSP) Johnson and Christy	$\Delta\lambda_{peak}$
2.6	644.2 nm	630.1 nm	14.1 nm
2.9	676.4 nm	661.3 nm	15.1 nm
3.1	698.6 nm	682.0 nm	16.6 nm
3.3	720.8 nm	703.7 nm	17.1 nm
3.6	754.1 nm	737.4 nm	16.7 nm

Table 3.1 Wavelength peak obtained from gold using the two different refractive indices values from experimental work by Weaver and Frederikse and Johnson and Christy for changing aspect ratios and for a constant surrounding medium dielectric constant $\varepsilon_{med} = 4$.

3.5.2. Influence of Medium Dielectric Constant on the LSP wavelength peak

In this section the influence the dielectric constant of the surrounding medium has on the spectroscopic response will be presented. To perform this analysis the aspect ratio in equations (3.5.5), (3.5.6) and (3.5.7) is maintained constant at $R = 3.3$, and the medium dielectric constant, ε_{med}, is varied over the range from 2.5 to 4.5. Again a comparative analysis is also provided for the real and imaginary dielectric constants, ε_{real} and ε_{imag}, respectively, from the experimental data presented in Figure 3.5 from both Weaver and Frederikse and Johnson and Christy.

The spectroscopic profile of the extinction coefficient, $\mu_{ext} = \mu_{abs} + \mu_{sca}$, over the wavelength range from 400 nm to 900 nm is presented in Figure 3.15 (a) for the data from Weaver and Frederikse and (b) for Johnson and Christy. It can be seen that as the medium dielectric constant increases the position of the LSP peak shifts to longer wavelengths and increases in amplitude, and that the TSP moves to shorter wavelengths and decreases in amplitude. Again, the effect is more dramatic for the LSP peak.

Figure 3.15 Extinction coefficient, $\mu_{ext} = \mu_{abs} + \mu_{sca}$, of GNR for medium dielectric, ε_{med}, ranging from 2.5 to 4.5 and for a constant aspect ratio of $R = 3.3$ over the wavelength range from 400 nm to 900 nm using particle refractive index from (a) Weaver and Frederikse and (b) Johnson and Christy.

The dependence the dielectric constant of the surrounding medium has on the position of the LSP peak is presented in Figure 3.16 (a) and (b) using data obtained from Figure 3.15 (a) and (b), respectively. It may be observed that there is a linear relation between both of these terms. The relation between the wavelength peak, λ_{peak}, and the dielectric constant of the surrounding medium, ε_{med}, when the aspect ratio, *R*, is held constant and the refractive index for the gold particle, $n_{particle}$, is taken from Weaver and Frederikse (see Figure 3.5) can be described by:

$$\lambda_{peak} = 60.52\varepsilon_{med} + 477.92 \tag{3.5.10}$$

and when the refractive index of the particle, $n_{particle}$, is taken from experimental work by Johnson and Christy (see Figure 3.5) by:

$$\lambda_{peak} = 58.4\varepsilon_{med} + 470.01 \tag{3.5.11}$$

Again this linear behavior is in agreement with work presented by other authors [3.19].

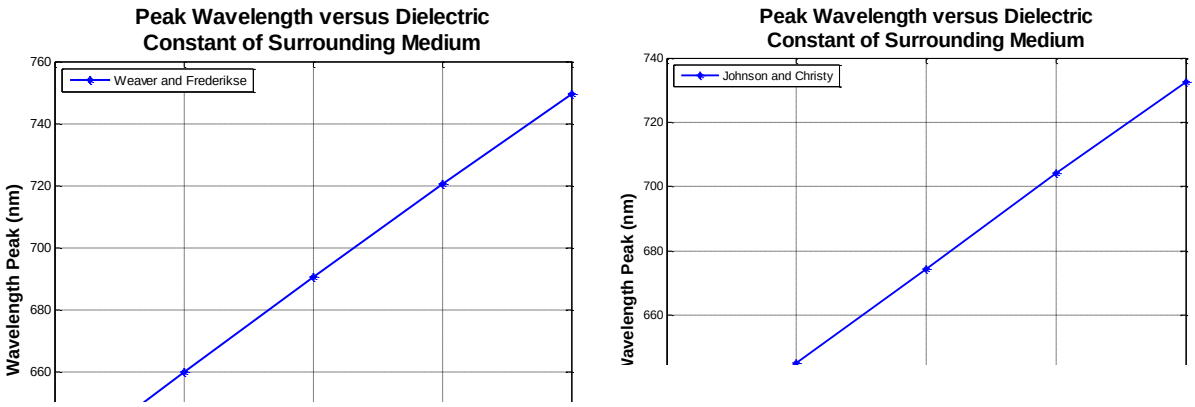

(a) **(b)**

Figure 3.16 Peak wavelength of the LSP versus the aspect ratio extracted from the numerical analysis from (c) Weaver and Frederikse and (d) Johnson and Christy.

From the plots in Figure 3.15 the sensitivity of the spectral response to differences in the refractive index can again be appreciated. As in the previous case, Section 3.5.1, the position of the LSP, λ_{peak}, from the data supplied by Weaver and Frederikse is observed to be greater than that from Johnson and Christy. This particular feature has also been observed by [3.21]. A summary of these properties for each medium dielectric constant is presented in Table 3.2 where the wavelength difference, $\Delta\lambda_{peak}$, ranges from 12.5 nm to 17 nm.

Medium Dielectric Constant ε_{med}	**λ_{peak} (LSP) Weaver and Frederikse**	**λ_{peak} (LSP) Johnson and Christy**	**$\Delta\lambda_{peak}$**
2.5	628.6 nm	616.1 nm	12.5 nm
3	659.7 nm	645.1 nm	14.6 nm
3.5	690.4 nm	674.3 nm	16.1 nm
4	720.5 nm	704.2 nm	16.3 nm
4.5	749.5 nm	732.5 nm	17 nm

Table 3.2 Wavelength peak obtained from gold using the two different refractive indices values from experimental work by Weaver and Frederikse and Johnson and Christy for varying dielectric constants of the surrounding medium and for a fixed aspect ratio (R = 3.3).

3.5.3. Influence of Nanorod dimensions on the Absorption and Scattering coefficients

Throughout this thesis it has been seen that the efficiency of optoacoustic signal generation is dependent on the amount of optical energy absorbed. In the previous sections the location of the wavelength attenuation peak has been characterized by studying the aspect ratio and medium dielectric constant. In this section a review of the influence the size of the gold nanorod has on the absorption and scattering properties will be performed. This analysis will indicate design parameters for the experimental setup used to determine the spectral profile by means of the optoacoustic technique. This examination also provides information required for the synthesis of highly absorbing gold nanorod solutions required for optoacoustic detection of optical contrast agents in biomedical applications.

3.5.3.1. Nanorod Diameter

To study the effect the short axis, or diameter, of the nanorod, (B and C in Figure 3.12), has on the both the absorption and scattering properties, the surrounding medium dielectric constant and the aspect ratio are maintained constant, $\varepsilon_{med} = 4$ and $R = 3.3$, respectively. The refractive index properties of the gold particles have been taken from Weaver and Frederikse (see Figure 3.5). The optical attenuation has been investigated for diameters of the nanorods (B, C) between 10 nm and 80 nm, where the corresponding length, (A in Figure 3.12) is calculated using equation (3.5.7). The results are presented in Figure 3.17 for the extinction, absorption and scattering coefficients, where:

$$\mu_{ext} = \frac{\sigma_{ext}}{V}, \mu_{abs} = \frac{\sigma_{abs}}{V}, \mu_{sca} = \frac{\sigma_{sca}}{V} \tag{3.5.12}$$

And the volume $V = \pi\left(B/2\right)^2 \cdot A$, (see Figure 3.12). The results provide insight into the evolution of the attenuation coefficients over the wavelength range from 400 nm to 900 nm.

Figure 3.17 Extinction μ_{ext} , Absorption μ_{abs} and scattering μ_{sca} over the spectral range from 400 nm to 900 nm for increasing nanorod diameters ranging from 10 nm to 80 nm and a constant aspect ratio and surrounding medium dielectric medium of $R = 3.3$ and $\varepsilon_{med} = 4$, respectively.

It may be observed from Figure 3.17 that as the diameter of the nanorod increases the ratio between the scattering and the absorption coefficient is also seen to increase. Note that the position of both the LSP and the TSP are constant, this is a result of maintaining the values for the aspect ratio and dielectric constant of the surrounding medium fixed. Another important feature that can be observed in each graph is that the absorption coefficient remains constant (see equations (3.5.1) and (3.5.12)) and that the scattering coefficient is directly proportional to the volume of the nanorod (see equations (3.5.2) and (3.5.12)). The fluorescence efficiency is commonly used to quantify the amount of scattered light from the total incident light and is defined as the ratio of scattered light to the total extinction of light and is given by [3.4]:

$$\varphi_s = \frac{\mu_{sca}}{\mu_{ext}} \tag{3.5.13}$$

A plot of the fluorescence efficiency versus the diameter of the short nanorod axis is presented in Figure 3.18. Here it may be observed that the scattered light increases with increasing nanorod short axis diameter.

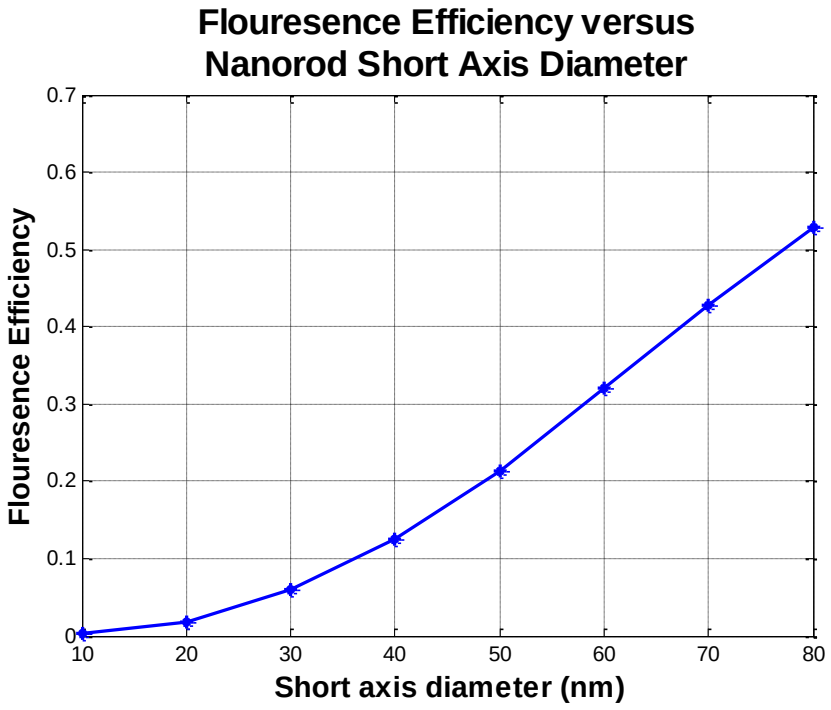

Figure 3.18 Fluorescence efficiency versus particle diameter, data taken for particles ranging in diameter from 10 to 80 nm, for a medium dielectric constant of 4 and Aspect ratio 3.3.

3.5.3.2. Nanorod Length

To study the effect the long axis, or length, of the nanorod, (A in Figure 3.12), has on the both the absorption and scattering properties, the surrounding medium dielectric constant and the aspect ratio are again maintained constant at the same values of $\varepsilon_{med} = 4$ and $R = 3.3$, respectively. Again the refractive index properties of the gold particles have been taken from Weaver and Frederikse (see Figure 3.5). The length of the nanorods (A) has been investigated over a range of 20 nm to 250 nm, where the corresponding diameter, (B, C in Figure 3.12) is calculated using equation (3.5.7). The results are presented in Figure 3.20 for the extinction, absorption and scattering coefficients (see equation (3.5.12))

It may be observed from Figure 3.20 that as the length of the gold nanorod increases the ratio between the scattering and the absorption coefficient is also seen to increase. Similar conclusions may be extracted from the fluorescence efficiency versus the nanorod length presented in Figure 3.19.

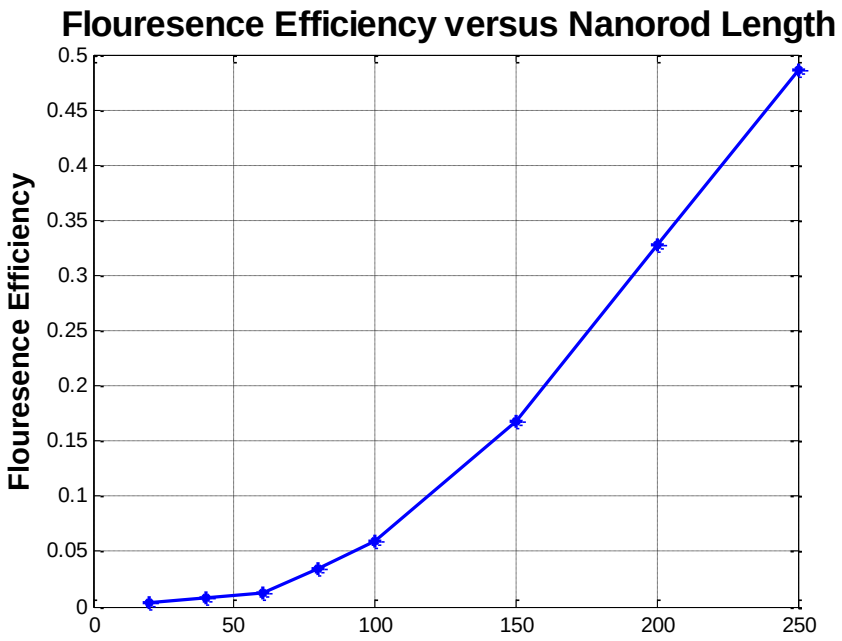

Figure 3.19 Fluorescence efficiency versus particle diameter, data taken for particles ranging in length from 20 to 250 nm, for a medium dielectric constant of 4 and Aspect ratio 3.3

Figure 3.20 Absorption and scattering effects for a constant aspect ratio of R = 3.3 and constant surrounding dielectric medium of $\varepsilon_{med} = 4$. The optical parameters were obtained for the long axis of the nanorod ranging from 10 nm to 250 nm.

3.6. Conclusions

In this chapter the optical attenuation parameters, defined in Chapter 2, have been investigated for gold nanostructures that are currently finding applications in the biomedical industry as contrast agents for *in-vivo* optical based diagnostic techniques and as localized absorbers for improved phototherapy. The phenomenon associated with the Surface Plasmon Resonance (SPR) of such particles has been identified as the principle mechanism behind their clearly defined spectral profiles. The SPR is directly related to the material properties of the particles, their surrounding medium, their shape and size.

The optical properties of SGNPs have been investigated using Mie Theory and an extension of Mie theory developed by Gans for GNRs. This numerical analysis has considered the most important particle parameters such as, particle size, particle dimensions, particle refractive index and also the effect of the surrounding medium. The results obtained have been compared to numerical studies performed by other authors and agreement has been observed.

It has been demonstrated that for spherical gold particles with a diameter of less than 20 nm that absorption is dominate and the contribution of the scattering component to the total extinction may be ignored. For GNRs the influence of the diameter of the short axis and length of the long axis has been investigated for a constant aspect ratio of $R = 3.3$ and surrounding medium dielectric constant of $\varepsilon_{med} = 4\,4$ where it has been demonstrated that for short axis diameters of less than 30 nm and long axis lengths of less than 80 nm the absorption of light is dominant.

The information provided in this chapter has provided vital information regarding the dimensions of nanoparticle particles that are best suited for optoacoustic signal generation and that should be considered during their synthesis. The key conditions for the experimental optoacoustic characterization schemes presented in this thesis have also been identified, such as their optical attenuation properties, wavelength range of interest for spectroscopic measurements, and the position of the main absorption peaks.

Chapter 4.

Concept and Design of a Novel Optoacoustic System for Spectroscopy Measurements of Gold Nanoparticles.

4.1. Introduction

The design of two different optoacoustic schemes for the quantification and spectral resolution of colloidal gold solutions embedded in a scattering medium are presented in this chapter. Although the optoacoustic measurement schemes presented here may be applied to any chromophore located within the therapeutic window, the work performed in this thesis has addressed the lack of quantitative information on highly absorbing gold nanoparticle solutions embedded within scattering media.

This chapter begins with a discussion on the measurement concepts commonly used to extract information from the optoacoustic signals generated during the interaction of short pulsed laser light with absorbing materials. This is followed by a review of optical soft tissue phantoms and includes a description of the scattering medium used in the experimental trials carried out in this thesis.

The first experimental scheme has been designed to quantify the optical absorption of a nanoparticle solution embedded in a scattering medium using the optoacoustic signals generated from a laser source operating at a single wavelength of 532 nm. The experimental results obtained from this scheme have motivated the implementation of a second spectroscopic scheme used to identify the properties of gold nanoparticles over the wavelength range from 410 nm to 1000 nm. The parameters required for an accurate analysis using these systems for both spherical gold nanoparticle (SGNP) and gold nanorod (GNR) solutions have been identified from the theoretical analysis presented in Chapter 3. In particular, the ideal source wavelength for efficient optoacoustic signal generation in the first scheme, which has been defined from the position of the SPR absorption peak, and the wavelength range of interest for the spectroscopic measurement in the second scheme.

Details will also be provided on the design of a reference measurement scheme, based on collimated optical transmission, which has been setup in parallel and under the same experimental conditions for both optoacoustic schemes. This has been used for a comparative analysis of the results obtained and to verify the feasibility of the optoacoustic technique for quantitative and spectral measurements.

4.2. Optoacoustic Measurement Concepts

The optoacoustic technique has received considerable interest in the field of biomedical diagnostics due to its non-invasive and real time imaging of tissue abnormalities located within the scattering confines of healthy soft tissue [4.1-4.3]. From knowledge of the speed of sound in the medium, v_{med}, a time of flight (TOF) analysis can provide the location of absorbers in the scattering medium or biological medium [4.4]. These spatially resolved acoustic signals are back projected forming images of the internally absorbed laser energy distribution. Details of this process may be observed in Figure 4.1 where the optoacoustic signals obtained from three spherical absorbers in a scattering dominant medium are presented. Note that as the optical energy propagates in the scattering medium it is attenuated reducing the amount laser energy available for absorption by the spherical targets. This reduction in absorbed energy affects the amplitude of the acoustic transients generated.

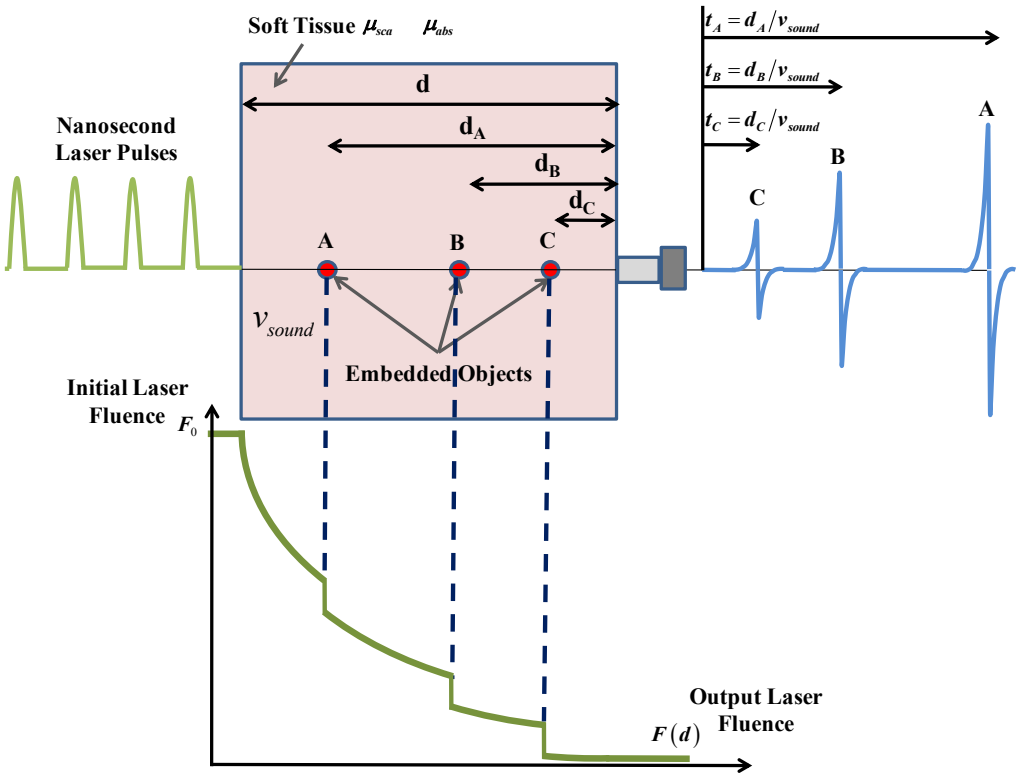

Figure 4.1 Optoacoustic signal generation of three embedded objects in soft tissue with speed of sound, v_{sound}.

The acoustic transients generated during optical irradiation contain valuable information on the optical properties of mediums. A method which has been adapted in [4.5] has

been to study the exponential slope of the acoustic transients generated by an absorber and by applying beers law (see equation (2.4.9) and Figure 4.2). This quantification method has been used *in-vitro* for non-invasive monitoring of blood oxygenation [4.6]. To extract the information from the pressure waves a calibrated wideband transducer is required.

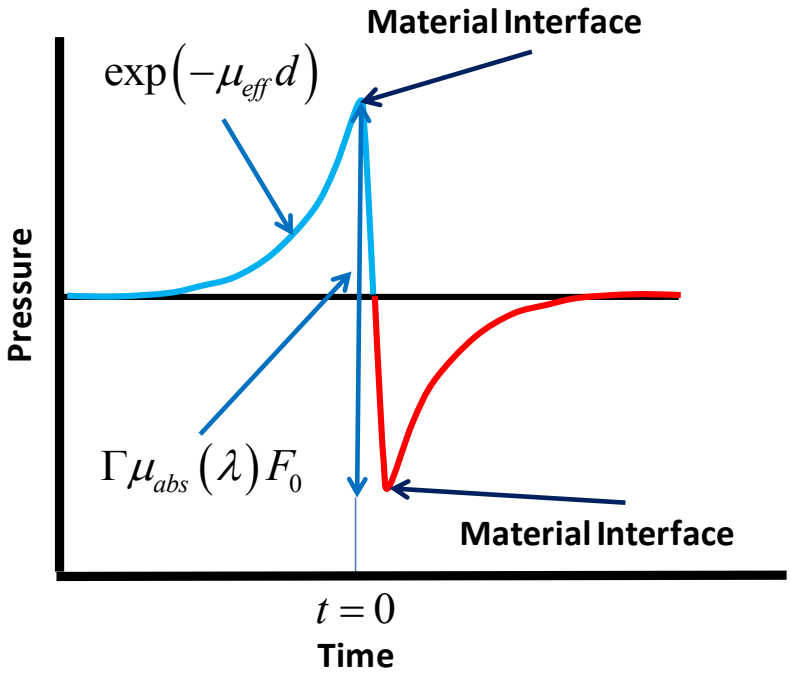

Figure 4.2 optoacoustic signal detected using a wideband acoustic transducer sensor.

It has been shown in Chapter 2 that the initial amplitude of the optical induced pressure transients are wavelength dependent and directly proportional to the initial laser fluence on the absorber, F_0 , the absorption coefficient of the target medium, μ_{abs}, and, Grüneisen coefficient, Γ, (see Figure 4.2). Thus, the absorption coefficient can be determined by analyzing the dependence of the initial amplitude of the pressure transient on the laser fluence incident on the absorber. This feature has been adapted in the optoacoustic schemes presented here for the quantification and spectral resolution of the gold nanoparticle solutions embedded in a scattering medium. This particular analysis has been performed in [4.7] to spectrally resolve gold nanoparticle contrast agents in a rat model, however this analysis has been limited to only three separate wavelengths (757 nm, 807 nm and 820 nm) and no quantitative information is directly extracted from the acoustic signals. Further descriptions of optoacoustic experiments

performed by other authors to quantify the optical properties of absorbers are presented in Appendix E.

4.3. Optical Tissue Phantom Construction

There is constant growth in the used of optical based methods for biomedical applications. This is due to the advantages they pertain over traditional methods, which are; the use of non-ionizing radiation, the capability of measuring functional (physiological) changes, the potential high sensitivity to pathologic state biological tissue and low cost. Diseased tissues are in most cases embedded within healthy human soft tissue which is highly attenuating to optical energy. To ensure the viability of optical techniques for biomedical applications it is essential to mimic the optical properties of human soft tissue.

It has been seen in Chapter 2 that the attenuation of light in healthy soft tissue is dominated by scattering. This is occurs because of the interaction of light with complex microscopic cellular structures that may be interpreted as scattering particles with a broad size distribution. From the theoretical analysis in Chapter 3 it has been shown using Mie theory that for particles greater than 80 nm optical scattering is dominant. As a result, materials used to simulate the optical properties of tissues commonly consist of a suspension of particles ($\gg 80nm$) in a solid or liquid. Selection of appropriate concentrations of the scattering materials enables the reduced scattering coefficient, $\mu_{sca}^{'}$, which simulates healthy soft tissue to be obtained.

Examples of scattering materials include solid particles suspended in polymer resin. In [4.8-4.9] the authors have used spherical polymer resin particles with diameters of 270 nm embedded in resin and in [4.5] polystyrene particles of 900 nm in diameter embedded in gel. Other materials commonly used for tissue phantoms in optical and optoacoustic trials are fat emulsions, commonly referred to as Intralips, named after the first fat emulsion brand approved for human use [4.10-4.13]. The particle diameters are dependent on the fat concentration and can be as high as 1 μm [4.14].

Other liquid phantoms which simulate the strong scattering of healthy human tissue are based on different concentrations of whole milk [4.15-4.19]. Milk is mainly composed of both fat and proteins. The fat spheres have diameters ranging from 0.5 μm to 20 μm where the majority of the particles lie in the range from 2 μm to 4 μm. The protein

particles fall in the range of 0.02 μm to 1 μm. Due to the size of the particles high levels of Mie scattering and very low levels of absorption are produced [4.20]. Owing to the large variation in particle size distribution, where each milk brand and batch from the same brand have different optical properties. This fact is reflected in reported quantitative results where values for the reduced scattering coefficient range from 0.375 cm^{-1} at 680 nm [4.21] to 12 cm^{-1} at 532 nm [4.22].

The strong scattering optical tissue phantom used in the experimental trials presented in this thesis has been based on different volumes of whole milk in distilled water. The optical properties of the milk solution have been characterized for each experimental setup. This has helped to ensure the feasibility of the optoacoustic technique as a method of determining the optical parameters and spectroscopic profiles of absorbers embedded within a scattering media.

4.4. Experimental Setup for Quantitative Measurements of the Absorption Coefficient of a Synthesized SGNP at a Single Laser Wavelength of 532 nm.

4.4.1. Introduction

In this section a description of the experimental setup designed to perform a quantitative measure of the optical parameters of a synthesized SGNP solution will be presented. The experimental setup is based on a parallel measurement which includes both the optoacoustic and collimated optical transmission schemes. The latter is used as a reference measurement to confirm the results, thus feasibility, of the optoacoustic technique.

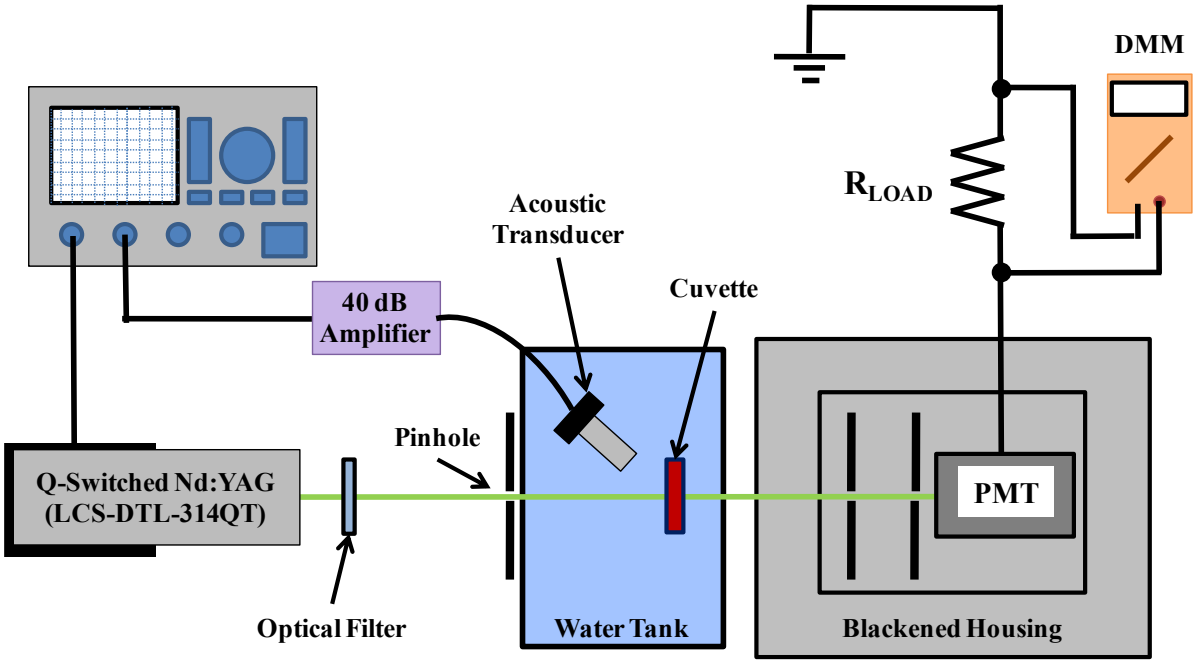

Figure 4.3 Experimental scheme for the characterisation of a SGNP solution showing the collimated optical transmission reference scheme in parallel with the optoacoustic characterisation technique.

A schematic showing all the major components of the experimental system is presented in Figure 4.3. The laser source used for both measurement techniques is a Q-switched Nd:YAG laser (LCS – DTL – 314QT) which emits at both 1064 nm and 532 nm (1st and 2nd harmonic). The 1064 nm is filtered so that only the 532 nm wavelength enters a tank

containing the liquid phantom and absorbing solution. The optical pulses from the laser source have a pulsewidth of 10 ns at a repetition rate set to 40 Hz. The fluence of the laser is determined experimentally to be 2.54 mW/cm^2. This laser is air cooled and the power has been monitored using an optical power meter over extended periods of time to ensure the stability of the laser system.

4.4.2. Collimated Optical Transmission Reference Measurement Scheme.

Collimated optical transmission is used to detect the light which traverses the tank containing the strong scattering tissue phantom and pure absorber solution. Due to the high levels of optical attenuation from both media a highly sensitive photomultiplier tube (PMT) is used to detect the light at the output. The responsivity of this device is 3.9 x 10^4 A/W and it has an optical response threshold of 0.5 pW. The output of the PMT is connected to an 80 KΩ resistor and voltmeter (labeled DMM, digital multimeter) in parallel. Due to the high sensitivity of the optical detector many precautions have been taken into consideration to isolate the detector from all external light sources. The PMT has been placed within a blackened housing sealed on all sides to avoid external light from the laboratory incident on the detector.

The validity of this measurement scheme is based on the assumption that the detected scattered light is negligible when compared to the detected unscattered light. The two main factors that affect this assumption is the scattering angle of the light leaving the tank containing the sample and surrounding medium and the collection angle of the optical detector [4.23-4.24]. To ensure the light reaching the detector is free from forward scattered light a series of 1 mm diameter pinholes have been placed at the output of the tank in the optical path of the laser input with a separation between them of $L = 10\,\text{cm}$ as shown in Figure 4.4. Assuming a scattering angle typical of soft tissue of $\theta = 26^{\circ}$ which corresponds to a anisotropy factor of $g = 0.9$, i.e. $g = \langle \cos(\theta) \rangle$, the diameter of the spot at the second pinhole (at L = 10 cm) would be $D = 9.75\,\text{cm}$, i.e. $D = 2L\tan(\theta)$ giving an area of $A = 74.66\,(\text{cm}^2)$. Using a pinhole diameter of 1 mm, i.e. area $A_{pinhole} = 0.008\,(\text{cm}^2)$ would remove 99.9 % of the forward scattered light.

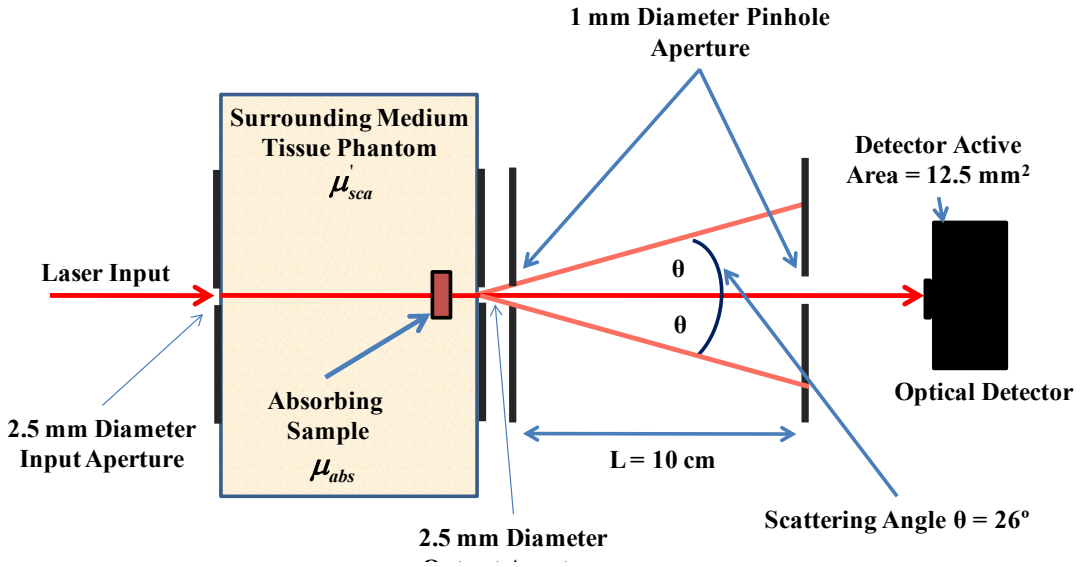

Figure 4.4 Pinhole configuration to reduce the forward scattering light from the tank containing the tissue phantom and absorber entering the optical detector.

The housing containing the optical detector and two pinhole aperture system have been placed within another sealed blackened housing to ensure that the external light is removed. This tank containing the liquid phantom and sample has been blackened on all sides (including top and bottom), see Figure 4.5, this avoids any stray reflections from external light sources. The tank contains a small aperture (2.5 mm diameter) at both the input and output and the sample was located at a distance of 45 cm from the PMT. The absorbing sample is contained within a quartz cuvette with an optical path distance of 1 mm.

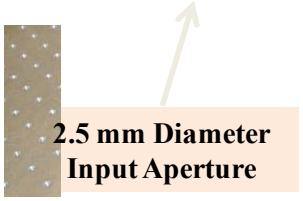

Figure 4.5 Blackened tank containing liquid phantom and absorbing solution.

4.4.3. Optoacoustic Measurement Scheme.

The experimental setup shown in Figure 4.3 also shows the optoacoustic characterization scheme. The acoustic transducer which detects the optically induced stress waves is an immersion 10 MHz resonant transducer (V327, Panametrics, see Figure 4.6). An immersion transducer has been used to optimize the acoustic impedance between the sample and the transducer via the liquid phantom. The output of the transducer is connected to a 40 dB amplifier (5328 Panametrics) which is connected to an oscilloscope to capture the signals generated.

Figure 4.6 Resonant immersion acoustic transducer (Panametrics).

The oscilloscope is triggered using an auxiliary output from the laser driver which provides a signal that corresponds to the pulse repetition rate of the laser output. A photograph of the experimental scheme is presented in Figure 4.7.

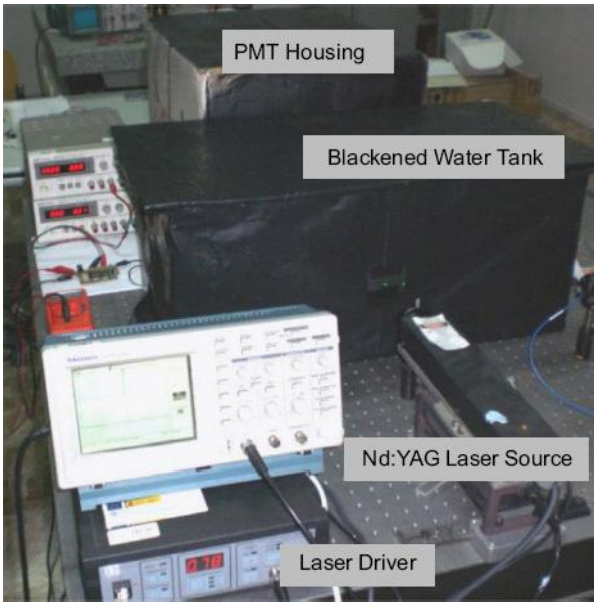

Figure 4.7 Photograph of experimental setup used to determine the optical parameters of an absorbing sample embedded within a liquid phantom.

4.4.4. Characterization Measurement Protocol.

Three different measurement protocols have been employed to quantify the optical absorption of two different solutions. The first solution characterized using the parallel optoacoustic and reference scheme has been based on different concentrations of a known optical absorber. This preliminary trial has been designed to verify the experimental setup and feasibility of the optoacoustic technique for quantification measurements. The second solution is based on different concentrations of a SGNP solution and the final protocol involves the characterization of a SGNP solution embedded within different concentrations of a strong scattering medium based on milk.

4.4.4.1. Known Absorber Measurement Protocol

To confirm the experimental parallel measurement scheme, initial trials have involved the use of a known absorber embedded in an optically clear medium, i.e. distilled water. This solution has been made from different concentrations of an ink solution (Montblanc, Midnight Blue (105194) see Figure 4.8) ranging from 0 % (i.e. distilled water) to 12 % where the diluent used was distilled water.

Figure 4.8 Known pure absorber, Montblanc, Midnight Blue (105194)

First the 1 mm quartz cuvette was filled with distilled water to perform a *zero*, or reference, measurement. The amount of optical power reaching the PMT was calculated using the detectors responsivity and voltage recorded on the voltmeter in parallel with the PMT 80 KΩ load resistance. It was also observed at this point that no optoacoustic signal has been generated from the distilled water solution.

The next step has involved filling the cuvette with the lowest ink concentration (i.e. 1 %) again the optical power received was recorded along with the peak to peak amplitude of the first resonant peak of the optoacoustic signal generated. A TOF

analysis using the laser trigger signal and acoustic signal has been used to confirm the distance between the cuvette and acoustic transducer.

The cuvette is then filled with increasing concentrations of the ink solution and the optical power and acoustic signal amplitude is recorded for each one. In Figure 4.9 a series of optoacoustic signals acquired for different concentrations of the absorbing solution are presented. Finally a measurement has been performed using a 20 % ink concentration to ensure that the minimum optical signal has been measured and the maximum acoustic signal generated. Between each sample measurement the cuvette has been cleaned and dried to ensure that no traces of the ink solution are present.

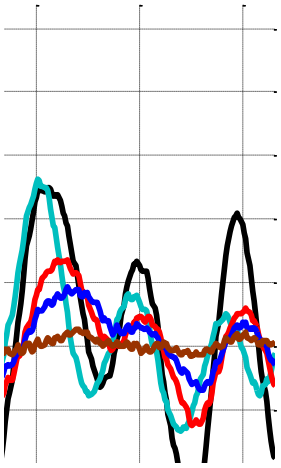

Figure 4.9 Optoacoustic signals generated for different concentrations of the absorbing solution.

4.4.4.2. SGNP Measurement Protocol

The measurement protocol used to quantify the optical properties of a synthesized 20 ± 2 nm diameter absorbing SGNP solution where the dimensions have been confirmed using TEM (see Figure 4.11) is the same as that described in the previous section for the

ink solution in an optically transparent medium. Again all the signals captured by both the optical detector and acoustic transducer are recorded for increasing concentrations of the SGNP solution. To obtain the different concentrations of the SGNP solution, a highly concentration solution (see Figure 4.10 right) was first generated from the stock synthesized solution (see Figure 4.10 left) using centrifugal techniques and by removing the bulk part of the suspension liquid. From this highly concentrated solution 13 different concentrations were made using distilled water as the diluent.

Figure 4.10 Spherical gold nanoparticles synthesized using the Turkevich protocol (left) stock solution (right) concentrated stock solution.

Figure 4.11 Transmission Electron Microscopy (TEM) image of 20 nm spherical gold nanoparticles

4.4.4.3. SGNP Embedded in Liquid Tissue Phantom Protocol.

The main objective of this optoacoustic quantitative measurement scheme has been to determine the optical properties of a nanoparticle absorbing solution embedded in a high scattering medium. In this experiment the protocol for the SGNP solution described previously is used to measure both the optoacoustic signals generated and the

optical power received after light propagation through ten different synthesized 15 ± 2 nm diameter SGNP solution concentrations ranging from 4.2 nM to 42.5 nM. In Figure 4.12 (left) five different concentrations of the SGNP solution are presented along with the TEM results (right). This procedure has been repeated eight times for concentrations of the scattering surrounding medium composed of milk ranging from 0 % to 0.1 %.

Figure 4.12 (Left) five different concentrations of the 15 nm SGNP solution (Right)Transmission Electron Microscopy (TEM) image of 15 nm spherical gold nanoparticles.

4.5. Experimental Setup for Laser Optoacoustic Spectroscopy (LOS) of Gold Nanoparticles.

4.5.1. Introduction

In this section a description of the experimental setup designed to measure spectroscopic profile of two different colloidal gold solutions will be presented. As in the previous design, the parallel optical transmission measurement scheme has been incorporated as a reference. A photograph of the LOS setup is presented in Figure 4.13 where the main components which are described here are presented.

The laser source used for both the optical transmission and optoacoustic schemes is a tunable laser system (Vibrant B 355 II, Opotek) which is a Q-switched Nd:YAG laser-pumped Optical Parametric Oscillator (OPO) (see Figure 4.13). This laser source has a wavelength tunable range from 410 nm to 2400 nm, with a peak OPO energy of 45 mJ at 410 nm and a beam diameter of 6 mm. The temporal width of the optical pulses is 5 ns and operates at a repetition rate of 10 Hz. The spectral linewidth of the optical pulses ranges from 4 to 7 cm^{-1}. For the maximum wavelength (1000 nm) and the maximum linewidth, this corresponds to 0.7 nm.

A specifically designed Matlab™ program has been used to control the wavelength tuning of the laser source, and, provides a complete scan range of 410 nm to 1000 nm in steps of 5 nm. This program also acquires the signal outputs from the optical detector in the collimated optical transmission setup and the transients generated from the optoacoustic technique, allowing a real time comparison of the spectroscopic profiles obtained from each technique.

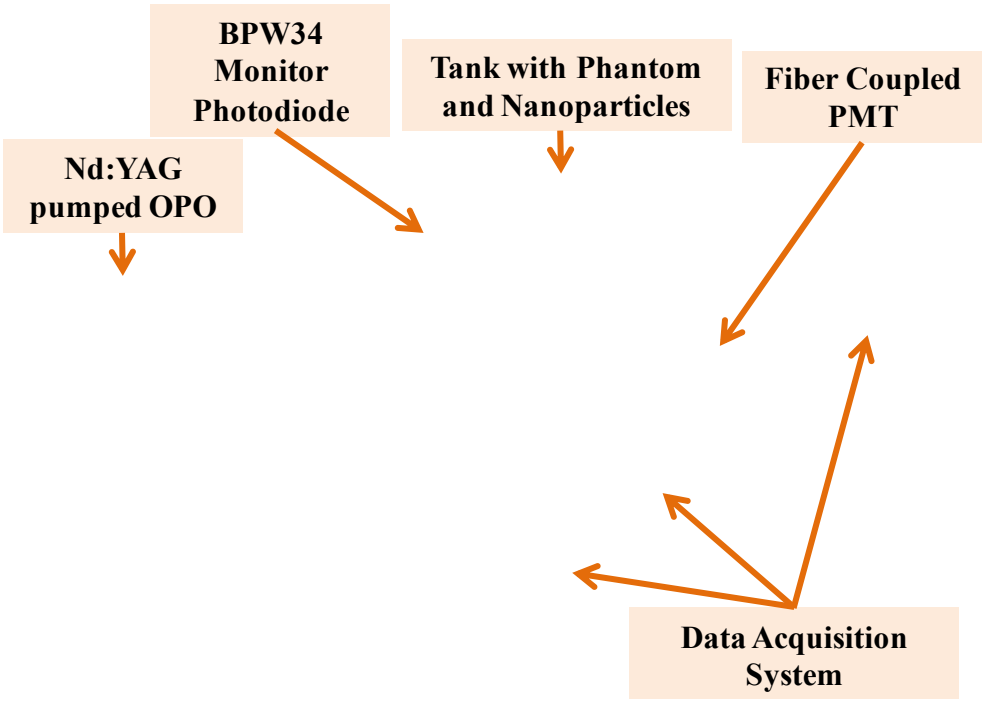

Figure 4.13 Photograph of experimental setup used to determine the spectroscopic response of an absorbing nanoparticle solution embedded within a liquid phantom

4.5.2. Optical Power Monitoring

The optical power at the output of the pulsed laser source has been monitored using the scheme presented in Figure 4.14 which incorporates a glass plate that transmits 96 % of the light and reflects 4 %. A BPW34 pin photodiode with 50 Ω load resistance is used to monitor the pulsed optical output power of the laser. The output of the receiver circuit is connected to an oscilloscope and the data obtained is acquired from this device using the specifically designed Matlab™ software. A series of different signals acquired for four different pulsed wavelength emissions are presented in Figure 4.15.

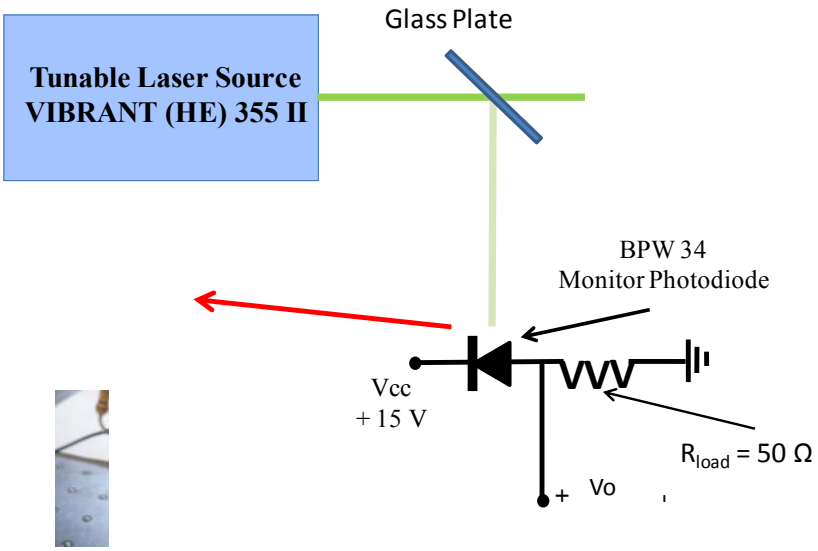

Figure 4.14 Scheme used to monitor the optical power output of the laser source which incorporates a glass plate that transmits 97 % of the light and reflects 3 %. A BPW34 pin photodiode with 50 Ω load resistance is used to convert the optical power received to an electrical signal.

The optical power, P_{OPO} (W), is converted to photocurrent, I_{ph} (A), in function of the responsivity of the detector, $\Re$ (A/W), at each wavelength using the information presented in Figure 4.16 over the range from 410 to 1000 nm in steps of 5 nm, using:

$$P_{OPO}(\lambda) = \frac{I_{BPW34}(\lambda)}{\Re(\lambda)} \tag{4.5.1}$$

This information is stored in the acquisition software and converts the signal obtained to optical power. The signal received by the photodiode over the complete spectral range considered for these experiments is presented in Figure 4.17.

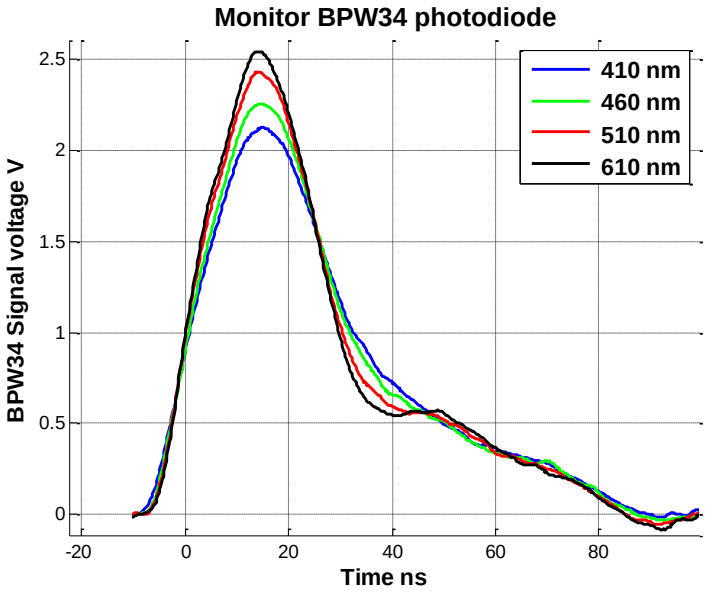

Figure 4.15 Optical pulses acquired using BPW34 monitor photodiode with 50 Ω load for 4 different wavelengths.

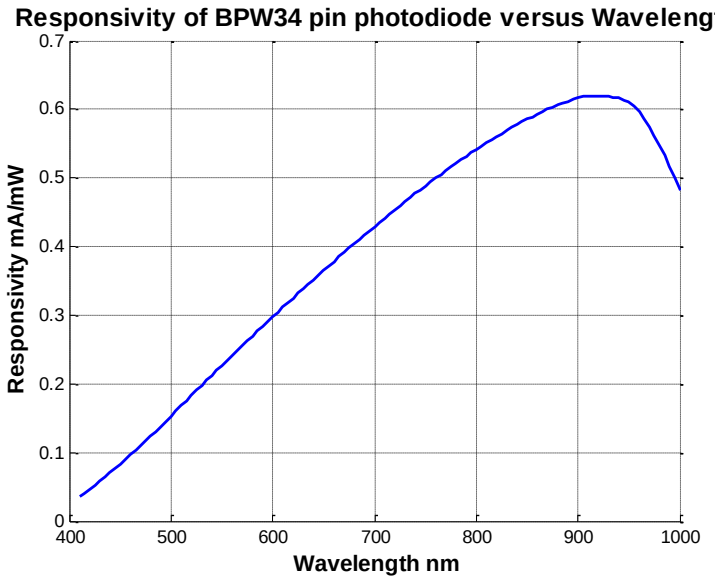

Figure 4.16 Responsivity, $\Re$, of the BPW34 pin photodiode over the wavelength range from 410 nm to 1000 nm.

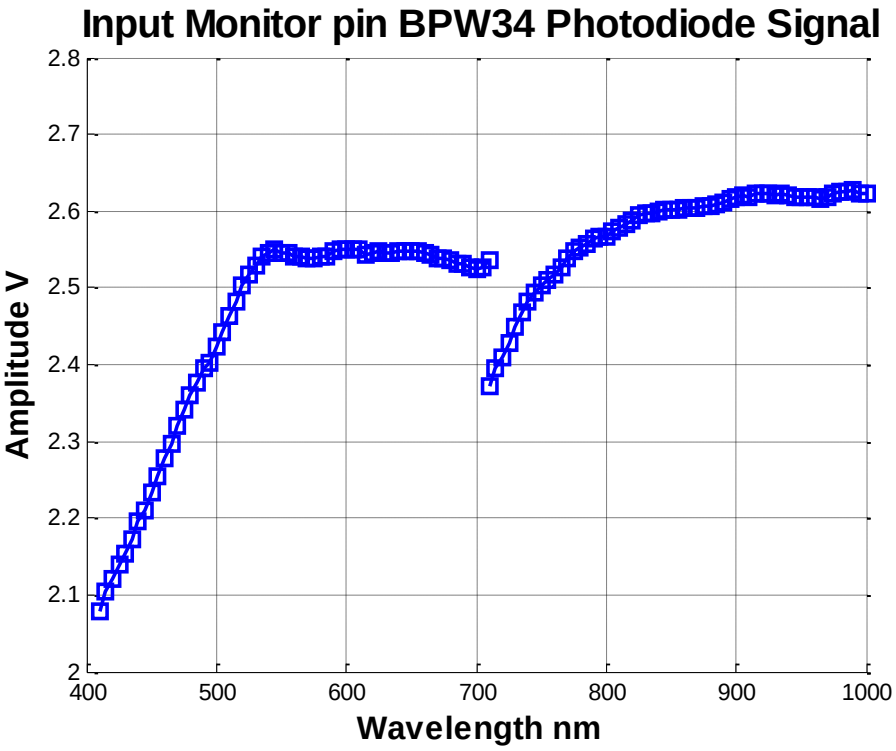

Figure 4.17 Signal received from BPW34 on 50 Ω load over the complete spectral range from 410 nm to 1000 nm acquired in steps of 5 nm.

The increase in the signal voltage from 410 nm to 520 nm is due to the increasing responsivity of the detector. From 520 nm to 700 nm the signal is constant, this is because the decreasing output power of the source compensates the increasing responsivity of the detector. A deviation in the output signal of the monitor photodiode circuit may be observed at 700 nm, see Figure 4.17. This is due to the change in wavelength range of the laser source from signal to idler, provoked by changing the direction of the cube polarizer within the OPO. Using the information provided from Figure 4.16 and Figure 4.17 and equation (4.5.1) the true optical power of the source at each wavelength that enters the tank is measured and presented in Figure 4.18.

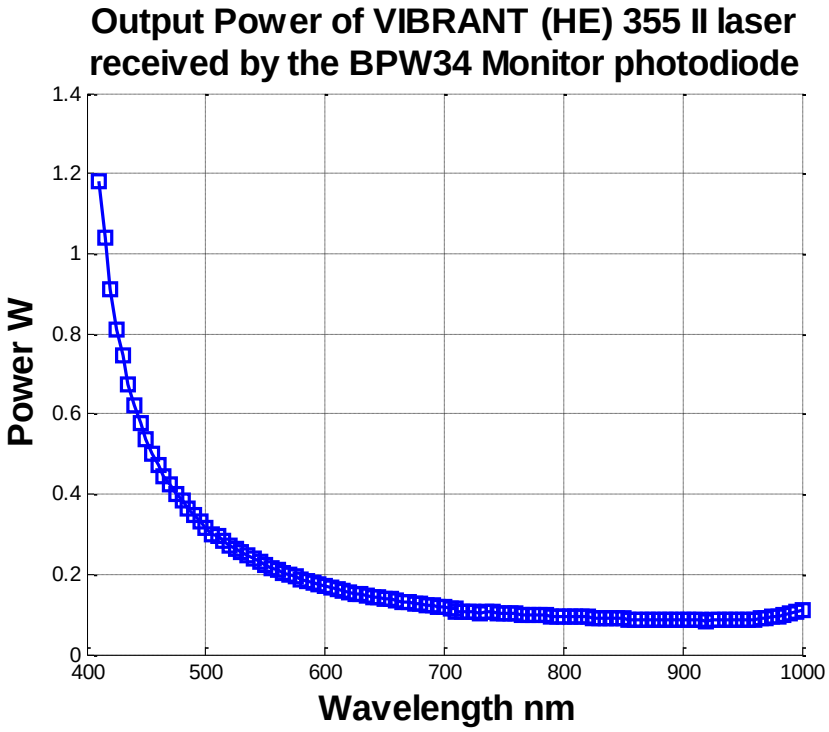

Figure 4.18 Output power of the OPO source received by the photodiode in function of wavelength emission.

4.5.3. Collimated Optical Transmission Reference Spectroscopic Measurement Scheme.

The experimental designs for two different LOS measurement schemes are presented in Figure 4.21 and Figure 4.22 where both systems have the reference measurement scheme incorporated. The main difference between these two schemes is based on the optical detection. The first, (see Figure 4.21), makes use of a BPW34 pin photodiode. The first experimental trials using this scheme has been for the 15 ± 2 nm SGNP solution, where this absorber is embedded in an optically transparent medium (over the wavelength range considered) i.e. distilled water medium. Due to the high energy from the laser source and the absence of the surrounding high scattering medium, the amount of light which propagates through the tank is easily detected using a PIN photodiode. The second scheme (see Figure 4.22) has been designed to measure the spectroscopic profile of a gold nanorod solution embedded in a high scattering material. As a high amount of optical attenuation is expected use has been made of a PMT detector.

Both optical detectors are fiber coupled to a 1 mm core diameter plastic optical fiber (POF), Figure 4.19. This more compact design removes the requirement for bulky sealed blackened housings and the fiber output serves as an input aperture to the

detector to reduce the amount of forward scattered light from the high scattering medium. To increase the accuracy of the measurement the peak to peak signal response of the PMT is taken, as opposed to previous experimental procedures where the average voltage level was taken. This avoids any influences due to baseline drifts. A series of signals obtained by the PMT are presented in Figure 4.20.

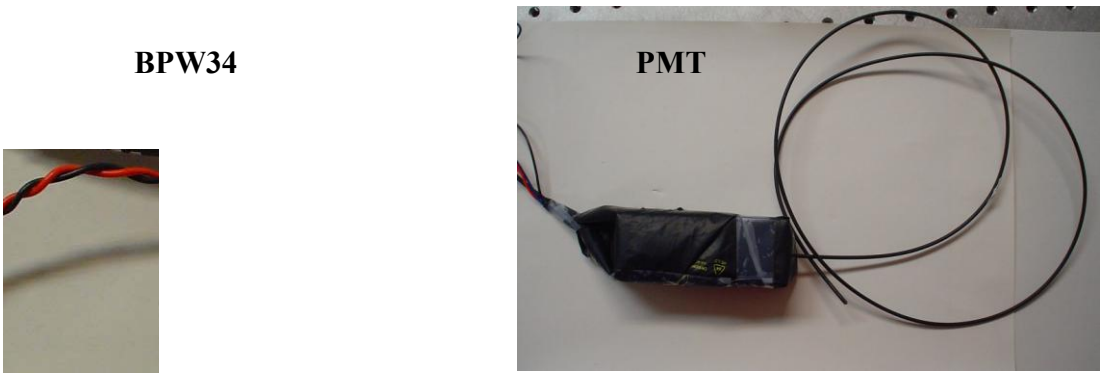

Figure 4.19 (a) fiber coupled BPW34 (b) fiber coupled PMT

As a further precautionary measure for the collimated optical transmission scheme, the water tank has been blackened on all sides, including top and bottom, to remove any external light entering the tank, see Figure 4.4. A pinhole aperture with a diameter of 6 mm was placed at the front and back of the tank. Two 1 mm apertures have been used to avoid forward scattered light entering the fiber coupled detectors (see Section 4.4.2).

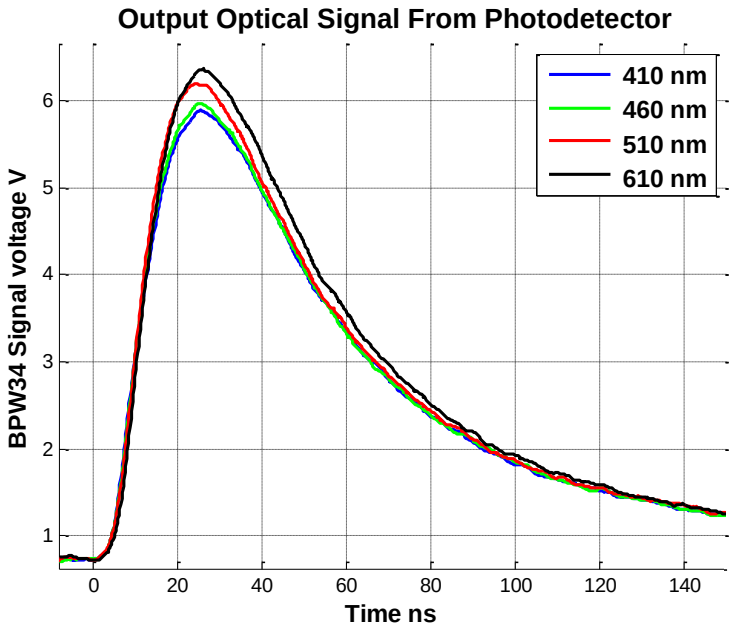

Figure 4.20 Output signals from tissue phantom acquired from PMT optical photodetector.

4.5.4. Spectroscopic Optoacoustic Measurement Scheme.

The main differences in the spectroscopic optoacoustic detection schemes is again based on the detection, in both cases the acoustic transducer used is an immersion resonant acoustic transducer with a central frequency located at 10 MHz (V327 Panametrics). However, in the first scheme, used to determine the spectroscopic profile of a SGNP solution, the acoustic transducer is connected to a 40 dB amplifier (see Figure 4.21). In the second case, the acoustic detector is connected directly to the oscilloscope (see Figure 4.22). This modification has been introduced as the GNR solution has a higher absorption coefficient when compared to the SGNP solution thus producing higher pressure transients. The first peak to peak voltage of the acoustic transient is measured at each wavelength emitted by the optical source and stored in the computer. A series of optoacoustic signals from the spherical particles are presented in Figure 4.23 and for the nanorod particles in Figure 4.24.

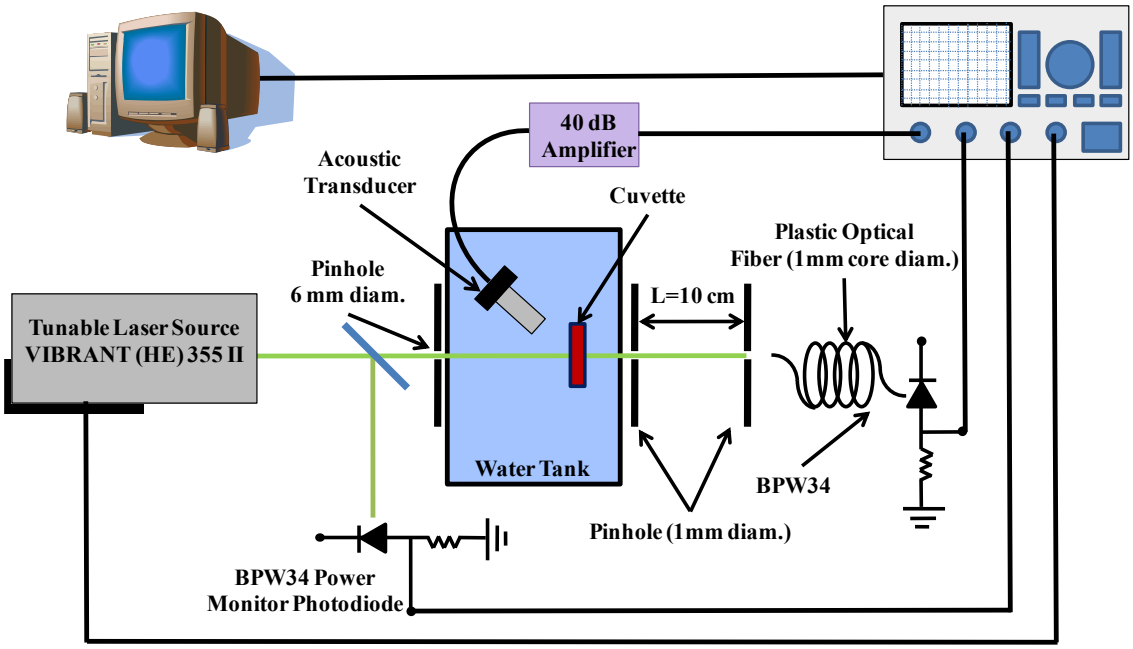

Figure 4.21 Parallel measurement scheme for LOS measurements of SGNP solution

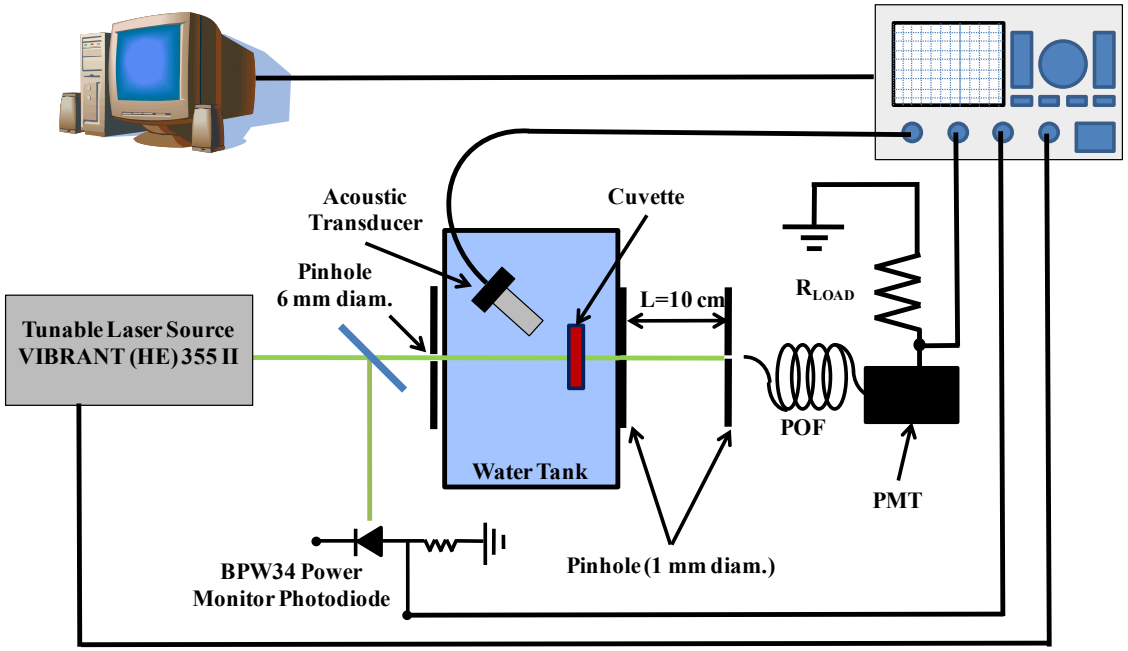

Figure 4.22 Parallel measurement scheme for LOS measurements of GNR solution

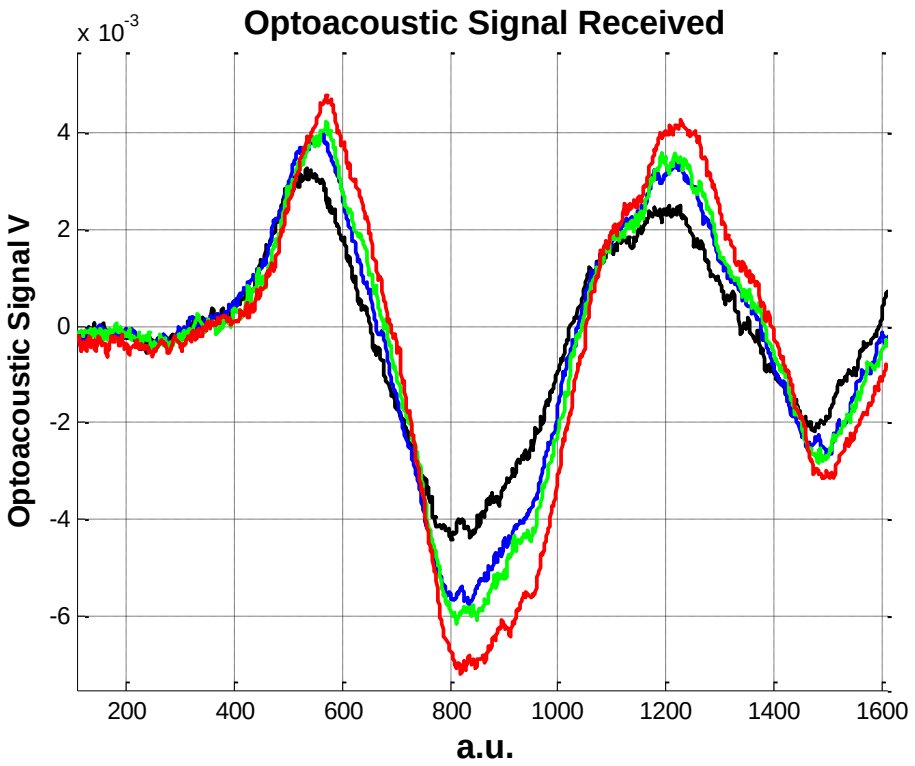

Figure 4.23 Optoacoustic signals obtained from spherical gold nanoparticle solution for a series of different wavelengths.

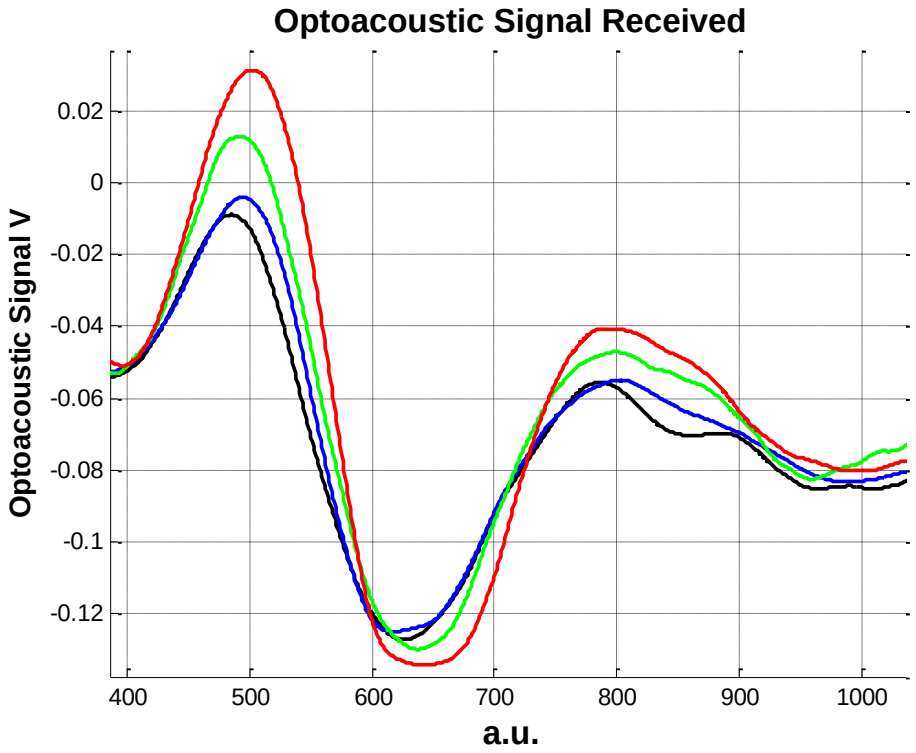

Figure 4.24 Optoacoustic signals obtained from gold nanorod solution for a series of different wavelengths.

4.5.5. Spectroscopic Characterization Measurement Protocol.

As previously mentioned, the objective of the spectroscopic measurements has been to measure the profile of two different gold colloid solutions. The first solution is based on a SGNP solution and the second on a GNR solution embedded in the optical liquid tissue phantom. As a result two different measurement protocols have been defined, one for each nanostructure.

4.5.5.1. Spectroscopic Measurement Protocol for SGNP solution

The spectroscopic measurement has been performed over the wavelength range from 450 nm to 650 nm in steps of 5 nm. This wavelength range has been identified by Mie Theory for spherical homogenous particles presented in Chapter 3. The absorption peak due to the SPR is expected close to 520 nm.

The first step taken for this measurement has been a baseline measurement which is taken for the cuvette filled with distilled water. This measurement is required for the optical transmission scheme to obtain the spectral profile. To obtain the absorption coefficient the optical power received when the cuvette contains the sample at each

wavelength, $P_{sample}(\lambda)$, is compared to the power from the zero measure, $P_{zero}(\lambda)$ (see Figure 4.25), where solving for the absorption coefficient in Beers law (Chapter 2 section 2.2) gives:

$$\mu_{abs}(\lambda) = -\frac{1}{d_{cuvette}} \ln\left(\frac{P_{sample}(\lambda)}{P_{zero}(\lambda)}\right) \tag{4.5.2}$$

The requirement for this zero measurement highlights another advantage of the optoacoustic technique. The acoustic signals generated are directly proportional to the absorbed laser energy, thus no reference is required. The data acquired from both the monitor and output BPW34 pin photodiodes are stored and used for direct conversion to obtain the spectroscopic profile.

The next step involves filling the 1 mm cuvette with the 15 ± 2 nm diameter SGNP solution and performing the measurement over the same spectral range. The power incident on the cuvette filled sample is calculated using the monitor photodiode for each wavelength.

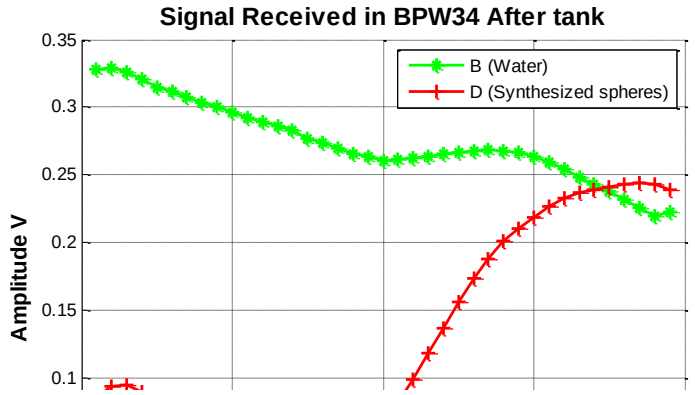

Figure 4.25 Collimated optical transmission measurements (green) water tank with no nanoparticle absorber, baseline measurement and (red) water tank with nanoparticles.

For the optoacoustic spectral profile the signal obtained from the acoustic transducer is acquired and stored for each wavelength. Using the information from the BPW34 monitor photodiode the power reaching the sample filled cuvette is adjusted and stored.

A real time comparative analysis is carried out by plotting the results at each wavelength step for each characterization method.

4.5.5.2. Spectroscopic Measurement Protocol for GNR Solution Embedded in a Liquid Tissue Phantom

From the theoretical review of the spectroscopic properties of GNR solutions it has been observed that the longitudinal surface plasmon (LSP) peak can be tuned to the visible - NIR portion of the electromagnetic spectrum. To account for this, the experimental scheme has been modified to cover the spectroscopic wavelength range from 410 nm to 1000 nm. Within this wavelength range the profile of both the LSP and transverse surface plasmon (TSP) can be observed. The GNR solution examined using this protocol have an aspect ratio of 3.5, the length of the rod is 35 nm and the width 10 nm. The theoretical analysis presented in Chapter 3 has shown that absorption is dominant in this GNR solution

Several modifications have been carried out on the experimental spectroscopic scheme, these have been based on errors observed from the preliminary SGNP measurements. The optical output power of the laser has been stabilized by letting it warm up for a longer period of time and by monitoring its output using the BPW34. Also the signals captured from both the optical and acoustic transducers have been averaged over 8 consecutive pulses.

As in the previous case for the SGNP solution, the first step taken has been a baseline measurement for the cuvette filled with a distilled water solution which is required by the optical transmission scheme. The data acquired from the monitor BPW34 photodiode and the PMT have been stored in the PC. The next step has involved filling the cuvette with the GNR solution and performing the measurement over the same preset wavelength range from 410 nm to 1000 nm.

The optical power incident on the cuvette is required to calculate the absorption coefficient of the GNR solution, thus it is necessary to know the attenuation due to the scattering of the surrounding medium. This has been obtained experimentally by filling a 1 cm optical path quartz cuvette with a sample of the scattering medium and using a commercial spectrophotometer (Lambda14 Perkin Elmer Inc.) over the complete wavelength range. The results for 5 different concentrations are presented in the

following Figure 4.26. These results have been included in the software of the optoacoustic spectroscopic system to calculate the power incident on the cuvette containing the absorbing GNR solution.

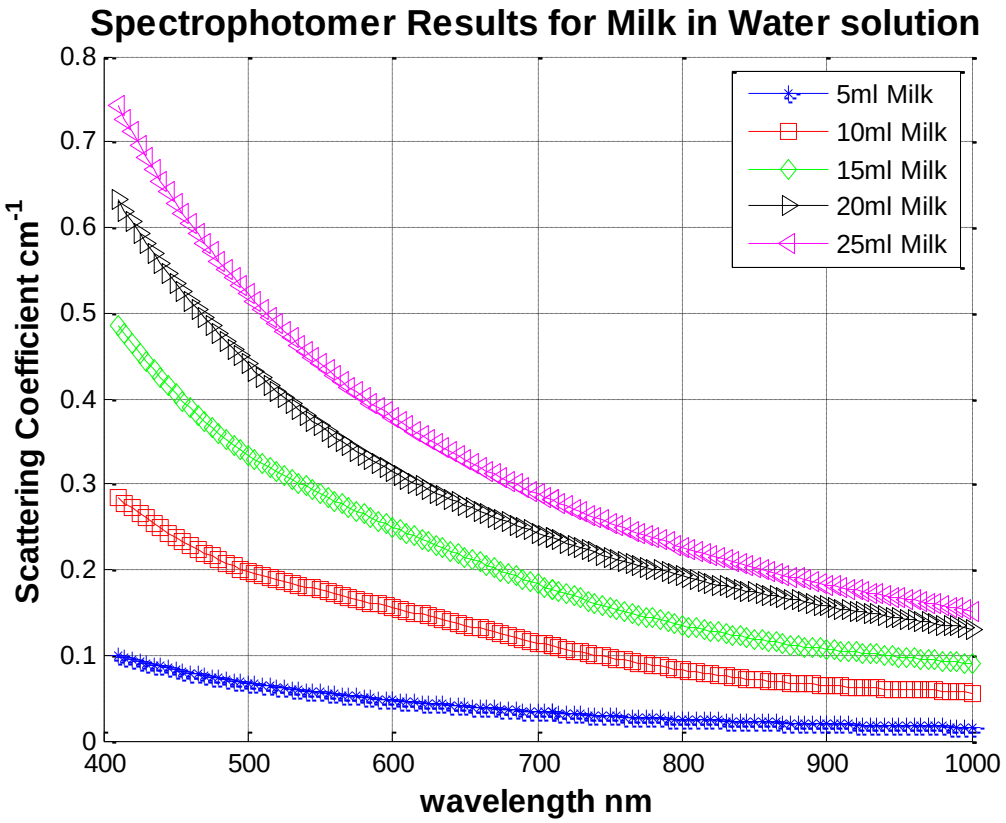

Figure 4.26 Scattering coefficient as a function of wavelength for 5 different milk volumes in the tank containing 7.5 liters of water.

To obtain the optoacoustic spectral profile the signal obtained from the acoustic transducer is acquired and stored for each wavelength. Using the information acquired from the BPW34 monitor photodiode and the previously characterized scattering coefficient the power reaching the sample filled cuvette is adjusted and stored. A real time comparative analysis is carried out by plotting the results at each wavelength step for both characterization schemes.

4.6. Conclusions

This chapter has brought together the key concepts of optical propagation and optoacoustic signal generation discussed in Chapter 2, along with the unique absorption properties of colloidal gold solutions presented in Chapter 3, to design and implement two optoacoustic characterization schemes for the quantification and spectral resolution of gold nanoparticles embedded in a scattering medium.

A review of the measurement concepts regarding the optoacoustic technique which have been employed in this research work have been presented. This has been followed by details regarding the high scattering liquid tissue phantom, which mimics the optical properties of human soft tissue. Due to the composition of milk, based on large particles of fat and proteins, this solution has been identified as a suitable agent to design a high scattering phantom medium for the experimental trials presented in this thesis.

The design and implementation protocol of two different optoacoustic measurement procedures, where both incorporate a reference measurement scheme in parallel have been presented in this chapter. The first scheme, based on a single laser wavelength of 532 nm, has been specifically designed to measure the concentration of a highly absorbing synthesized 15 ± 2 nm diameter SGNP solution embedded in a highly scattering medium.

The second system, has been designed to measure the spectroscopic signature of two different absorbing gold nanostructure solutions using the optoacoustics technique and reference measurement. The wavelength range of interest for both nanostructures has been identified in Chapter 3 and is 450 nm to 650 nm for the SGNP, and, from 410 nm to 1000 nm for the GNR solution.

Chapter 5.

Experimental Results on the Optical Properties of Spherical Gold Nanoparticles at a Single Wavelength in a High Scattering Media.

5.1. Introduction

Throughout this thesis the benefits of quantitative online *in-vivo* technique to quantify the absorption coefficient of optical contrast agents within a highly scattering media, such as soft tissue, has been indicated. In this chapter results from the optoacoustic experimental scheme, specifically designed to quantify the absorption of a spherical gold nanoparticle (SGNP) solution embedded in a high scattering medium will be presented. The experimental scheme, described in the previous chapter, has been designed based on the concepts of optical propagation and optoacoustic signal generation presented in Chapter 2. The experimental parameters have been defined from a theoretical analysis using Mie theory presented in Chapter 3.

The experimental results presented here have been divided into three different sections. The first set of results are from preliminary trials on a known pure absorber (i.e. $\mu_{abs} \gg \mu_{sca}$) embedded in a distilled water solution. From a comparative analysis between the optoacoustic and reference measurement scheme, agreement is shown, thus ensuring the feasibility of the technique for quantification purposes. This experimental analysis has motivated further trials using highly absorbing SGNP solutions.

The second set of experimental results is based on the measurement, using the parallel scheme, of different concentrations of a SGNP solution which has been specifically synthesized to be highly absorbing. The peak absorption band is located close to the wavelength emission of the laser source. The SGNP solution quantified in these experimental trials has again been embedded in a distilled water solution.

Finally, and in accordance with the objectives laid out for this experimental scheme, the third section contains experimental results from a specifically designed SGNP solution embedded in a high scattering medium. This final analysis will highlight one of the major advantages of using the optoacoustic technique which is the localization of absorbing media using a time of flight (TOF) analysis, a principle that is used in optoacoustic imaging. Using this information, a comparative analysis of the results from both measurement schemes are again shown to be in close agreement, demonstrating the scope of optoacoustics for quantification of absorbers in high scattering media.

5.2. Absorption Measurement Analysis

The objective of the experimental analysis presented in this chapter has been to quantify the attenuation coefficient of pure absorbers, and to confirm the feasibility of the optoacoustic technique as a reliable measurement method. Preliminary trials have been carried out on a known pure optical absorber, which is based on different concentrations of ink.

The reference collimated optical scheme places the upper limit on the sensitivity of the system. This is because the analysis is based on the measurement of the small portion light emerging from the attenuating media. The optoacoustic analysis is based on the large portion of light that is attenuated by the absorber.

To PMT optical detector has been implemented to maximize the sensitivity of the optical transmission scheme. The minimum optical power detectable by this device is $P_{\min} = 0.5\,\text{pW}$. To measure high concentrations a quartz cuvette with an optical path $d = 1\,\text{mm}$ has been used. A description of the reference scheme is presented in Figure 5.1.

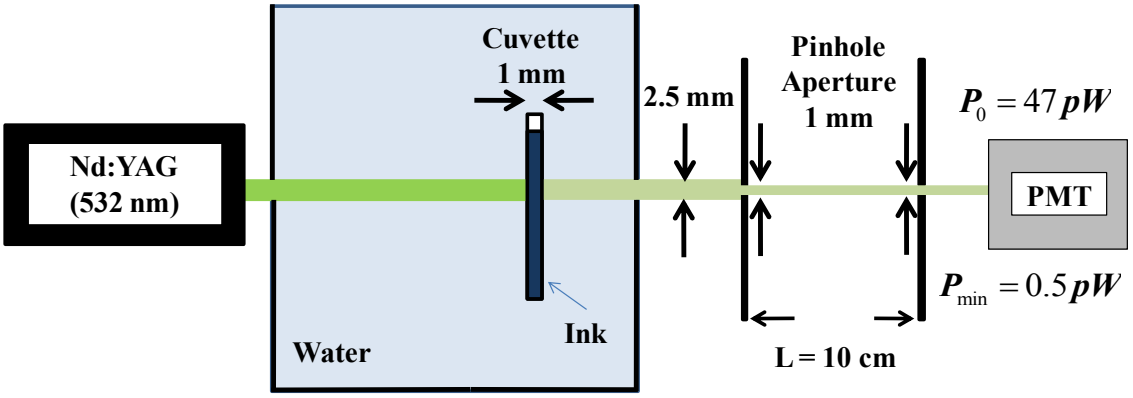

Figure 5.1 Collimated optical transmission measurement scheme

From preliminary characterisation of the ink solution using a commercial spectrophotometer it has been seen that the absorption coefficient at the operational wavelength of the laser source (532 nm) is 0.36 cm^{-1} for a 0.1 % ink solution (see Figure 5.2). The initial optical power reaching the detector, through the tank and pinholes, when the cuvette is filled with distilled water is $P_0 = 47\,\text{pW}$. From Beers law,

$$\mu_{abs} = \frac{-1}{d} \ln\left(\frac{P_{\min}}{P_0}\right) \qquad (5.2.1),$$

it is calculated that the maximum ink absorption coefficient measurable is 45.3 cm^{-1}. Considering the data from the spectrophotometer, and, the dimensions of the cuvette, the maximum ink concentration is 12.62 %.

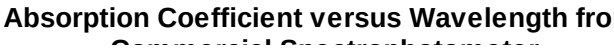

Figure 5.2 Spectroscopic response from a 0.1 % ink solution obtained from a commercial spectrophotometer.

5.3. Experimental Results for the Quantification of a Known Pure Absorber.

The ink absorber used in the experimental trials has been based on different concentrations of Montblanc, Midnight Blue (105194). Other authors have taken advantage of the absorption properties of ink solutions to generate optoacoustic signals [5.1-5.5]. A comparative analysis of the results obtained using the reference measurement scheme will be presented.

5.3.1. Reference measurement results and Quantification using collimated optical transmission.

The analysis of the ink absorption coefficient has been carried out over the complete measurement range of the PMT optical detector (i.e. from 47 pW to 0.5 pW). To ensure these power levels 15 different ink concentrations within the previously identified range from 0 % to 12.6 % have been prepared. The diluent in each case has been distilled water. In Figure 5.3 the average optical power received, detected using the highly sensitive PMT versus different the ink concentrations in a 1 mm cuvette is presented. To ensure that the minimum power has been received an additional measurement for a 20 % ink solution concentration has been performed.

The results for the optical attenuation present a clear exponential decay for increasing ink solution concentrations. This process of optical attenuation in a homogeneous absorbing medium, where $\mu_{abs} \gg \mu_{sca}$, has been described by Beer's law,

$$P_{ink} = P_0 \exp\left(-\mu_{abs} d\right) \tag{5.3.1}$$

Where P_{ink} (W) is the power received for each ink concentration over the optical path distance $d = 1\,\text{mm}$. The initial power incident on the cuvette containing the sample is taken to be $P_0 = 47\,\text{pW}$. The exponential decay of the optical intensity is governed by the linear dimensions of the absorbing medium, defined by the constant optical path distance of the cuvette ($d = 1\,\text{mm}$) and the absorption coefficient μ_{abs}.

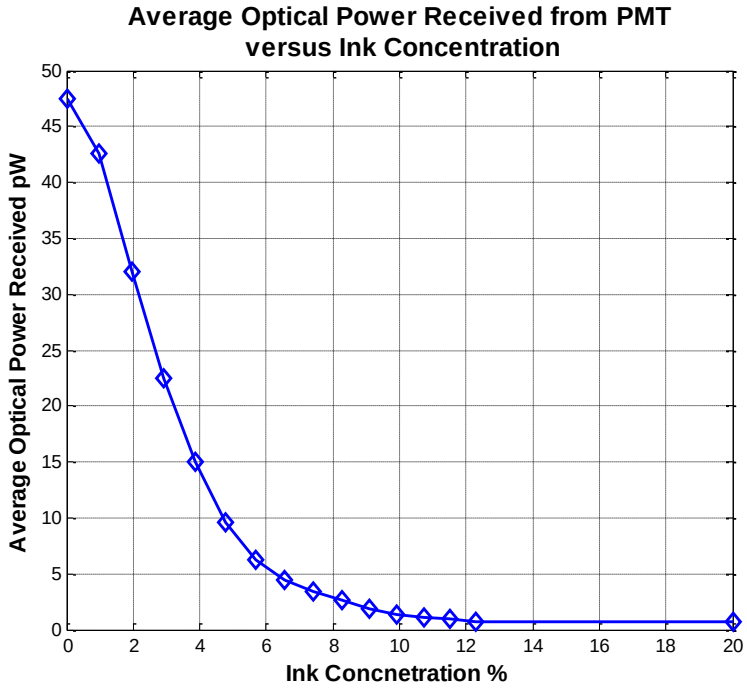

Figure 5.3 Average optical power received versus ink concentration.

To relate the absorption coefficient to the ink concentration, equation (5.2.1) is used to calculate the absorption coefficient for each ink concentration using the optical power received in each case from the data presented in Figure 5.3. The relation between both of these terms is presented in the following Figure 5.4.

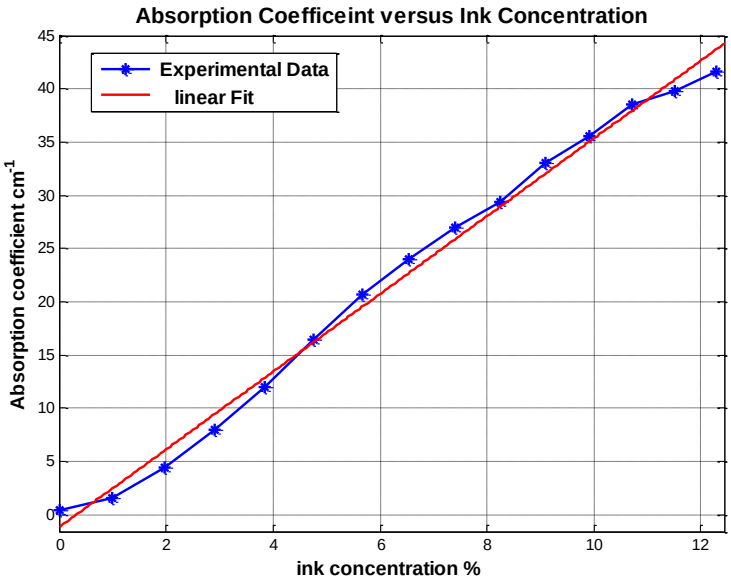

Figure 5.4 Graphical representation of the dependence of the absorption coefficient, μ_{abs}, at 532 nm versus the ink concentration, where μ_{abs} = 3.65 ± 0.2 cm^{-1} (per % ink concentration).

The linear response of the absorption coefficient and ink concentration may be observed, where this is in agreement with predictions of Beer's law for a pure absorber. By taking a linear fit of the experimental points, the dependence of the absorption coefficient on the absorber concentration is obtained, in this case it is 3.65 ± 0.2 cm^{-1} (per % ink concentration).

The results obtained at 532 nm are in good agreement with those obtained from the analysis using the spectrophotometer, see Figure 5.2, at the same wavelength. Also in [5.1] the authors have quoted a value of 3.3 cm^{-1} for a similar ink solution. The results obtained and presented here using the reference scheme will now be compared to those obtained from the optoacoustic characterization scheme.

5.3.2. Measurement Results and Quantification using the Optoacoustic Technique.

In this section details regarding the quantitative analysis of the ink absorber embedded in a transparent medium using the optoacoustic technique are presented. In Chapter 2 of this thesis a theoretical review of the optical to acoustic energy conversion has been presented (Chapter 2 Section 2.3,), where it has been shown that under stress and thermal confinement the acoustic pressure generated is proportional to the optical absorption coefficient of the irradiated absorber. Revisiting the expression from equation 2.3.15, this pressure, *p*, is given by [5.6]:

$$p(d,\lambda) = \Gamma \mu_{abs}(\lambda) F_0 \exp\left(-\mu_{abs}(\lambda) d\right) \tag{5.3.2}$$

the effective attenuation coefficient, μ_{eff}, has been replaced by the absorption coefficient, μ_{abs}, as the scattering component of the absorber solution may be neglected (i.e. $\mu_{abs} \gg \mu_{sca}$). The concentration of the ink solution has ranged from 0% (i.e. distilled water) to 12.6 %. For each concentration measurement the amplitude of the first resonant peak from the acoustic transducer is recorded. In Figure 5.5 the results for the optoacoustic signal generated from the laser material interaction versus the concentration of the absorbing ink medium are presented. The relation between the optoacoustic signal produced and the sample concentration is in agreement with work performed by other authors on ink solutions [5.7].

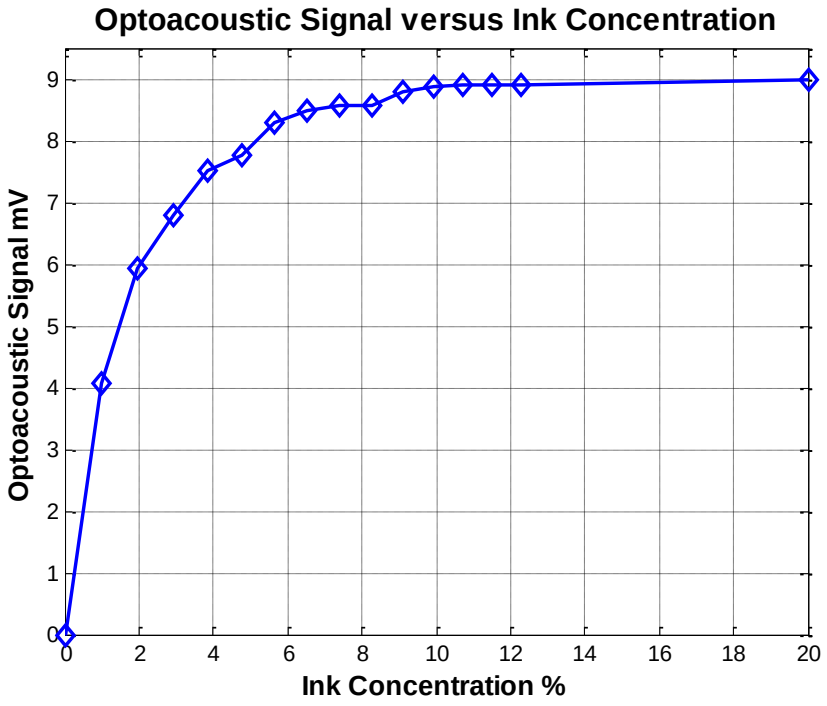

Figure 5.5 Graphical representation of the of the peak to peak optoacoustic signal generated from the initial pressure distribution of the laser absorber interaction for concentrations ranging from 0 % to 20 %.

From equation (5.3.2) it can easily be seen that as the absorbed laser fluence increases, so too will the pressure induced. According to Beer's Law and the exponential nature of the absorption of the laser radiation, the energy density transmitted, E_{TX}, decays exponentially with increasing concentration, i.e.:

$$E_{TX} = E_0 \exp\left(-\mu_{abs} d\right) \tag{5.3.3}$$

From here it may be deduced that the energy density absorbed, E_{abs}, is:

$$E_{abs} = E_0 - E_{TX} \tag{5.3.4}$$

In equation (5.3.4) it is shown that the energy density absorbed is at a maximum, $E_{abs-\max}$ when $E_{TX} = 0$ thus the maximum pressure induced, $p_{0-\max}$, in terms of the maximum energy density absorbed is thus:

$$p_{0-\max} = \Gamma E_{abs-\max} = \Gamma E_0 \tag{5.3.5}$$

Using (5.3.5) and (5.3.3) the pressure generated in function of the concentration may be expressed as:

$$p = p_{0-\max}\left(1-\exp\left(-\mu_{abs}d\right)\right) \tag{5.3.6}$$

Where this particular relation is shown in Figure 5.5 for the optoacoustic pressure generated versus the concentration of the absorbing ink solution. Solving for the absorption coefficient (at the laser wavelength of 532 nm) in terms of the induced optoacoustic signal we obtain:

$$\mu_{abs} = \frac{-1}{d}\ln\left(1-\frac{p}{p_{0-\max}}\right) \tag{5.3.7}$$

Since the optoacoustic signal amplitude is directly proportional to the voltage amplitude produced by the transducer, then:

$$\mu_{abs} = \frac{-1}{d}\ln\left(1-\frac{v_{out}}{v_{0-\max}}\right) \tag{5.3.8}$$

By introducing the experimental data in Figure 5.5 into equation (5.3.8), a plot of the absorption coefficient versus the concentration of the absorbing ink solution can be generated, where this is presented in Figure 5.6. The results obtained demonstrate a linear response. Taking the slope from a linear fit of the data indicates the absorption coefficient cm^{-1} per % ink concentration where this value is calculated to be μ_{abs} = 3.67 ± 0.3 cm^{-1} (per % ink concentration). A similar linear response from data obtained from different concentrations of an ink solution has been presented in [5.7].

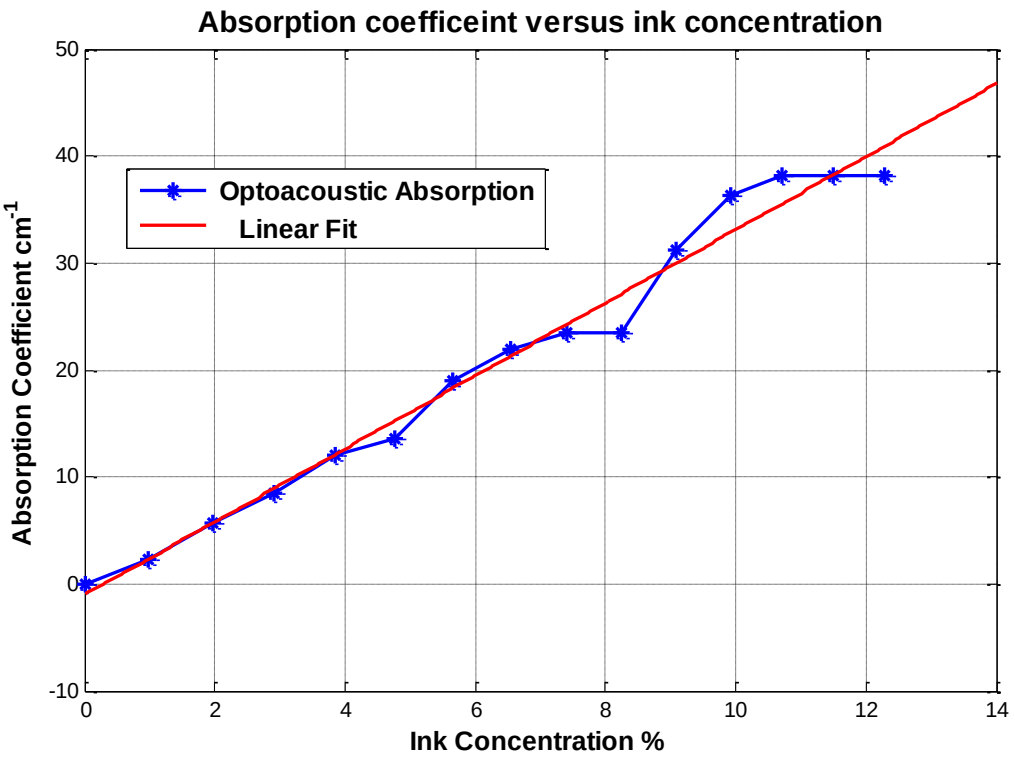

Figure 5.6 Graphical representation of the absorption coefficient versus the concentration of the absorbing ink solution concentration, where μ_{abs} is calculated to be 3.67 ± 0.3 cm^{-1} (per % ink concentration).

5.3.3. Comparative Analysis of Results.

The two previous sections have presented the results on a quantitative analysis of an ink absorber embedded in an optically transparent medium using the optoacoustic technique and reference collimated optical transmission scheme in parallel. Use has been made of Beer's law for a pure absorber to determine the absorption coefficient in function of the absorbers concentration. The absorption coefficient obtained experimentally using the optoacoustic technique was measured to be 3.67 ± 0.3 cm^{-1} (per % ink concentration) and using the collimated optical transmission, 3.65 ± 0.2 cm^{-1} (per % ink concentration), showing good agreement between both measurement schemes. The results are also in very close agreement with the results obtained from a commercial spectrophotometer (see Figure 5.2), and those from other authors [5.1]. This preliminary trial using ink has demonstrated the feasibility of the optoacoustic technique and has motivated further experimental work on quantifying the optical properties of SGNP solutions.

5.4. Experimental Results for the quantification of a SGNP Solution.

The previous sections of this chapter have dealt with quantifying the absorption coefficient of an ink absorber. In this section, the same parallel experimental setup has been used to determine the optical properties of an absorbing colloidal gold solution. Different concentrations of a spherical gold nanoparticle solution (SGNP) have been specifically synthesized using the Turkevich protocol [5.8] to perform this analysis, more details regarding the synthesis procedure may be found in Appendix D. The diameter of the particles has been confirmed using Transmission Electron Microscopy (TEM) to be 20 ± 2 nm. Using the theoretical analysis based on Rayleigh and Mie theory, developed in Chapter 3 (Section 3.4), it has been demonstrated that the scattering component from a 20 nm diameter particle solution does not add significantly to the total extinction coefficient. The behaviour of the particles using Mie Theory over the wavelength range from 300 nm to 700 nm is presented in Figure 5.7 for the extinction, absorption and scattering coefficients. From this numerical analysis it can be seen that the peak absorption band lies close to the wavelength of the optical source (532 nm) and that optical absorption is the dominant process.

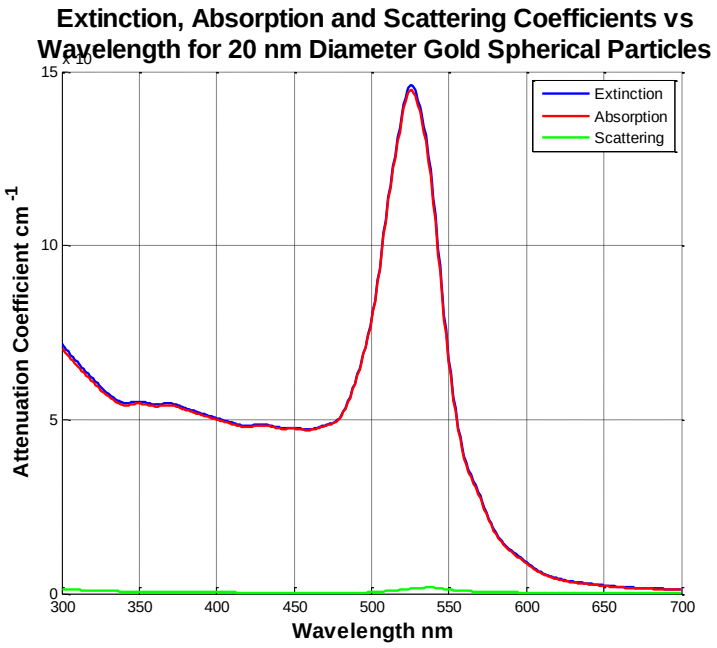

Figure 5.7 Plot of extinction, absorption and scattering coefficient as calculated from Mie theory, (Chapter 3 Section 3.4) the ratio between the scattering coefficient and the absorption coefficient is 0.01.

This behaviour is in agreement with theoretical work using Mie theory performed by other authors in [5.9], where it has been reported that the ratio of the scattering to absorption presented by a 20 nm SGNP is:

$$\frac{\mu_{sca}}{\mu_{abs}} = 0.01 \tag{5.4.1}$$

5.4.1. Reference Collimated Optical Transmission Measurement Results and Analysis.

The experimental procedure described in Chapter 4 and used in the previous section of this chapter to quantify the absorption coefficient of an ink absorber solution has been employed again using 13 different concentrations of the gold nanosphere solution. In Figure 5.8 a plot of the power received by the PMT after the laser radiation has traversed the different concentrations of the SGNP solution is presented. The concentration of the nanoparticle solution in this case has been normalized to the most concentrated solution. The exponential behavior (as presented in Figure 5.3 for ink) is not as evident, this is due to the limited SGNP solution concentrations available.

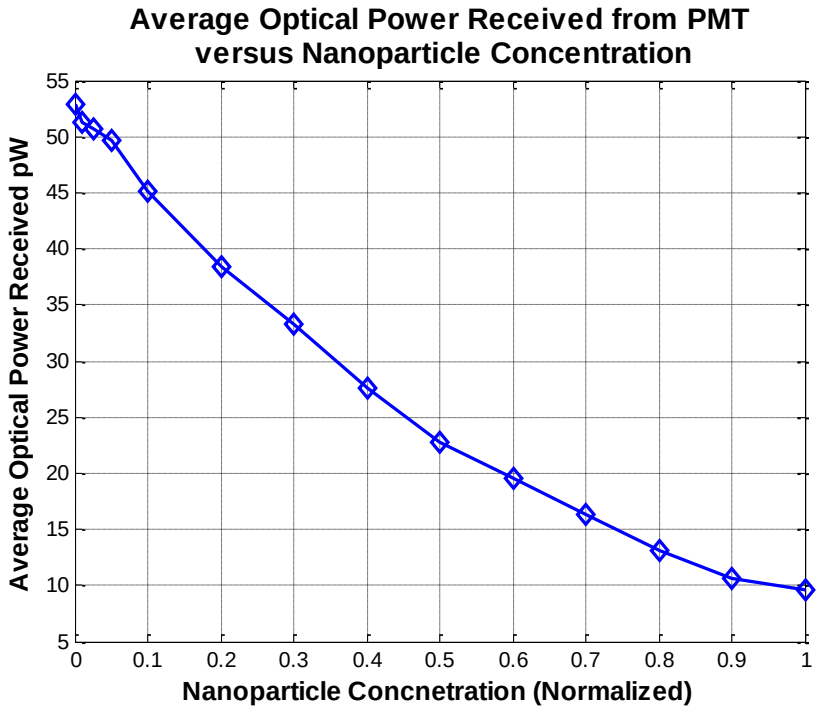

Figure 5.8 Optical power received versus 20 nm gold nanoparticle concentration, where the highest concentration of the nanoparticle solution has been normalized.

Considering again Beer's law (equation (5.3.1)) and solving for the absorption coefficient for each SGNP concentration, the relation between the absorption coefficient, μ_{abs}, and the SGNP solution concentration is obtained. The results of this analysis are presented in Figure 5.9. From the linear response of the system it may be observed that Beer's law is again satisfied. The calculated absorption coefficient of the SGNP solution is 17.35 ± 0.5 cm^{-1} (per normalized SGNP concentration).

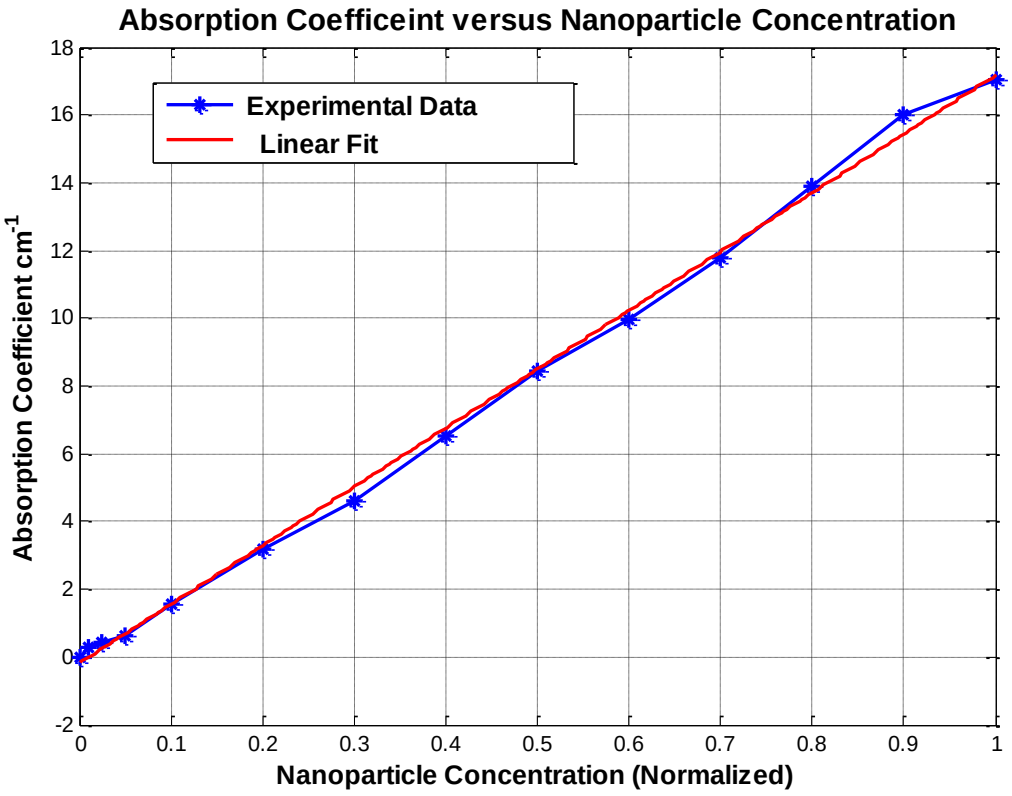

Figure 5.9 Absorption coefficient at the laser wavelength of 532 nm versus the concentration (normalized) of the SGNP solution. The absorption μ_{abs} is calculated from the slope to be 17.35 ± 0.5 cm^{-1} (per normalized SGNP concentration).

5.4.2. Measurement Results and Quantification using Optoacoustic Technique on SGNP solution.

The procedure used to quantify the absorption coefficient of the ink solution using optoacoustics has again been used to determine the optical properties of the SGNP solution. The optoacoustic signal obtained from the amplified resonant transducer are presented in Figure 5.10 for each concentration of the SGNP solution.

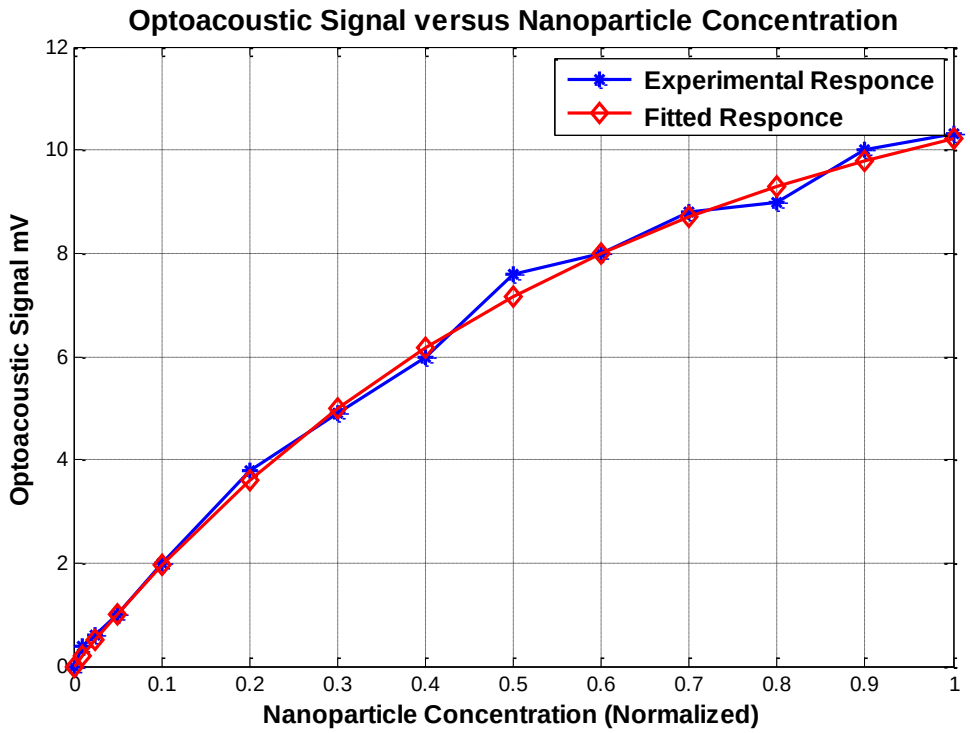

Figure 5.10 Optoacoustic signal response versus SGNP concentration for 20 nm diameter particles along with exponential fit to the data.

The same tendency observed for the absorbing ink solution is also seen here for the SGNP solution (see Figure 5.5). However, unlike the ink solution the maximum optoacoustic signal has not been obtained, this due to the limited range in concentration of the SGNP solution. The maximum signal amplitude is required to obtain the maximum pressure generated (see equation (5.3.8)). This shortcoming has been overcome by fitting the experimental data to an exponential curve, using this procedure the maximum optoacoustic signal has been determined in this case to be 12.5 mV. Using equation (5.3.8) and the experimental data along with the maximum signal response from the exponential fit allows the absorption coefficient versus SGNP concentration to be plotted, see Figure 5.11. The results obtained demonstrate a linear response, again by taking the slope from a linear fit of the data the absorption coefficient per SGNP concentration is calculated to be 17.18 ± 0.8 cm^{-1} (per normalized SGNP concentration).

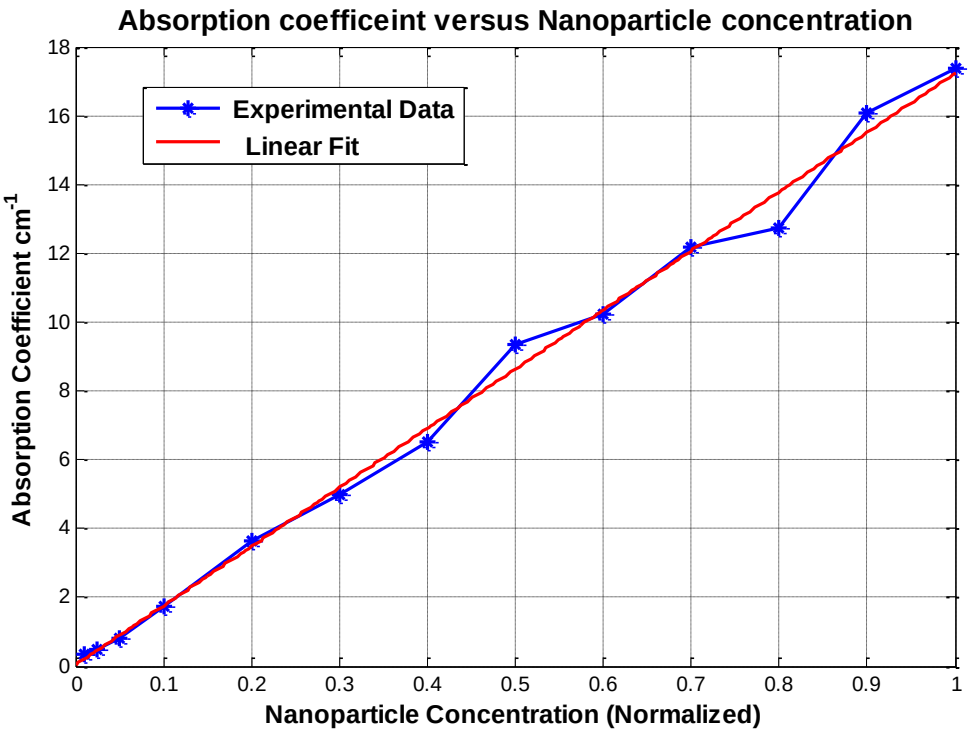

Figure 5.11The absorption coefficient of the 20 nm diameter SGNP versus nanoparticle solution concentration, the calculated absorption coefficient is 17.18 ± 0.8 cm^{-1} (per nanoparticle concentration)

5.4.3. Comparative Analysis of Results

The two previous sections have presented the results obtained from different concentrations of an absorbing 20 nm diameter SGNP solution using both the optoacoustic technique and a collimated optical transmission reference scheme in parallel. As in previous sections, use has been made of Beer's law for a pure absorber to quantify the absorption coefficient of the SGNP solution. It has been observed that the results for this coefficient using both techniques are in good agreement, where the values obtained were 17.35 ± 0.5 cm^{-1} (per normalized SGNP concentration) and 17.18 ± 0.8 cm^{-1} (per normalized SGNP concentration) using collimated optical transmission and the optoacoustic technique, respectively.

5.5. Experimental Results for the Quantification of a SGNP Solution Embedded in a Highly Scattering Medium.

The experimental trials presented in this section address the requirement for optical parameter quantification of absorbers located within a highly scattering medium. The scattering medium and measurement scheme used for this procedure have been discussed in Chapter 4 Section 4.3. Here, this experimental scheme will be used to determine the absorption coefficient for a specifically synthesized SGNP solution with sphere diameter of 15 ± 2nm, confirmed using TEM.

Use has been made of Beer's law to determine the attenuation of light as it travels through the attenuating medium. However, since the 1 mm cuvette containing the absorbing solution is located within an optical attenuating medium, dominated by scattering, the optical properties of this medium must also be taken into consideration, this has been done using the following expression [5.10]:

$$P(d_{tot}) = P_0 \exp(-\mu_{abs} d_{abs} - \mu_{sca} d_{sca}) \tag{5.5.1}$$

Where μ_{sca} and d_{sca} are the scattering coefficient of the surrounding medium and the linear optical path distance in this medium, respectively. The absorption coefficient is represented by μ_{abs} and has a linear optical path distance of d_{abs}. The medium attenuation described by equation (5.5.1) assumes that the scattering is isotropic, in Chapter 2 Section 2.2.2 a review of the anisotropic nature of electromagnetic waves and their directionally dependence in scattering media, such as soft tissue, has been presented, where the reduced scattering coefficient has been defined in terms of the anisotropy parameter g as $\mu'_{sca} = (1-g)\mu_{sca}$ [5.11].

5.5.1. Time of Flight Analysis

From equation (5.5.1) it may be observed that knowledge of the dimensions of both the scattering and absorption medium are required to quantify each parameter. These have been obtained using a Time of Flight (TOF) analysis of the optoacoustic transients generated from the light/SGNP interaction [12-13]. This particular analysis highlights one of the major advantages of the optoacoustic technique when compared to standard spectroscopic or transmission measurement schemes where no positional or dimensional

data can be retrieved. This feature is the basis for optoacoustic imaging techniques [5.14-5.15].

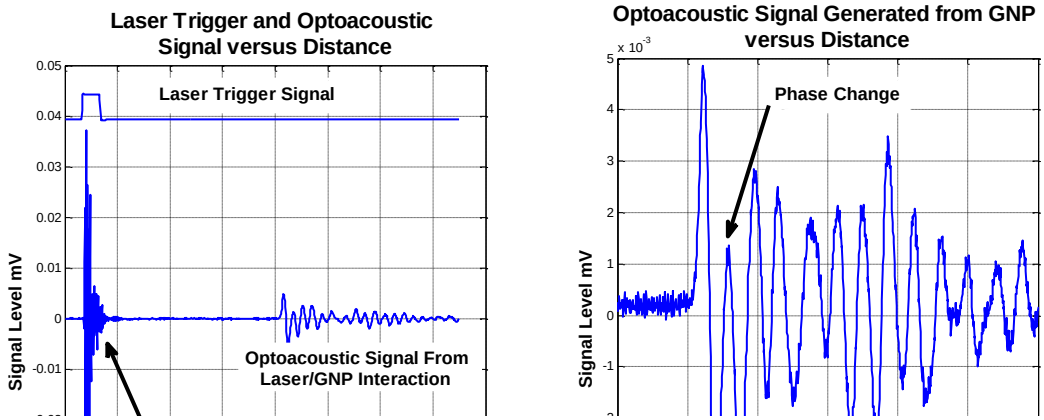

Figure 5.12 (Left) Optoacoustic response along with laser trigger signal showing TOF of 42 mm. (Right) Optoacoustic signal from laser/SGNP interaction with phase changes every 2 mm which correspond to the cuvette roundtrip distance.

In Figure 5.12 (Left) the optoacoustic signals generated by the thermoelastic expansion of the SGNP particles may be observed along with the trigger signal from the laser source. The first set of peaks, labelled *Laser/Acoustic Detector Interaction*, correspond to the optoacoustic response from the direct impact of the 532 nm laser radiation on the acoustic transducer and also electrical noise. The second set of peaks corresponds to the optoacoustic signals generated from the laser/SGNP interaction. Using the TOF analysis and taking the calibrated speed of sound in the diluted milk solution, measured to be 1496 m/s, it is possible to determine the position of the cuvette containing the SGNPs within the scattering medium. This distance was measured and verified to be 42 mm.

In Figure 5.12 (right) a close-up of the optoacoustic signal generated by the laser/SGNP interaction is presented. It may be observed that this signal contains a change in phase which occur periodically, this is due to the internally reflected acoustic signals within the cuvette containing the sample that are retransmitted in the direction of the acoustic transducer. This phase change occurs at a distance of 2 mm which corresponds to the round trip distance within the cuvette. From the temporal analysis of the optoacoustic

signals the location and dimensions of the absorbing object within the scattering medium have been determined. The information obtained from the TOF analysis provides the distance parameters required in equation (5.5.1), i.e. $d_{sca} = 42\,\text{mm}$ and $d_{abs} = 1\,\text{mm}$.

5.5.2. Reference Collimated Optical Transmission Measurement Results and Quantification.

The optical power reaching the PMT detector for different concentrations of the SGNP solution within different concentrations of the diluted milk solution is presented in Figure 5.13. The exponential behaviour predicted by Beer's law is again observed. Also, and as expected, the concentration of both the scattering agent in the liquid phantom and SGNP increase, the optical power reaching the detector is seen to decrease.

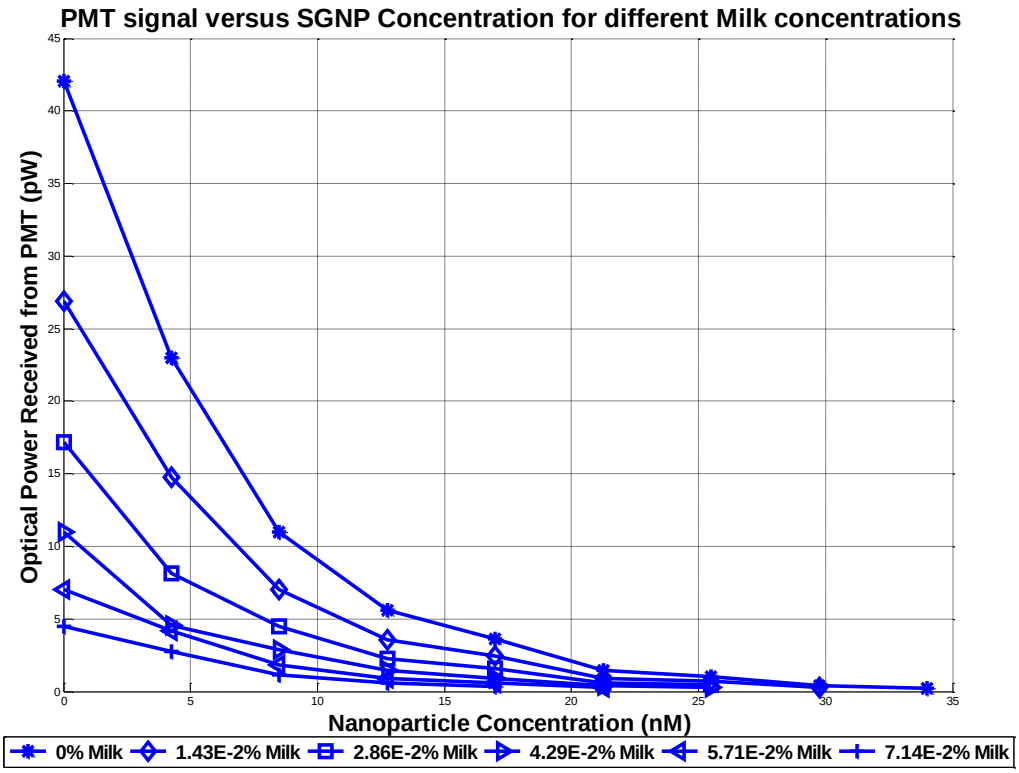

Figure 5.13 Optical power reaching the PMT detector for different concentrations of SGNP solutions within concentrations of diluted milk ranging between 0 % to 7.14 10^{-2} %.

To obtain the absorption coefficient of the embedded SGNP solution equation (5.5.1) is solved for this coefficient as:

$$\mu_{abs} = \frac{-1}{d_{abs}}\left(\ln\left(\frac{P(d_{tot})}{P_0}\right) + \mu_{sca}d_{sca}\right) \tag{5.5.2}$$

Both d_{abs} and d_{sca} have been obtained from the TOF analysis, however knowledge of the scattering coefficient is required to obtain the absorption coefficient.

The scattering coefficient is obtained from the collimated optical transmission reference scheme by taking all the values of the optical power received for the different milk concentrations when the concentration of the nanoparticle solution is 0 nM. In this case the optical attenuation is due solely to the scattering of the surrounding liquid phantom. Revisiting Beer's law (equation (2.2.9) from Chapter 2) for a pure scattering medium and substituting for the reduced scattering coefficient (equation (2.2.13)):

$$P = P_0 \exp\left(-\mu_{sca}^{'}d\right) \tag{5.5.3}$$

A plot of the received optical power, P, versus milk concentration is plotted in Figure 5.14:

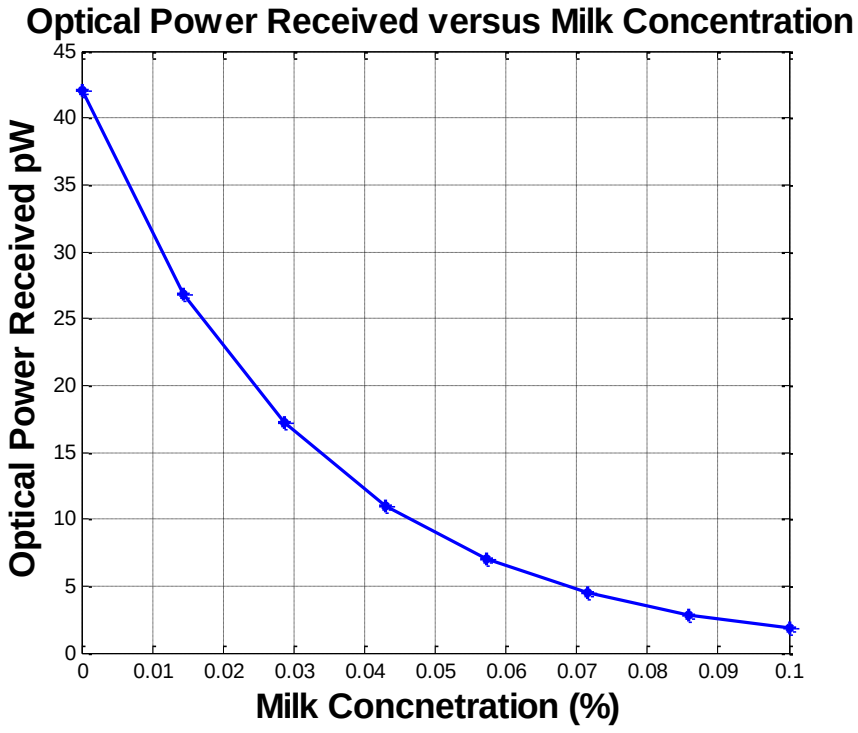

Figure 5.14 Optical power received from PMT versus milk concentration when the concentration of the SGNP solution is 0 nM.

With knowledge of the linear optical path distance of the tank, d_{sca}, (i.e. from the optoacoustic TOF analysis), the initial power received P_0, i.e. when the concentration of the scattering medium is 0 % (i.e. from the zero measurement), and the power received for each milk concentration, P_{milk}, the reduced scattering coefficient can be obtained using the information presented in Figure 5.14 and solving equation (5.5.3), given as:

$$\mu_{sca}^{'} = \frac{-1}{d_{sca}} \ln\left(\frac{P_{milk}}{P_0}\right) \tag{5.5.4}$$

In Figure 5.15 the reduced scattering coefficient, $\mu_{sca}^{'}$, versus the Milk concentration is presented, a linear fit of this plot demonstrates the validity of Beer's law and also provides a scattering coefficient of 3.16 cm^{-1} per % milk concentration. In [5.16] the authors have characterized both the scattering and absorption coefficient for milk in the green part of the visible spectrum quoting values of 3.596 cm^{-1} and 0.0015 cm^{-1} per % milk concentration, respectively. The slight discrepancy in the scattering coefficient between the results obtained and presented here to those obtained in [5.16] owes to the fact the different brands of milk produce diverse scattering coefficient values.

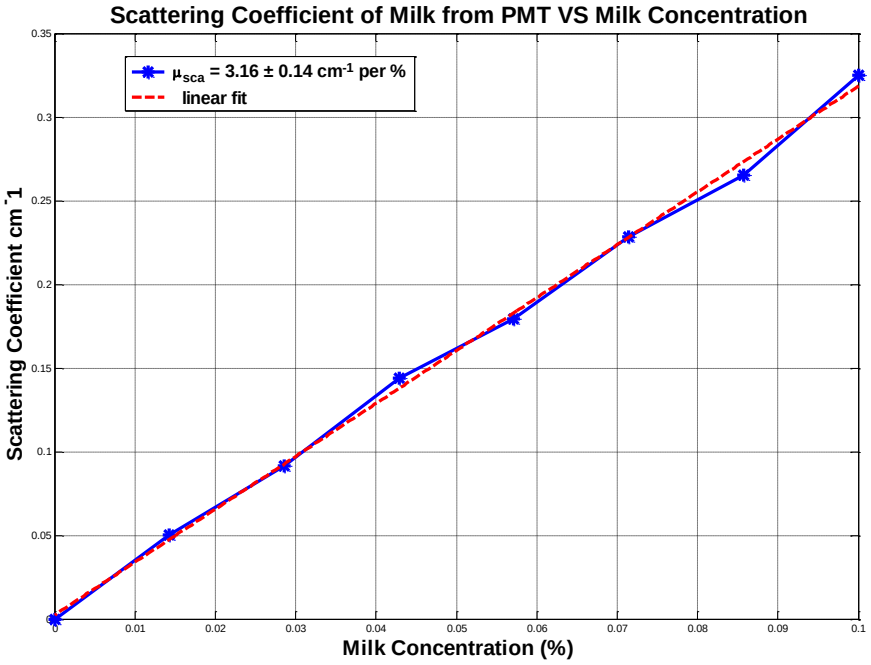

Figure 5.15 Scattering coefficient versus milk concentration, from a linear fit the scattering coefficient is determined as 3.16 ± 0.14 cm^{-1} per Milk concentration.

With knowledge of the scattering coefficient and the distances from the TOF analysis, the absorption coefficient can now be obtained from equation (5.5.2) for each concentration of the scattering medium. In Figure 5.16 a plot of the absorption coefficient versus nanoparticle concentration is provided for each milk concentration. The mean value of the absorption coefficient for each concentrations of the scattering medium is found to be 1.98 ± 0.05 cm^{-1} (per nM of the SGNP solution).

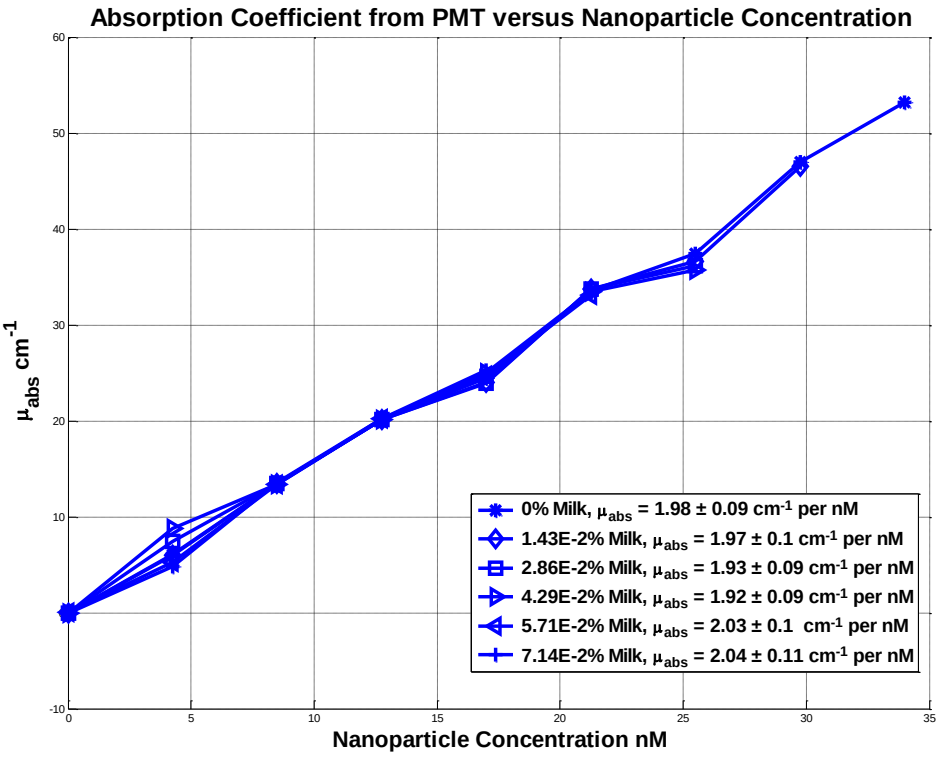

Figure 5.16 Absorption coefficient versus SGNP concentration for different concentrations of the scattering medium. The mean absorption coefficient is 1.98 ± 0.05 cm^{-1} (per nM of the SGNP).

5.5.3. Measurement Results and Quantification using the Optoacoustic Technique on the SGNP embedded in a Highly Scattering Medium.

For each concentration of the surrounding medium and each concentration of the SGNP solution, the amplitude of the amplified optoacoustic signal taken from the acoustic resonant transducer is recorded. The behaviour of the system has been plotted in Figure 5.17 for milk solution concentrations ranging from 0 % to 0.1 % and for SGNP solution concentrations ranging from 0 nM to 42 nM. The expected behaviour of the system predicted by equation (5.3.6) is clearly seen. Note that as the scattering coefficient of

the surrounding medium increases the amplitude of the optoacoustic signal is seen to decrease, this is explained by the attenuation of the optical energy reaching the sample.

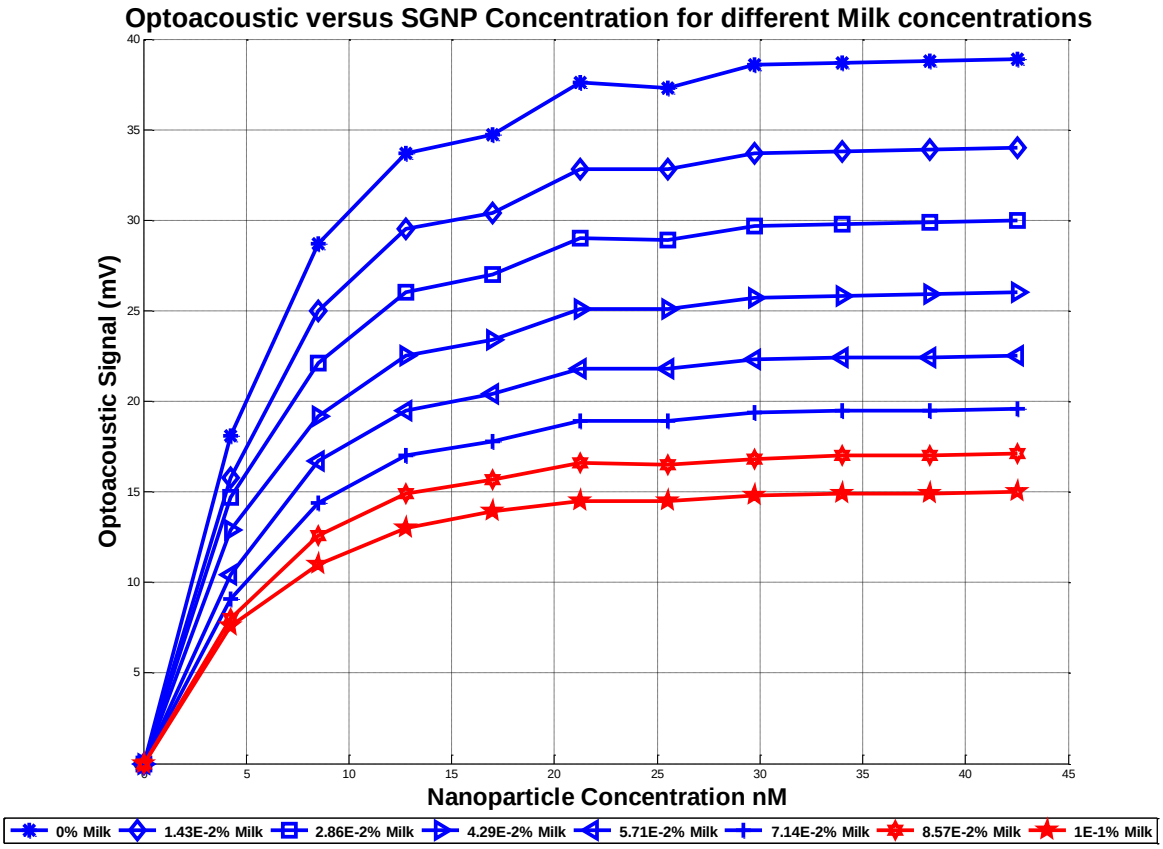

Figure 5.17 Optoacoustic signal response to different concentrations of a SGNP solution surrounded by different concentrations of the scattering matrix.

To determine the absorption coefficient of the SGNP solution, again knowledge of the scattering coefficient must be known. This value has been obtained using the optoacoustic technique. As opposed to the collimated optical transmission technique, the absorbing sample must be present to measure the scattering coefficient. The scattering coefficient is measured from the decrease in amplitude of the acoustic transients for increasing concentrations of the milk solution obtained for a single SGNP solution concentration. In Figure 5.18 a plot of the optoacoustic signal amplitude generated versus the surrounding mediums diluted milk concentration is presented for a single SGNP solution concentration of 32 nM.

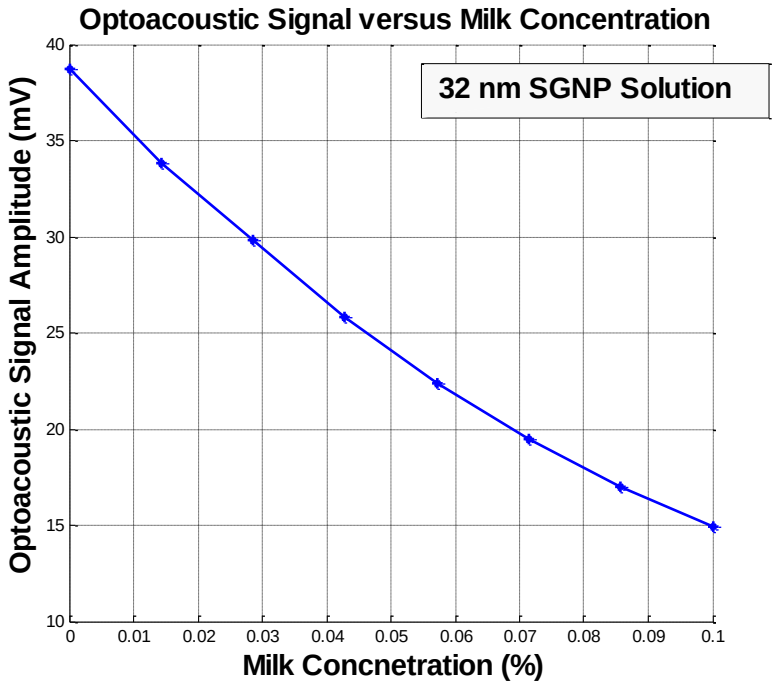

Figure 5.18 Optoacoustic signal generated versus Milk concentration for a 32 nm SGNP solution.

To obtain the reduced scattering coefficient from Figure 5.18 use is again made of equation (5.5.4). This process has been repeated for each SGNP solution concentration and the results in terms of the milk concentration are plotted in Figure 5.19. A mean reduced scattering coefficient of $\mu_{sca}^{'}$ = 3.19 ± 0.06 cm^{-1} (per % diluted milk concentration) has been obtained.

With knowledge of the scattering coefficient and the linear dimensions provided from the TOF analysis, the absorption coefficient of the SGNP solution can be calculated. In Figure 5.20 the absorption coefficient versus SGNP solution concentration is presented for each concentration of the surrounding scattering matrix. The mean value of the absorption coefficient over all the different concentrations of the scattering medium has been obtained experimentally as 1.96 cm^{-1} ± 0.06 cm^{-1} (per nM of the SGNP solution).

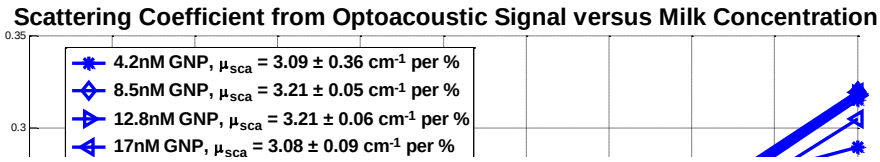

Figure 5.19 Reduced scattering coefficient versus diluted milk concentration for each concentration of the SGNP solution. The mean reduced scattering coefficient has been found experimentally to be 3.19 ± 0.06 cm^{-1}.

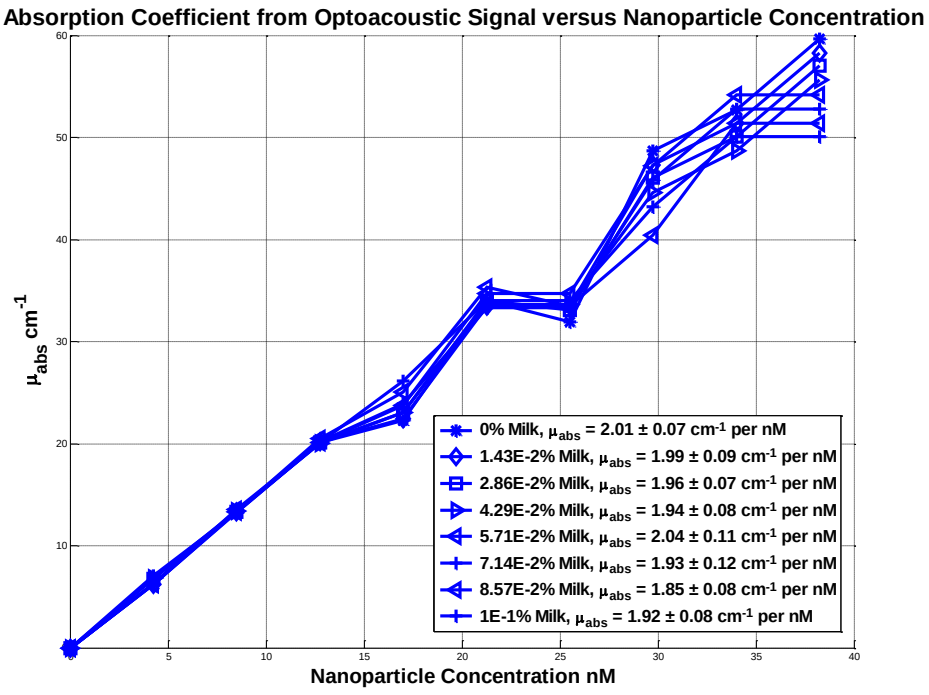

Figure 5.20 Absorption coefficient versus SGNP solution for each value of the diluted milk surrounding scattering matrix.

5.5.4. Comparative Analysis of Results.

A quantitative analysis has been provided for different concentrations of a synthesized 15 ± 2 nm diameter SGNP ranging in concentration from 4.2 nM to 42 nM and embedded in a highly scattering media composed of different diluted milk solutions. In order to obtain the absorption coefficient of the SGNP solution, using both techniques, knowledge of two different key parameters are required. First, the linear dimensions of the different optical media, d_{sca} and d_{abs}, and second, the scattering coefficient of the surrounding liquid phantom. The former parameter has been obtained from a temporal analysis of the optoacoustic signals produced where $d_{sca} = 42\,\text{mm}$ and $d_{abs} = 2\,\text{mm}$. This TOF analysis highlights one of the major advantages of this method over standard transmission and/or any other spectroscopic measurement scheme where dimensional information may not be obtained.

The reduced scattering coefficient has been measured experimentally, using the dimensional information, to be 3.16 ± 0.14 cm^{-1} and 3.19 ± 0.06 cm^{-1} per % concentration using the collimated optical transmission and optoacoustic technique, respectively. It may be observed that the results obtained from both techniques are in good agreement, and are also in close agreement with results from other authors on the milk scattering coefficient [5.16].

With knowledge of the dimensions of both the scattering and absorbing media and with the scattering coefficient it has then been possible to quantify the absorption coefficient of the embedded SGNP solution. The results obtained from the collimated optical transmission and optoacoustic technique were 1.98 ± 0.05 cm^{-1} and 1.96 ± 0.06 cm^{-1} per nM, respectively. The results for both the scattering and absorption coefficient are in good agreement.

The increased sensitivity of the optoacoustic technique to the measurement of the absorption coefficient of spherical nanoparticles within the surrounding scattering medium has also been observed and is clearly seen in Figure 5.17. For concentrations of the milk medium beyond 7.14 10^{-2} % the amount of light reaching the PMT detector is below its optical power response threshold of 0.5 pW (data taken from datasheets).

5.6. Conclusions.

In this chapter a comprehensive study of the feasibility of the optoacoustic technique to quantify the optical properties of an absorbing SGNP solution embedded within a highly scattering medium has been presented. The experimental scheme designed for this procedure, described in Chapter 4, has involved optoacoustic signal generation at a single source wavelength of 532 nm. The scheme has incorporated a parallel collimated optical transmission setup, under the same experimental conditions, and is used as a reference, allowing a comparative analysis of all the results obtained.

Preliminary trials have been performed on a known absorber, based on different concentrations of ink, where the results obtained for the absorption coefficient have been 3.67 ± 0.3 cm^{-1} and 3.65 ± 0.2 cm^{-1} using the optoacoustic technique and reference measurement, respectively. Agreement is observed between both measurement techniques and with the absorption coefficient measured at 532 nm using a commercial spectrophotometer. The absorption coefficient also concurs with values quoted for the absorption coefficient of ink by other authors [5.1]. These preliminary experimental trials have motivated subsequent trials on a 20 ± 2 nm diameter SGNP solution, in this case the absorption coefficient was measured to be 17.18 ± 0.8 cm^{-1} and 17.35 ± 0.5 cm^{-1} (per normalized nanoparticle concentration) for the optoacoustic and reference scheme, respectively. It may be observed that close agreement is again observed.

The objective of this quantitative measurement scheme, and the research work presented in this thesis, has been to quantify the optical absorption coefficient of a SGNP solution embedded within a scattering medium. A final set of experimental tests have been devised to test the versatility of optoacoustics when faced with this particular situation. The experimental setup has involved embedding an absorbing SGNP solution within a diluted milk solution which is commonly used to simulate the scattering properties of human soft tissue. The colloidal solution used for these trials contained gold spheres with a diameter of 15 ± 2 nm. The tests have been performed on concentrations of the SGNP solution ranging from 4.2 nM to 42 nM and for concentrations of the diluted milk surrounding medium ranging between 0 % to 0.1 % over a distance of 42 mm. Both the scattering coefficient of the surrounding medium and absorption coefficient of the SGNP solution have been obtained using both techniques. Using the reference

collimated optical transmission technique the attenuation coefficients were determined to be μ_{sca} = 3.16 ± 0.14 cm^{-1} and μ_{abs} = 1.98 ± 0.05 cm^{-1} and for the optoacoustic technique μ_{sca} = 3.19 ± 0.06 cm^{-1} and μ_{abs} = 1.96 ± 0.06 cm^{-1}.

The experimental results presented in this chapter for a single laser wavelength of 532 nm are seen to be in close agreement for all experimental trials. The results presented have led to a recent publication in [5.13]. This analysis has motivated further investigation to determine the wavelength dependence of absorbing nanoparticle solutions embedded within scattering media. The results from this spectroscopic analysis will be presented in the following Chapter 6.

Chapter 6.

Experimental Results of Spectroscopic Analysis using New Optoacoustic System Design over the Wavelength range from 410 nm to 1000 nm.

6.1. Introduction

The feasibility of optoacoustics as a technique to quantify the optical properties of an absorbing spherical gold nanoparticle (SGNP) solution embedded within a highly scattering media has been established in Chapter 5. The reliability of this technique has been confirmed by means of a comparative analysis using a reference measurement scheme, based on collimated optical transmission. These preliminary quantitative experimental trials have motivated the further development of a *Laser Optoacoustic Spectroscopic* (LOS) system that is capable of determining the spectroscopic profile of gold nanostructures over the complete wavelength range from the visible part of the electromagnetic spectrum (410 nm) to the near-infrared (1000 nm).

The results presented in this chapter have been divided into two parts. The first, deals with the experimental analysis of a synthesized spherical gold nanoparticle (SGNP) solution where the particle diameters were 15 ± 2 nm. Preliminary trials using these particles embedded in distilled water have been designed to test the feasibility of LOS. The wavelength range covered has been defined using Rayleigh and Mie Theory in Chapter 3 (Section 3.4), and ranges from 450 nm to 650 nm.

The second set of results is based on the LOS analysis of a gold nanorod (GNR) solution. The numerical approach presented in Chapter 3 (Section 3.5) using Gan's extension to Mie Theory has identified the behavior of these particles. It has been demonstrated that these nanostructures can be tuned to specific wavelengths via there aspect ratio. The rod structures investigated in this chapter have an aspect ratio of 3.5, where the length of the rod is 35 nm and their diameter 10 nm. It has been confirmed from the theoretical review that optical absorption by the GNR solution is dominant. The wavelength range covered for this analysis goes from the visible to NIR, from 410 nm to 1000 nm. As part of the objectives of this work and to further demonstrate the capabilities of the LOS system, these nanostructures have been embedded in a high scattering medium.

A comparative analysis using the data obtained from the reference measurement scheme and those from a commercial offline spectrophotometer show close agreement for each nanostructure solution.

6.2. Absorption Spectroscopic Analysis

The objective of the short pulsed optoacoustic spectroscopic scheme implemented has been to measure the spectral signature pertaining to gold nanostructures that are embedded in a high scattering medium. The difficulties arising when using this technique evolve around the variation in optical power from the short pulsed laser source. In this sense the collimated optical transmission scheme is seen to be more affected, as to obtain the absorption coefficient a previously measured baseline is required, this is illustrated in:

$$\mu_{abs}(\lambda) = \frac{-1}{d} \ln\left(\frac{P_{sample}(\lambda)}{P_0(\lambda)}\right) \qquad (6.2.1).$$

It may be appreciated in the following Figure 6.1 from the measurements of both the baseline, P_0, and nanorod solution, P_{sample}, that the system is very sensitive to changes in optical power, where the maximum optical power difference measured is close to 6 pW.

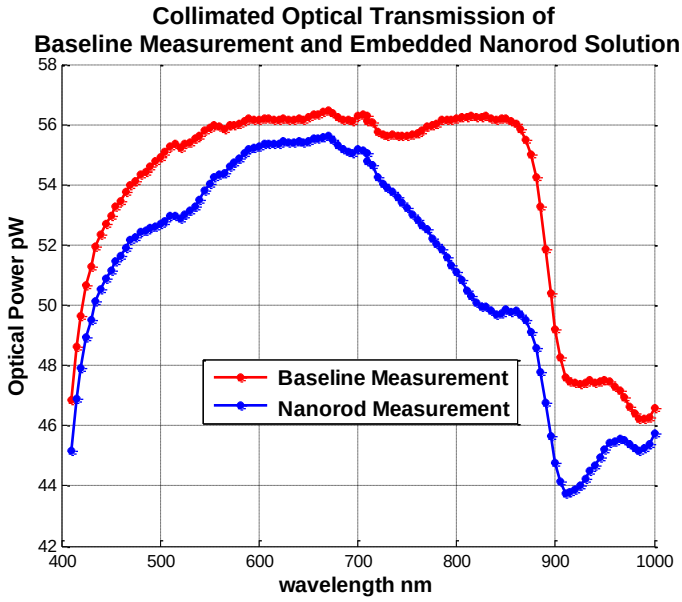

Figure 6.1 Baseline measurement and measurement when the nanorod simple is in place over the spectral range from 410 nm to 1000 nm.

This is not as critical for the optoacoustic technique as the optical power is corrected in real time using the monitor BPW34 photodiode. Similar power monitoring has been carried out by other authors in [6.1-6.3] where more details regarding these procedures are presented in Appendix E.

6.3. Spectroscopic analysis of a SGNP solution between 410 to 650 nm Embedded in a Distilled Water Medium

In the previous chapter the absorption coefficient of both a 20 ± 2 nm and 15 ± 2 nm diameter SGNP solutions have been experimentally quantified at a single wavelength of 532 nm. In this section, a spectral characterization of the synthesized 15 ± 2 nm diameter SGNP solution will be performed over the visible wavelength range of 450 nm to 650 nm in steps of 5 nm using a Nd:YAG pumped OPO and the experimental LOS scheme described in Chapter 4 Section 4.4. The operating wavelength and data acquisition have been controlled using a specifically designed Matlab™ program and has provided a direct comparative analysis between the results from both measurement techniques.

6.3.1. Collimated Optical Transmission Spectroscopy for a 15 nm SGNP between 450 nm and 650 nm

The first step taken in this process has been to measure the baseline over the complete wavelength range. This measurement is stored in the acquisition software to calculate the absorption coefficient (using equation**¡Error! No se encuentra el origen de la referencia.**) and provides a direct comparative analysis of the spectral information obtained with the optoacoustic technique.

In Figure 6.2 the spectral profile from the synthesized 15 nm diameter SGNP solution using the reference scheme is presented. The peak absorption, due to the surface plasmon resonance (SPR), has been observed to occur at 520 nm. The spectroscopic profile and the location of the peak absorption are in agreement with the theoretical findings using Rayleigh and Mie theory presented in Chapter 3 for SGNP solutions with the same dimensions.

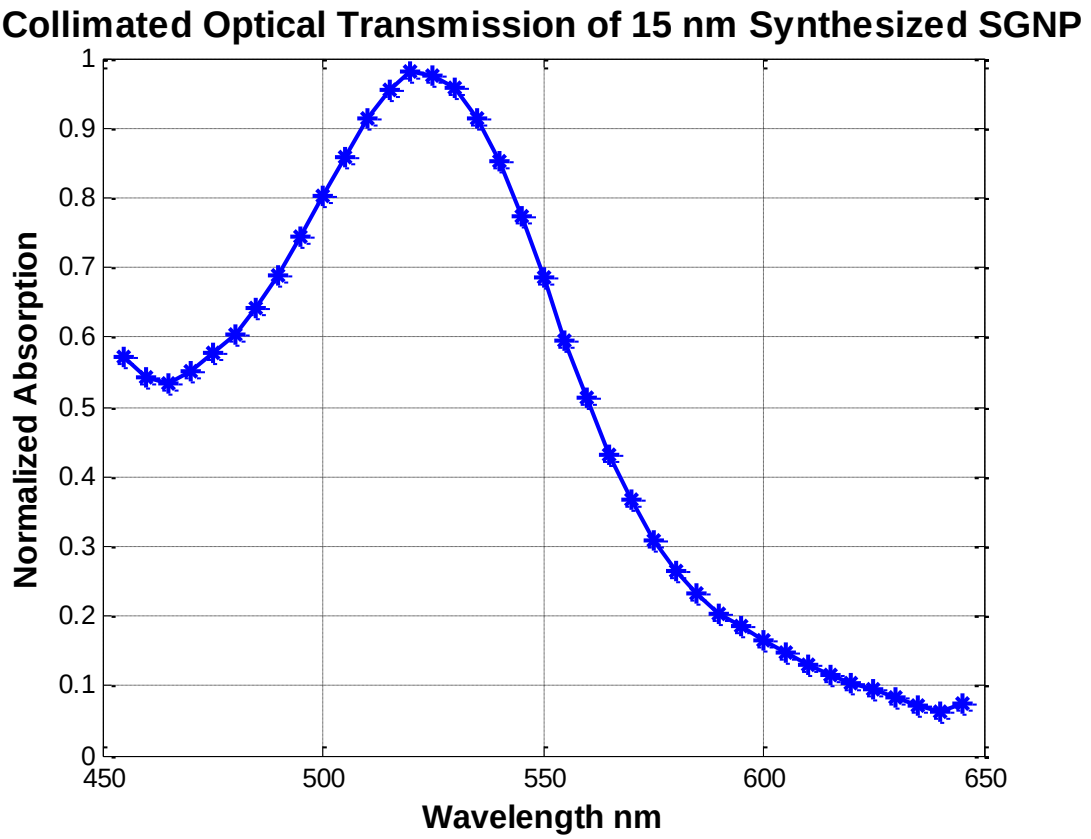

Figure 6.2 Collimated optical transmission of synthesized 15 nm diameter SGNP, the peak absorption is located at 520 nm.

6.3.2. LOS of 15 nm SGNP Between 410 and 650 nm

The results presented in the previous section will be used to confirm the feasibility of the optoacoustic spectroscopy for the same 15 nm diameter SGNP solution. The acoustic signal is acquired from the PZT transducer and its amplitude is adjusted according to the input optical power obtained from the monitor BPW34 photodiode scheme.

The experimental results obtained from the LOS analysis of the SGNP solutions, over the predetermined wavelength range from 450 nm to 650 nm in steps of 5 nm are presented in Figure 6.3. The spectroscopic response has been normalized to the peak signal value. The location of the peak absorption band of the SGNP solution was observed experimentally to be situated at 520 nm.

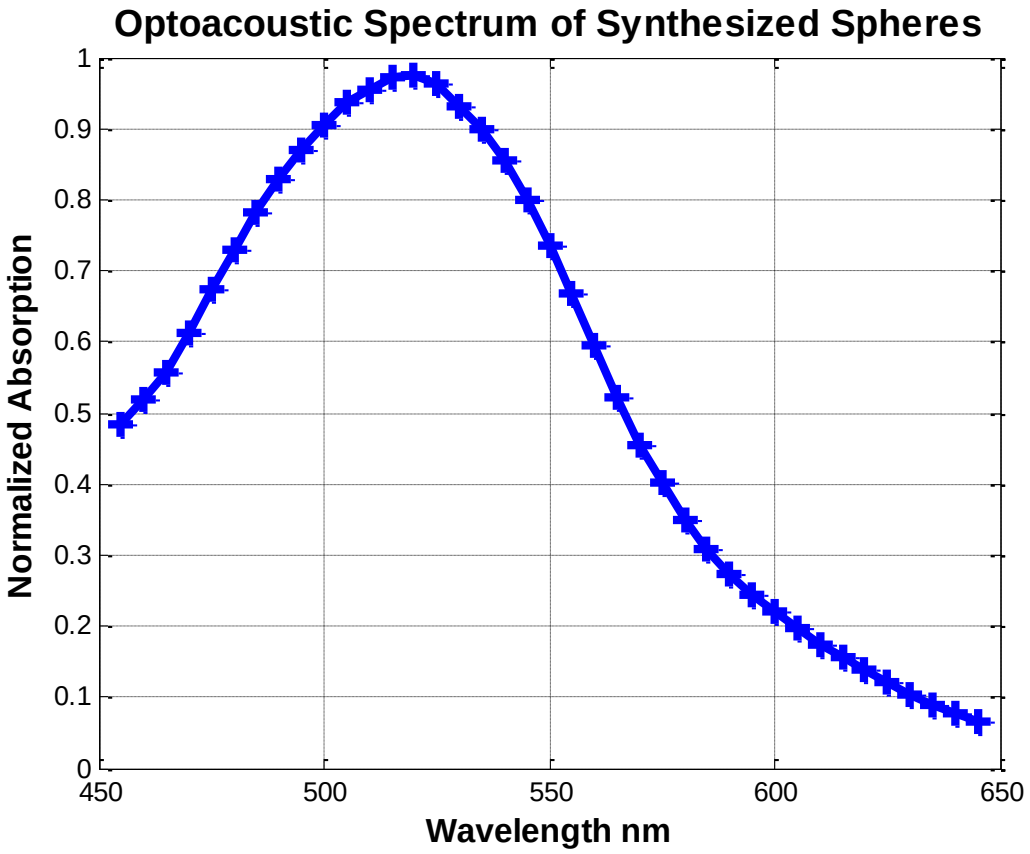

Figure 6.3 LOS profile of 15 nm diameter synthesized SGNP with the peak absorption located at 520 nm.

6.3.3. Comparative Analysis of Experimental Results Obtained

For the wavelength range considered in these preliminary trials (from 450 nm and 650 nm) both spectroscopic techniques, i.e. the reference and optoacoustic scheme are seen to be in agreement. The position of the main absorption peak is located at 520 nm in both cases. This absorption peak is in agreement with work performed by other authors on spherical gold nanoparticle characterization [6.4-6.5]. To ensure the accuracy of the experimental results, they have been compared with results obtained from a commercial offline spectrophotometer (Lamda 14 Perkin Elmer). In Figure 6.4 these results are presented where it may be observed that not only the position of the maximum absorption band coincides but also the shape of the spectral profile over the complete wavelength range.

Even though this analysis demonstrates positively the optoacoustic experimental procedure, several discrepancies occur between the different measurement techniques. Comparing the results from the LOS system, the maximum error in the spectral width (at 80 % of the maximum) is 20 %. For the collimated optical transmission the

corresponding error is 6 %. The error sources have been identified as fluctuations in the optical power of the laser source.

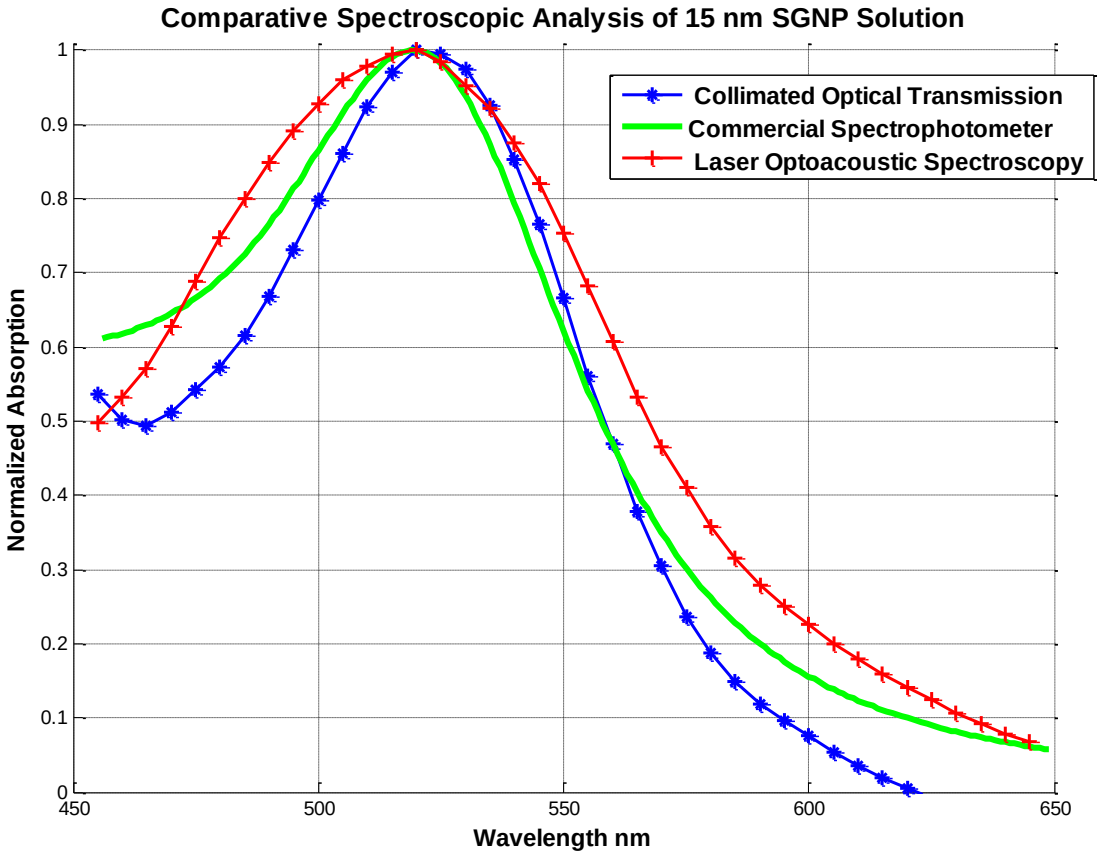

Figure 6.4 Comparative analysis of three different measurement techniques to determine the spectroscopic profile of a 15 nm SGNP solution.

6.4. Spectroscopic Analysis of a Gold Nanorod Solution from 410 nm to 1000 nm Embedded in a Liquid Biomedical Phantom

The previous section has discussed the spectroscopic analysis of a SGNP solution within the visible region of the electromagnetic spectrum (from 450 nm to 650 nm). From the experimental analysis error sources have been defined and the experimental scheme has been modified, as described in Chapter 4 Section 4.5. In this section experimental results from a spectroscopic analysis will be presented over the wavelength range from the visible to NIR of a commercial optically absorbing GNR solution (30-PM-850 from Nanopartz). The aspect ratio of the nanoparticle solution is 3.5, (rod length 35 nm, rod diameter 10 nm). The stock nanorod solution has a concentration of 3.2 10^{13} particles per milliliter. Here, results from the collimated optical transmission reference will be presented and compared to results obtained from the LOS system.

6.4.1. Collimated Optical Transmission Spectroscopy of Gold Nanorod Solution Between 410 nm and 1000 nm

The modified experimental scheme makes use of a fiber coupled PMT optical detector with increased responsivity (3.6 10^4 A/W) to detect the attenuated transmitted light. The acoustic signals generated are captured directly without the use of an amplifier. As part of the objectives of this experimental scheme, the GNR solution has been embedded in a highly scattering medium composed of diluted milk, see Chapter 4 Section 4.3. It has been ensured that the diluted milk solution, liquid phantom, is homogeneous by continually stirring it before and after measurements. The experimental spectral results are presented in Figure 6.5 where the typical spectroscopic response expected from a GNR colloidal solution may be observed, the two peaks correspond to the transverse and longitudinal surface plasmons (TSP and LSP), and are located at 514 nm and 844 nm, respectively. For comparative purposes the ratio between the amplitude of the first and second peak has been measured to be 0.34.

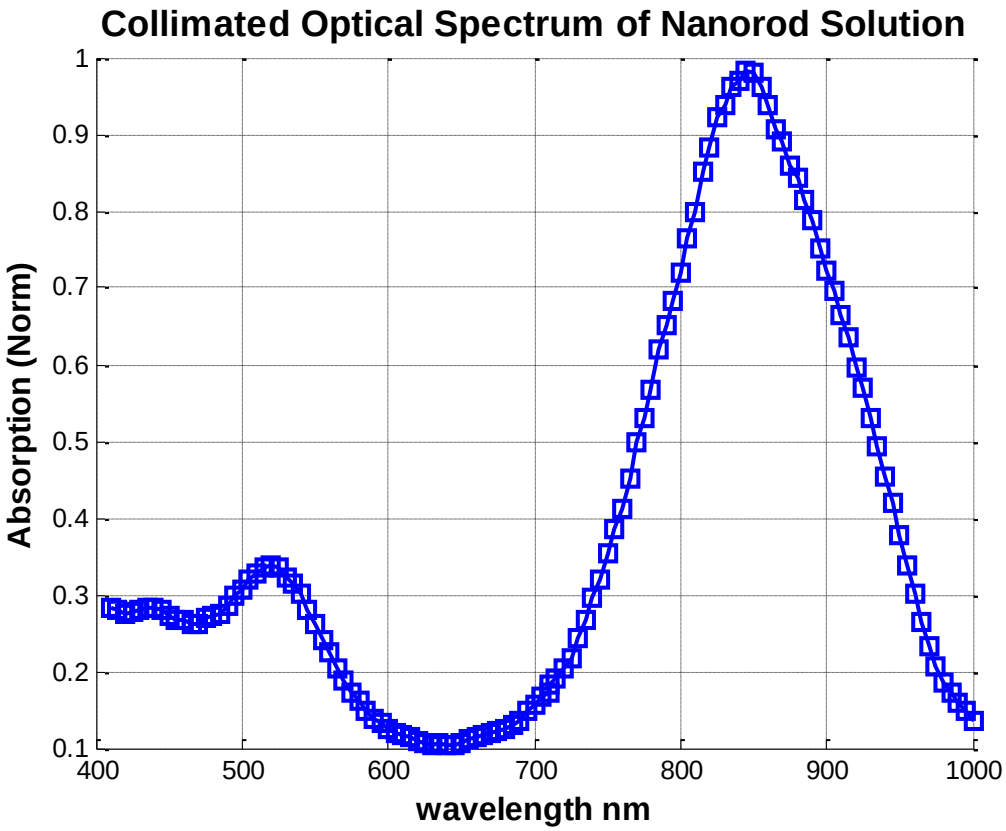

Figure 6.5 Collimated optical transmission spectroscopic results of the commercial gold nanorod solution over the wavelength range from 410 nm to 1000 nm.

6.4.2. LOS of Gold Nanorod solution between 410 and 1000 nm

As in the case of the SGNP, the experimental results obtained from reference measurement scheme will be used to verify the feasibility of the LOS. The experimental results obtained from the LOS system are presented in Figure 6.6, again the expected two peak response due to the splitting of the surface plasmon into transverse modes and longitudinal modes, TSP and LSP, respectively may be observed. These position of these peaks are 514 and 844 nm, respectively. These values are in agreement with those obtained from the reference measurement scheme (see Figure 6.5). The ratio between the amplitude of the first and second peak, 0.34, also corresponding to the previous optical transmission measurement.

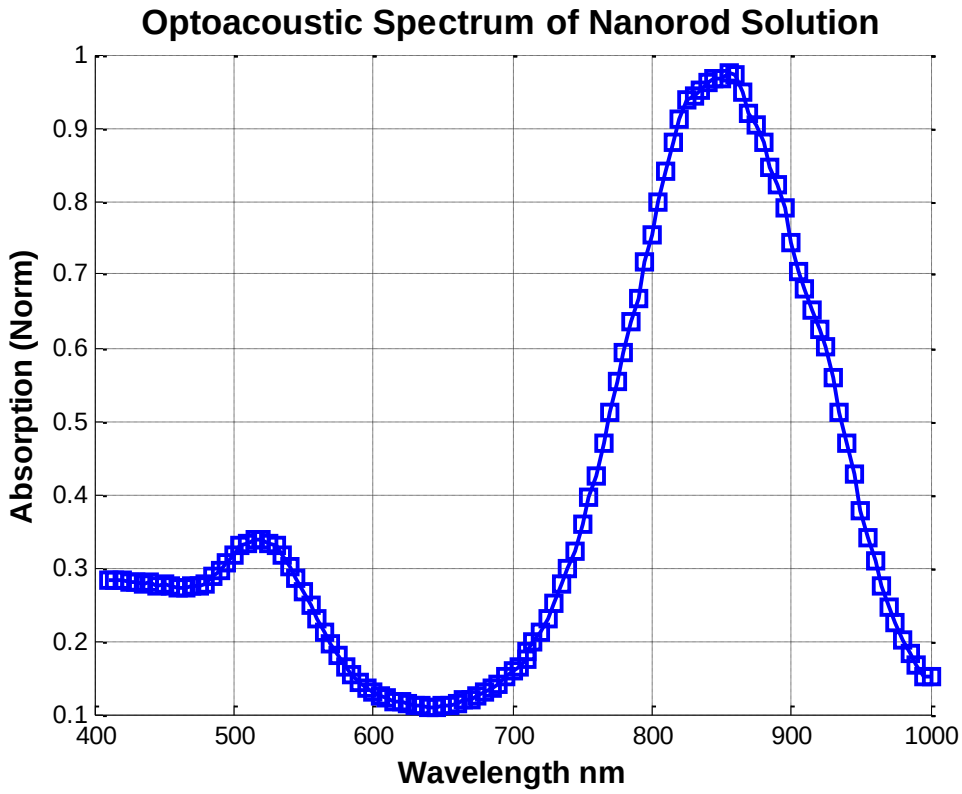

Figure 6.6 LOS response of the gold nanorod solution over the wavelength range from 410 nm to 1000nm.

6.4.3. Comparative Analysis of Experimental Results Obtained

To further investigate the feasibility of the results obtained, the spectral profiles from both measurement schemes have been compared to those from a commercial spectrophotometer (Lambda 14 PerkinElmer). In Figure 6.7 (a) a combined plot is presented of the spectral profiles obtained from the collimated optical transmission and spectrophotometer. Both profiles are normalized to their maximum value. In Figure 6.7 (b) a similar combined plot for the results from the optoacoustic spectroscopy measurement and the spectrophotometer is presented.

When compared to the results from the spectrophotometer, the errors in the amplitude of the first maximum (514 nm) are 3.2 % and 4.1 % for the optoacoustic and reference scheme, respectively. The maximum errors in the spectral width of the second peak (844 nm) are 2.3 % and 8 % for the optoacoustic and reference scheme, respectively. These errors correspond to instrumental errors of the system, particularly the optical power measurements of the pulsed OPO source at each wavelength. The optical transmission scheme is seen to be more affected.

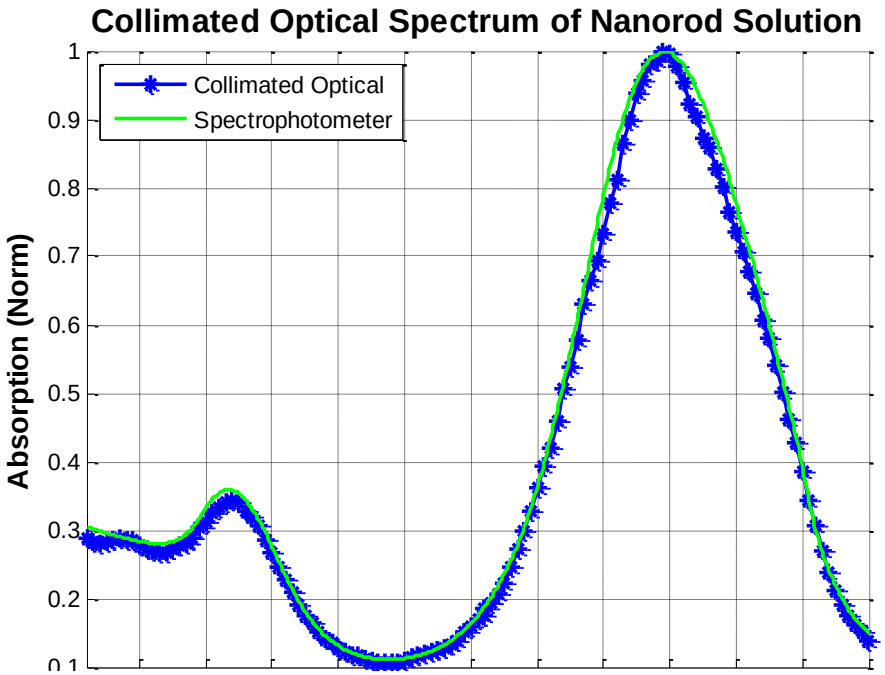

(a)

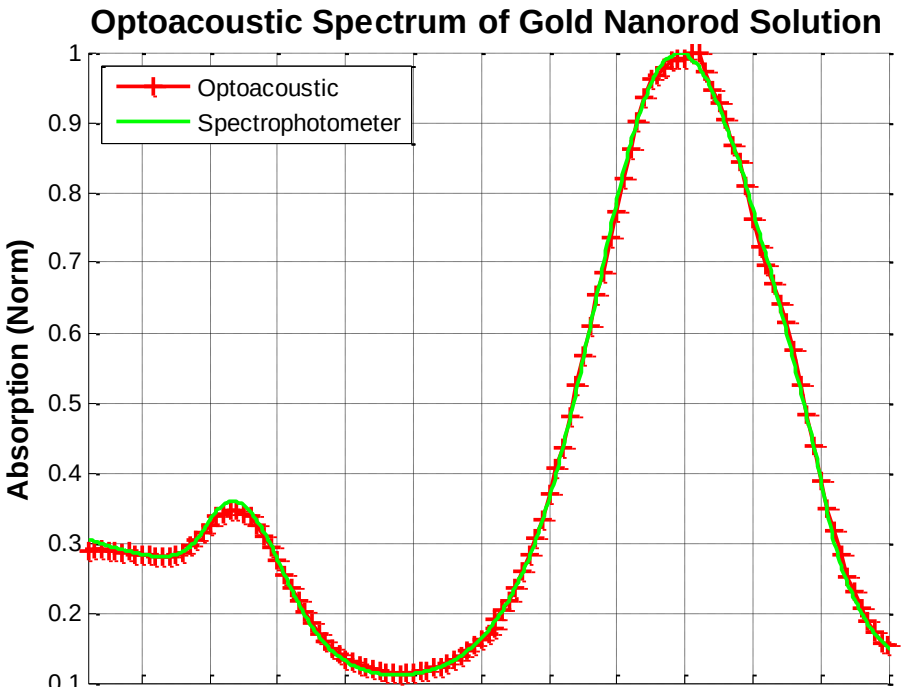

(b)

Figure 6.7 (a) Combined plot of reference collimated optical transmission and commercial spectrophotometer plots and (b) Combined plot of LOS measurements and commercial spectrophotometer plot, over the wavelength range from 410 nm to 1000 nm.

The exact source of the experimental errors is difficult to ascertain and arise from a combination of different factors. Two different possibilities have been considered that are related to the comparative analysis with the commercial spectrophotometer. First, and due to the limited sensitivity of this device, a dilute solution (10 %) is required to obtain the spectroscopic results. Secondly, and again due to the sensitivity limitations of the spectrophotometer measurement, the GNR solution is not embedded in a scattering matrix. It is common knowledge that nanoparticle solutions aggregate with time, producing larger particles and changing the optical properties of the colloidal solution.

Regarding the collimated optical transmission spectroscopic measurement, the results obtained are based on an analysis with a 'baseline' or 'zero reference' measurement, which has been taken and stored in the memory of the computer to perform the necessary calculations for the spectroscopic analysis. Any changes in the experimental setup over time have an important impact on the results obtained. Due to this procedure two different error sources have again been identified here: First, the optical power emitted by the laser source has been observed to deviate slightly and has required recalibration between measurements. Secondly, due to slight deviations in the position of the cuvette, this occurs when exchanging the cuvette with the distilled water 'reference' sample for the cuvette containing the nanorod solution. Any changes in the optical power or position of the cuvette will change the spectroscopic profile.

Regarding the optoacoustic experimental setup, the error sources previously described do not affect the optoacoustic analysis as no baseline measurement is required. There are no problems with changes in the optical power as the BPW34 monitor photodiode has been used for real time incident power calculations. Since there is no interchange with a 'reference' cuvette, no errors arise from the positioning of the cuvette. The error observed in the LSP peak may arise from the increase in temperature due to the high level of absorption. Changes in temperature affect the stability of nanoparticle solutions, and also affect the amplitude of the optoacoustic signal [6.6]. For high levels of absorbed power the particles aggregate, producing larger particles [6.7]. High levels of absorbed energy may even lead to particle destruction [6.8]. A direct comparison of the three different techniques is presented in Figure 6.8 where close and good agreement between all three methods may be observed.

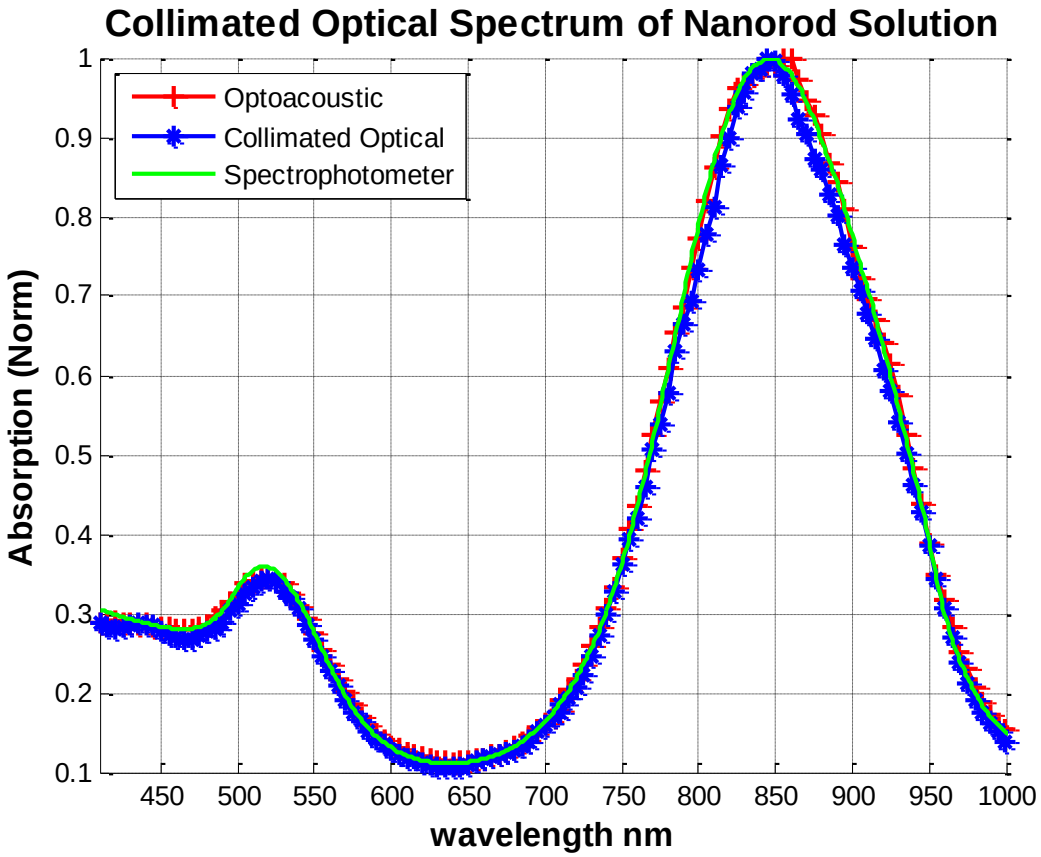

Figure 6.8 Combined spectroscopic profile obtained from the LOS, reference measurement scheme and commercial spectrophotometer.

6.5. Estimation of the absorption coefficient from spectroscopic analysis

In Chapter 2 Section 2.3 it has been shown that the initial pressure signal p_0 generated is proportional to the absorption coefficient of the medium as:

$$p_0 = E_{abs}\Gamma = \mu_{abs}F_0\Gamma \tag{6.5.1}$$

Where the energy absorbed is equal to the product of the fluence of the laser source incident on the absorber, F_0, and the absorption coefficient, μ_{abs}, of the medium. The dimensionless Grüneisen parameter is a temperature dependent constant [6.9] and provides the ratio of the laser energy that is available for conversion into acoustic energy and is given by [6.10]:

$$\Gamma = \frac{\beta v_{med}^2}{C_p} \tag{6.5.2}$$

Where β is the thermal coefficient of volume expansion, C_p, is the heat capacity at constant pressure, and v_{med} is the longitudinal wave speed in the medium. Muscle contains roughly 75 % water, taking this as an example, the volume expansion coefficient is $\beta \approx 3.8\times10^{-4}\,\mathrm{K}^{-1}$, the heat capacity is $C_p = 3.7\,\mathrm{mJ/(g\ mK)}$, and the speed of sound in muscle is $v = 1.5\,\mathrm{mm/\mu s}$. From equation (6.5.2) this gives the Grüneisen parameter ~ 0.23 in muscle [6.11]. In water the value of the Grüneisen parameter is 0.1 [6.12].

The nominal energy of the laser source at 844 nm, which is the location of the LSP peak, which enters liquid phantom has been measured using the monitor photodiode to be 6 mJ. When the optical radiation enters the tank containing the scattering medium it is attenuated according to the scattering coefficient of the milk which has been measured using a commercial spectrophotometry. The light energy at the location of the cuvette filled sample is calculated to be 1.2 mJ. Considering that the optical irradiation is highly scattered and that the surface area of the cuvette containing the nanorod solution is 1 cm x 2 cm (2 x 10^{-4} m^2) then the energy fluence incident on the cuvette is 6 J/m^2.

The pressure generated by the optoacoustic signal is generally obtained using the sensitivity of the acoustic transducer in Pa/V. The acoustic transducer has been calibrated using a wideband ultrasonic transducer (WAT-13, Fairway Medical Technologies Inc.) and the sensitivity has been determined as 3.2 kPa/V. The optoacoustic signal generated at 844 nm is presented in Figure 6.9, where the amplitude of the first resonant peak is 250 mV, thus the pressure of the signal generated is 0.8 kPa.

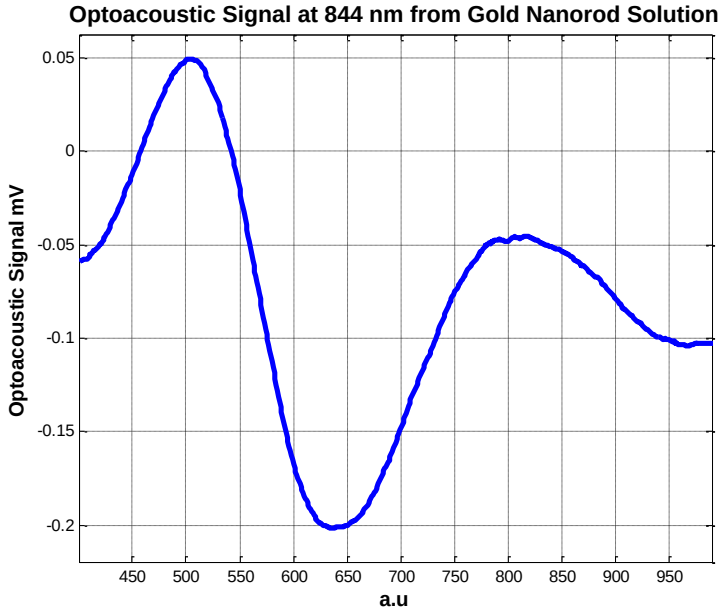

Figure 6.9 Optoacoustic signal generated by gold nanorod absorber at 844 nm.

Solving equation (6.5.1) for the absorption coefficient gives:

$$\mu_{abs} = \frac{p_0}{F\Gamma} \tag{6.5.3}$$

Inserting the values for the pressure generated (0.8 kPa), the fluence of the laser source incident on the sample (6 J/m^2) and the Grüneisen parameter (0.1) gives an estimation of the absorption coefficient as 13.36 cm^{-1}.

For the collimated optical transmission the absorption coefficient is obtained using equation (6.2.1) by comparing the power received at 844 nm when the GNR solution is in place, $P_{sample}(\lambda)$, to the power received from the zero measurement $P_0(\lambda)$ at the same wavelength. From this analysis the absorption coefficient is determined to be 13.7 cm^{-1}.

The value for the absorption coefficient at the LSP peak from the spectrophotometer has been measured as 14 cm^{-1}. However, it must be highlighted that this measurement has not been performed in parallel and that the sample used has been diluted in order to perform the measurement. It can be seen that the estimated value for the absorption coefficient from the optoacoustic technique and the value obtained from the reference measurement scheme are in close agreement with that obtained from the commercial spectrophotometer.

6.6. Conclusions

In this Chapter 6 the experimental results for a spectroscopic analysis of two different gold nanostructure colloidal solutions has been presented for the wavelength range from 410 nm to 1000 nm. This experimental analysis has been motivated by the success of the quantitative analysis presented in Chapter 5. The theoretical analysis based on Mie theory, presented in Chapter 3 has served to identify the optical properties of each nanostructure solution and to define the experimental parameters required for their spectroscopic analysis.

Preliminary spectroscopic trials using a 15 ± 2 nm diameter SGNP solution located within a distilled water solution have been carried out using both optoacoustics and collimated optical transmission. The results obtained clearly identify the absorption band due to the SPR of the spherical gold particles. A detailed analysis of the results shows that the position of the peak absorption is at 520 nm and is in good agreement for both techniques. The results presented here for the spectroscopic analysis of gold nanospheres have recently been published in [6.13].

The second part of this chapter has dealt with the optoacoustic spectroscopic analysis of a commercial gold nanorod structure (30-PM-850 from Nanopartz) with aspect ratio of 3.5. From the theoretical analysis presented in Chapter 3 (Section 3.5), using Gan's extension to Mie theory, it has been shown that the optical attenuation of such particles is dominated by optical absorption.

The experimental results obtained from both the optoacoustic and reference measurement scheme demonstrate the typical splitting of the surface plasmon into the transverse and longitudinal modes, TSP and LSP, respectively. The TSP peak is located at 514 nm and the LSP at 844 nm using both techniques. The results have been compared to those from a commercial spectrophotometer, regarded as the gold standard measurement technique. The position of the peaks is in good agreement for all three methods. Comparing the results to the spectrophotometer, the errors in the amplitude of TSP maximum are 3.2 % and 4.1 % for the optoacoustic and reference scheme, respectively. The maximum errors in the spectral width of the second peak (844 nm) are 2.3 % and 8 % for the optoacoustic and reference scheme, respectively. The

experimental results presented in this section using the optoacoustic scheme have led to a recent publication in [6.14].

Finally, using the optoacoustic signal generation concepts presented in Chapter 2, a quantitative estimation of the absorption coefficient of the nanorod solution from the optoacoustic technique has provided a value of 13.4 cm^{-1} at the LSP peak of 844 nm. The absorption coefficient calculated from the collimated optical transmission at the same wavelength was 13.7 cm^{-1}, both of these values are in close agreement with the absorption coefficient of 14 cm^{-1} obtained from a commercial spectrophotometer. The feasibility of the optoacoustic technique for quantitative spectroscopic analysis of absorbers embedded within a turbid media has been confirmed.

Chapter 7.

Conclusions

This thesis has presented results from two experimental schemes specifically designed to quantify and spectrally characterize the absorption of gold nanoparticles embedded in a high scattering medium. To implement these systems a conceptual understanding of the behavior of light in turbid media as well as the processes involved in the optical to acoustic conversion is required.

This study has begun with a review of the optical propagation in attenuating media, where two key parameters associated with this process have been defined; optical absorption and optical scattering. These are characterized by the absorption and scattering coefficients, μ_{abs} and, μ_{sca}, respectively. According to Beer's law, the optical energy traversing an attenuating homogeneous absorption or, scattering medium is seen to decrease exponentially where the decay constant is directly proportional to the attenuation coefficients of the medium. For efficient optoacoustic signal generation, due to thermoelastic expansion of the optically irradiated medium, the absorbed optical energy must be both stress and thermally confined. It has been demonstrated that the amplitude of the initial induced pressure transient is directly proportional to the optical energy absorbed.

The importance of colloidal gold solutions, as optical contrast agents in optoacoustic biomedical applications, to increase the absorption of optical energy in areas where scattering is dominant, has prompted the study presented in this thesis for their characterization and quantification. The source of the unique optical properties of such nanostructures has been presented in Chapter 3, it has been illustrated that clearly defined extinction bands due to surface plasmon resonance exist. The location of these attenuation peaks is directly related to the geometrical structure and size of the particles.

A numerical spectral analysis of homogeneous spherical particles using Mie theory has shown the dependence of the spherical particles diameter on the contribution of both optical absorption, and scattering, to the total optical energy extinction. The results have

shown that particles with diameters less than 60 nm efficiently absorb optical energy in the visible part of the spectrum and the scattering component can be depreciated. The theoretical review of SGNP has provided key experimental parameters for both optoacoustic characterization schemes. It shows that the ideal wavelength of the optical source for quantification should be close to 520 nm, and the spectral range of interest is between 450 nm and 650 nm.

Also in Chapter 3, an extension of Mie theory developed by Gans has provided insight into the behavior of gold nanorods. The numerical analysis presented has been used to examine the dependence of the aspect ratio, and medium dielectric constant, on the position of the surface plasmon resonance peaks. Also, the dependence of the length and diameter of gold nanorods on the absorption and scattering has been presented. This mathematical analysis has again provided crucial information required for the optoacoustic spectroscopic scheme, where it has been demonstrated that the embedded commercial gold nanorods that have been spectrally characterized, are highly absorbing and, that the effect of scattering is neglected.

In Chapter 4 the measurement concepts of the optical properties using optoacoustics have been introduced and used to elaborate the design and development of two characterization schemes, which is the fundamental part of this thesis. The first, used to quantify the concentration of a nanoparticle solution embedded in a turbid media, has employed a short pulsed Nd:YAG laser source operating at 532 nm. The second, used for spectroscopic characterization of gold nanoparticles in a scattering media, has employed a short pulsed OPO pumped with an Nd:YAG operating over the wavelength range from 450 to 650 nm for spherical particles and 410 nm to 1000 nm for the rod shaped gold particles. The wavelength emission of the OPO and the acquisition of both optical and acoustic signals have been completely controlled using a specifically designed software program.

To verify the feasibility of the optoacoustic quantification and spectroscopic measurement techniques, a collimated optical transmission scheme has been set up in parallel, and under the same experimental conditions. This additional measurement procedure has allowed a comparative analysis of the results obtained. The spectroscopic analysis has also been compared to measurements from a standard commercial spectrophotometer, which is regarded as the gold standard for spectral characterization.

The experimental results obtained from the quantification scheme have been presented in Chapter 5. Results from preliminary trials on different concentrations of a known optical absorber have been presented. An absorption coefficient of 3.67 ± 0.3 cm^{-1} (per % ink concentration) has been obtained using the optoacoustic technique which is in very close agreement with the absorption coefficient of 3.65 ± 0.2 cm^{-1} (per % ink concentration) obtained from the reference measurement scheme. This preliminary trial has confirmed the feasibility of the optoacoustic technique, and has motivated further experimental trials to determine the absorption coefficient of a 20 ± 2 nm diameter spherical gold nanoparticle solution. This has produced results of 17.18 ± 0.8 cm^{-1} and 17.35 ± 0.5 cm^{-1} (per normalized SGNP concentration) for the optoacoustic and reference measurement, respectively, again very close agreement is shown. Finally, and as part of the objectives of this thesis, the optical absorption of a 15 ± 2 nm diameter SGNP with concentrations ranging from 4.2 nM to 42 nM embedded in different concentrations of a highly scattering media, have been measured. The results obtained from the optoacoustic and collimated optical transmission techniques were 1.96 cm^{-1} and 1.98 cm^{-1} per nM, respectively. The reduced scattering coefficient of the turbid medium has also been determined experimentally as 3.19 cm^{-1} and 3.16 cm^{-1} per % concentration using the optoacoustic and reference scheme, respectively. The results obtained from the quantification system have been the subject of a recent publication.

The results from the optoacoustic spectroscopic scheme have been presented in Chapter 6 for both the spherical and nanorod particle solutions. The spectroscopic profile associated with the geometrical structure of each particle has been observed using the optoacoustic technique and has been confirmed with those obtained from the reference measurement scheme, and from an offline standard spectrophotometer. A quantitative spectroscopic analysis using a calibrated detector has determined the absorption coefficient of the longitudinal surface plasmon at 844 nm to be 13.4 cm^{-1}. Good agreement is observed between this value and the 13.7 cm^{-1} obtained from the collimated optical transmission scheme at the same wavelength and is also in good agreement with the absorption coefficient of 14 cm^{-1} provided by the commercial spectrophotometer. The feasibility of the optoacoustic technique for quantitative spectroscopic analysis of absorbers embedded within a scattering media has been confirmed. The experimental results obtained from the spectroscopic analysis on the

spherical gold nanoparticles and gold nanorods have been the subject of two recent publications.

Finally, the experimental work presented in this thesis has opened up new lines of investigation on the quantitative and spectroscopic analysis of absorbers embedded within turbid media dominated by scattering. First, the development of novel nanostructures based on carbon nanotubes are finding applications as targeted contrast agents in optoacoustics, MRI Imaging, cell tracking, and for monitoring the progress of tissue formation. By extending the wavelength range of the optoacoustic spectroscopy setup described in this thesis, a quantitative analysis of the behavior of such particles can be determined for both the near and far-infrared. Also, and just as significantly, the combination of the quantitative spectroscopic analysis with optoacoustic imaging techniques would provide vital information on the evolution of chromophores embedded in soft tissue. Finally, recent *in-vivo* trials using enhanced absorption of continuous wave laser power by gold nanoparticles for photothermal ablation of cancerous formations tumors have prompted the requirement for monitoring of changes in nanoparticle concentration and spectral profile. This analysis will help understand and quantify the photothermal energy conversion in tumor tissues.

Appendix A

Optical Properties of Biological Tissues and Fluids

A.1 Introduction

A discussion on the attenuation of optical energy has been presented in Chapter 2 of this thesis. It has been shown optical attenuation is principally due to the absorption and scattering of light. In this Appendix A a list of the wavelength dependent optical properties are presented for tissues commonly found in biomedical imaging and diagnostics within the therapeutic window, 300 nm to 1200 nm (see Chapter 2 Section 2.2.4).

A.2 Optical Absorption in Biological Materials

The optical absorption is the way by which the energy of a photon is taken up by matter. A full description of this process has been presented in Chapter 2 Section 2.2.1. The absorption of a medium is characterized by both the absorption cross section, σ_{abs} (cm^2) and the absorption coefficient, μ_{abs} (cm^{-1}). Where the relation between these two parameters is given by:

$$\mu_{abs} = N\sigma_{abs} \tag{A.2.1}$$

Where N (cm^{-3}) is the number density of absorbers. Using Beer's law the intensity, I, at any distance, d, in a pure absorber can be obtained with knowledge of the initial intensity, I_0, and the absorption coefficient as:

$$I(d) = I_0 \exp(-\mu_{abs} d) \tag{A.2.2}$$

A.2.1 Skin Optical Absorption Properties

The skin is the largest organ in the human body, and serves to protect underlying muscles, bones, ligaments and internal organs, as well as providing insulation and temperature regulation forming an anatomical barrier to pathogens. Skin is composed of three primary layers, see FigureA.1. These are: *Stratum Corneum*, clear or translucent avascular layer, with a stratified structure. It is the uppermost layer of the skin and is composed of 10 – 20 layers of dead cells which have no nuclei, these are known as corneocytes and are embedded in a liquid matrix. *Epidermis*, also an avascular layer which has a depth in the order of 27 - 150 μm. *Dermis*, is 0.6 - 3 mm thick and can be divided into two different layers, the papillary dermis and the reticular dermis. These layers are composed of dense, irregular connective tissue with nerves and blood vessels

(smaller ones in the papillary and larger ones in the reticular). The dermis layer contains extra-cellular structural proteins such as collagen and elastin.

In TableA.1 the wavelength dependent absorption coefficient for the different skin layers is presented [A.1-A.2].

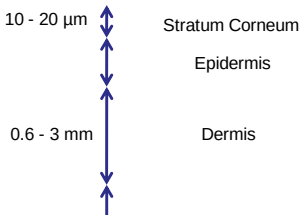

FigureA.1 Skin tissue structure

Description	λ (nm)	μ_{abs} (cm^{-1})	Description	λ (nm)	μ_{abs} (cm^{-1})
Stratum Corneum	250	1150	Dermis	585	3
Stratum Corneum	308	608	Dermis	800	2.3
Stratum Corneum	337	330	Caucasian male	500	5.1
Stratum Corneum	400	230	Caucasian male	810	0.26
Epidermis	250	1000	Caucasian female	500	5.2
Epidermis	308	300	Caucasian female	810	0.97
Epidermis	585	36	Hispanic male	500	3.8
Epidermis	800	40	Hispanic male	810	0.87
Dermis	250	35	Forearm: fat	633	0.026
Dermis	308	12	Forearm: muscle	633	0.96

TableA.1 Absorption coefficient for skin layers [A.1-A.2]

A.2.2 Blood Optical Absorption

Blood is the principle body fluid that delivers nutrients and oxygen to the cells within the human body. Blood is composed of blood cells that are suspended in a liquid known as blood plasma. This contains dissolved proteins, glucose, mineral ions, hormones, carbon dioxide, platelets and blood cells. The majority of blood cells are known as red blood cells and white blood cells. The red blood cells contain haemoglobin, a protein containing iron, and facilitate the transport of oxygen. Oxygenated haemoglobin (HbO_2) transports the Oxygen received in the lungs to the rest of the body's tissues. The deoxygenated haemoglobin (Hb) returns to the heart where it is pumped to the lungs to be re-oxygenated. In Chapter 2 the importance of blood diagnostics has been indicated, and is shown to be an important chormophore within the therapeutic window, where both HbO_2 and Hb present distinct spectral profiles.

The concentration of oxygen in haemoglobin is used for cancer diagnostics. By using two different wavelengths it is possible to calculate the concentration, C, of the oxygenated haemoglobin, c_{HbO_2}, and the deoxygenated haemoglobin, c_{Hb}, *in vivo* from the absorption coefficients at each wavelength, i.e:

$$\mu_{abs}(\lambda_1) = \varepsilon_{HbO_2}(\lambda_1) c_{HbO_2} + \varepsilon_{Hb}(\lambda_1) c_{Hb} + \varepsilon_{water}(\lambda_1) c_{water} \tag{A.2.3}$$

$$\mu_{abs}(\lambda_2) = \varepsilon_{HbO_2}(\lambda_2) c_{HbO_2} + \varepsilon_{Hb}(\lambda_2) c_{Hb} + \varepsilon_{water}(\lambda_2) c_{water} \tag{A.2.4}$$

Where c_{water} is the water concentration and the wavelength dependent molar extinction coefficients for the oxygenated blood, deoxygenated blood and water are given by ε_{HbO_2}, ε_{Hb} and ε_{water}, respectively. Within the therapeutic window the impact of water absorption may be neglected. A measure of the percentage of haemoglobin saturated with oxygen is given by the oxygen saturation, SO_2, i.e:

$$SO_2 = \frac{c_{HbO_2}}{c_{HbO_2} + c_{Hb}} \tag{A.2.5}$$

Typical values for the absorption coefficient of blood in its different states of oxygenation are presented in Table A.2 [A.1-A.2].

Tissue	Description	λ (nm)	μ_{abs} (cm^{-1})	Tissue	Description	λ (nm)	μ_{abs} (cm^{-1})
Blood	Oxygenated	665	1.3	Blood	Oxygenated > 98%	865	7.2
Blood	Oxygenated	685	2.65	Blood	Oxygenated > 98%	910	8.9
Blood	Oxygenated	960	2.84	Blood	Oxygenated > 98%	965	9.3
Blood	Deoxygenated	665	4.87	Blood	Oxygenated > 98%	1010	8.3
Blood	Deoxygenated	960	1.68	Blood	Flowing Blood 24.5ºC	633	2.9 – 3.5
Blood	Oxygenated > 98%	710	4	Blood	Flowing Blood 24.5ºC – 42ºC	633	3.0 – 4.0
Blood	Oxygenated > 98%	765	5.3	Blood	Flowing Blood 47ºC	633	4.5
Blood	Oxygenated > 98%	810	6.5	Blood	Flowing Blood 54.3ºC	633	6.3

Table A.2 Blood absorption coefficients at different wavelengths [A.1-A.2]

A.2.3 Breast Tissue Absorption

The female breast is made up mainly of *lobules*, (milk producing glands), *ducts* (tubes that transport milk) and *stroma* (fatty and connective tissue). The majority of breast cancers begin in the cells that line the ducts, referred to as ductal cancer. Infiltrating ductal carcinoma accounts for the majority of breast cancer cases. The role of optoacoustics for detecting cancer in breast tissue has received much attention over the past decade [A.3-A.5]. The optical absorption properties of the different constituents of the female breast are presented in TableA.3 for *in-vitro* measurements [A.1] and in TableA.4 for *in-vivo* measurements.

Description	λ (nm)	μ_{abs} (cm^{-1})	Description	λ (nm)	μ_{abs} (cm^{-1})
Fatty normal	749	0.18	Fatty tissue	540	2.27
Fatty normal	789	0.08	Fatty tissue	700	0.7
Fatty normal	836	0.11	Fatty tissue	900	0.75
Fibrous normal	749	0.13	Fibrocystic tissue	540	1.64
Fibrous normal	836	0.05	Fibrocystic tissue	900	0.27
Infiltrating carcinoma	749	0.04	Fibroadenoma	540	4.38
Infiltrating carcinoma	836	0.1	Fibroadenoma	700	0.52
Mucinous carcinoma	749	0.26	Carcinoma	540	3.07
Ductal carcinoma	749	0.076	Carcinoma	900	0.5
Ductal carcinoma	836	0.039	Healthy tissue adjacent to carcinoma	580	2.6
Glandular tissue	540	3.58	Healthy tissue adjacent to carcinoma	850	0.3
Glandular tissue	700	0.47	Fatty tissue	625	0.06
Glandular tissue	900	0.62	Benign tumor	625	0.33

TableA.3 *in vitro* female breast tissue optical absorption [A.1]

Tissue	λ (nm)	μ_{abs} (cm^{-1})	Notes	Ref.
Normal (30 Japanese women averaged for all ages)	753	0.046	Time-domain technique	[A.6]
Normal (6 subjects, 26 – 43 years old)	800	0.017-0.045	Time-domain technique	[A.7]
Normal (6 patients)	580	0.7	Measurements of transmission	[A.8]
Normal (6 patients)	780	0.23	Measurements of transmission	[A.8]
Normal (6 patients)	850	0.27	Measurements of transmission	[A.8]
Breast Cancer (5 patients)	630	0.305	Relapsed cancer	[A.9]

TableA.4 *in-vivo* absorption coefficients for female breast tissues and tissue components

A.3 Optical Scattering in Biological Materials

The optical scattering in biological tissues occurs as a results refractive index mismatches at microscopic boundaries of different biological tissues and fluids. A full description of the scattering process has been given in Chapter 2 Section 2.2.2. Similarly to the absorption, the scattering characteristics of a medium are characterized by both the scattering cross section, σ_{sca} (cm^2) and the absorption coefficient, μ_{sca} (cm^{-1}). Where the relation between these two parameters is given by:

$$\mu_{sca} = N\sigma_{sca} \tag{A.3.1}$$

Where N (cm^{-3}) is the number density of scatterers. Using Beer's law the intensity, I, at any distance, d, in a pure scattering homogeneous medium can be obtained with knowledge of the initial intensity, I_0, and the absorption coefficient as:

$$I(d) = I_0 \exp(-\mu_{sca} d) \tag{A.3.2}$$

The medium described by equation (A.3.2) assumes that the scattering is isotropic. However, the electromagnetic waves from the optical source, such as a laser, are directionally dependent and decrease the scattering coefficient. It has been seen that the reduced scattering coefficient is described by the g parameter which is a measure of the mean cosine of the scattering angle θ as:

$$g = \langle \cos(\theta) \rangle \tag{A.3.3}$$

The reduced scattering coefficient, $\mu_{sca}^{'}$, is described by:

$$\mu_{sca}^{'} = (1-g)\mu_{sca} \tag{A.3.4}$$

In this section of Appendix A details regarding the scattering coefficient and g parameter will be provided.

A.3.1 Skin Optical Scattering Properties

When dealing with non-invasive optical procedures the optical properties of the skin must be taken into consideration. The light must pass through the three different layers, see Section A.2.1. In vitro measurements of the stratum corneum have shown that the scattering coefficient, μ_{sca}, is 2000 cm^{-1} at 400 nm and has a typical anisotropy factor, g, of 0.9 scattering in this layer is strongly dependent on the age and hydration of the tissue [A.10]. Mie scattering dominates in the epidermis and is due to cell organelles, reports have been presented for μ_{sca} in the order of 2000 cm^{-1} at 250 nm which decreases for longer wavelengths to 420 cm^{-1} at 800 nm, the g parameter being 0.69 and 0.85, respectively [A.10]. The scattering of collagen fibers within the dermis are of major importance when calculating the penetration depth. These are responsible for Mie scattering, while smaller scale collagen fibers and other micro-structures are responsible for Rayleigh scattering [A.11]. In TableA.5 the wavelength dependent scattering coefficient and anisotropy factor *g* for the different skin layers are presented [A.1-A.2].

Description	**λ (nm)**	μ_{sca} **(cm^{-1})**	μ'_{sca} **(cm^{-1})**	**g**
Stratum Corneum	250	2600	-	0.9
Stratum Corneum	308	2400	-	0.9
Stratum Corneum	337	2300	-	0.9
Stratum Corneum	400	2000	-	0.9
Epidermis	250	2000	-	0.69
Epidermis	308	1400	-	0.71
Epidermis	585	470	-	0.79
Epidermis	800	420	-	0.85
Dermis	250	833	-	0.69
Dermis	308	583	-	0.71
Dermis	585	196	-	0.79
Dermis	800	175	-	0.85

TableA.5 scattering coefficient and *g* parameter for skin layers [A.1-A.2]

A.3.2 Blood Optical Scattering Properties

In blood the strongest scatterers are caused by the disc shape of the red blood cells, known as erythrocytes (see FigureA.2). This disc structure is 7 to 9 µm in diameter and ranges from 100 nm to 2 µm thick. In blood the scattering depends on the volume fraction of red cells, known as *hemacrit*, and its degree of agglomeration. Typical values for both the scattering coefficient and *g* parameter of blood samples in different states of oxygenation are presented in Table A.6 [A.1-A.2].

FigureA.2 Erythrocytes and their typical dimensions

Description	λ (nm)	μ_{sca} (cm^{-1})	μ'_{sca} (cm^{-1})	g	Description	λ (nm)	μ_{sca} (cm^{-1})	μ'_{sca} (cm^{-1})	g
Oxygenated	665	1246	6.11	0.995	Oxygenated > 98%	865	649	-	0.99
Oxygenated	685	1413	14.13	0.99	Oxygenated > 98%	910	649	-	0.992
Oxygenated	960	505	3.84	0.992	Oxygenated > 98%	965	650	-	0.991
Deoxygenated	665	509	2.49	0.995	Oxygenated > 98%	1010	645	-	0.992
Deoxygenated	960	668	5.08	0.992	Flowing Blood 24.5ºC	633	-	18-20	-
Oxygenated > 98%	710	737	-	0.986	Flowing Blood 24.5ºC – 42ºC	633	-	18-17	-
Oxygenated > 98%	765	725	-	0.991	Flowing Blood 47ºC	633	-	21	-
Oxygenated > 98%	810	690	-	0.989	Flowing Blood 54.3ºC	633	-	17	-

Table A.6 Blood scattering coefficient and g parameter at different wavelengths

A.3.3 Breast Tissue Scattering

The optical scattering in breast tissue occurs as a consequence of the refractive index changes which are influenced by the cellular and extracellular matrix density. In the following Table A.7 *in-vitro* measurements for different healthy and diseased constituents of the female breast are presented. In Table A.8 *in-vivo* results for both normal and diseased breast tissue are presented. Comparing the attenuation of light due to scattering to that caused by absorption (see TableA.3 and TableA.4) it may be seen that the scattering component is dominant. The high level of scattering present reduces the penetration depth and the optical contrast in optical based systems that rely on the absorption of light.

Description	**λ (nm)**	μ_{sca} **(cm^{-1})**	μ'_{sca} **(cm^{-1})**	**Description**	**λ (nm)**	μ_{sca} **(cm^{-1})**	μ'_{sca} **(cm^{-1})**
Fatty normal	749	8.48	-	Glandular tissue	540	-	24.4
Fatty Normal	836	7.27	-	Glandular Tissue	900	-	9.9
Fibrous Normal	749	9.75	-	Fatty Tissue	540	-	10.3
Fibrous Normal	836	8.1	-	Fatty Tissue	900	-	7.9
Infiltrating carcinoma	749	10.91	-	Fibrocystic tissue	540	-	21.70
Infiltrating carcinoma	836	9.1	-	Fibrocystic tissue	900	-	9.5
Mucinous carcinoma	749	-	6.15	Fibroadenoma	540	-	11.1
Mucinous carcinoma	836	-	4.78	Fibroadenoma	900	-	5.3
Ductal Carcinoma	749	-	13.1	Carcinoma	540	-	19
Ductal Carcinoma	836	-	10.46	Carcinoma	900	-	8.9

Table A.7 *in vitro* female breast tissue optical absorption

Description	λ (nm)	$\mu_{sca}^{'}$ (cm^{-1})	Uncertainty (cm^{-1})	Notes	Ref.
Normal (30 Japanese women averaged for all ages)	753	8.9	1.3	Time-domain technique	[A.6]
Normal (6 subjects, 26 – 43 years old)	800	7.2 – 13.5	-	Time-domain technique	[A.7]
Breast Cancer (5 patients)	630	9.41	7.35	Relapsed cancer	[A.9]

Table A.8 *in-vivo* absorption coefficients for female breast tissues and tissue components

Appendix B

Efficient Combination of Multiple High Power Semiconductor Laser Sources for Optoacoustic Signal Generation

B.1 Introduction

Currently the most popular laser sources for optoacoustic signal generation are based on the use of Nd:YAG solid state lasers. This is because such laser sources can produce short optical pulses with high amounts of energy ($\sim mJ$). This is required for penetration of high scattering media, such as biological tissue, and for efficient conversion of the optical energy to acoustic transients. During the design steps of the optoacoustic schemes presented in this thesis, a review of the use of high power semiconductor lasers has also been performed [B.1].

The high power semiconductor pertains many advantages when compared to solid state laser sources, such as the Nd:YAG. Semiconductor laser sources are small, robust, lightweight and cost effective and are compatible with portable compact systems. Semiconductor lasers are commercially available in a wide range of operating wavelengths, this particular property is of interest for optoacoustic spectroscopy systems, providing information on tissue oxygenation, lipid content, and the concentration of water [B.2]. Another clear advantage of the diode laser source is the controlled variability of the pulse repetition rate (PRR) and pulse duration. In high power devices user controlled PRR ranging from Hz to 100's of kHz can be achieved, compared to 10's of Hz in Q-switched systems. Another main advantage is their compatibility with optical fiber technology, allowing the possibility for optoacoustic probes.

The main drawback to using semiconductor laser devices is their limited pulse energy. As a result of this shortcoming, current biomedical applications using diode lasers are limited to shallow tissue applications, such as glucose measurement in blood vessels [B.3]. Other authors have stated that this problem can be overcome by joining several semiconductor laser sources [B.4-B.5]; however no results or indications to this process have been presented.

In this Appendix B a description of an experimental scheme which efficiently combines the optical power from two high power diode laser sources is presented. The experimental results obtained from this technique will also be presented here.

B.2 Optoacoustic Signal Generation Scheme

B.2.1 Laser Diode Optoacoustic Signal Generation Scheme

A block diagram of the diode laser based optoacoustic signal scheme is presented in FigureB.1. and a photograph of the system is presented in Figure B.2. The optical source is composed of two combined high power commercial semiconductor lasers with similar characteristics (TPGAU3S09 from Perkin-Elmer). These lasers operate at a central wavelength of 905nm, and have a maximum peak power of between 210 and 224 Watts. In order to achieve efficient coupling of the laser radiation it is important that the laser pulses generated from the pulse generator and PRR source occur simultaneously. This has been accomplished by designing a pulse generator with two symmetric outputs that are connected to the laser driver circuitry (laser driver PCO-7120 from DEI, directed energy incorporated, giving 50 A peak current).

The acoustic signals generated are detected using a piezoelectric ceramic transducer with a resonant frequency of 1MHz (V303 from Panametrics). The signals from the transducer are amplified before being captured by the measurement apparatus (40dB preamplifier, 5678 from Panametrics).

FigureB.1 Laser diode based optoacoustic signal generation scheme

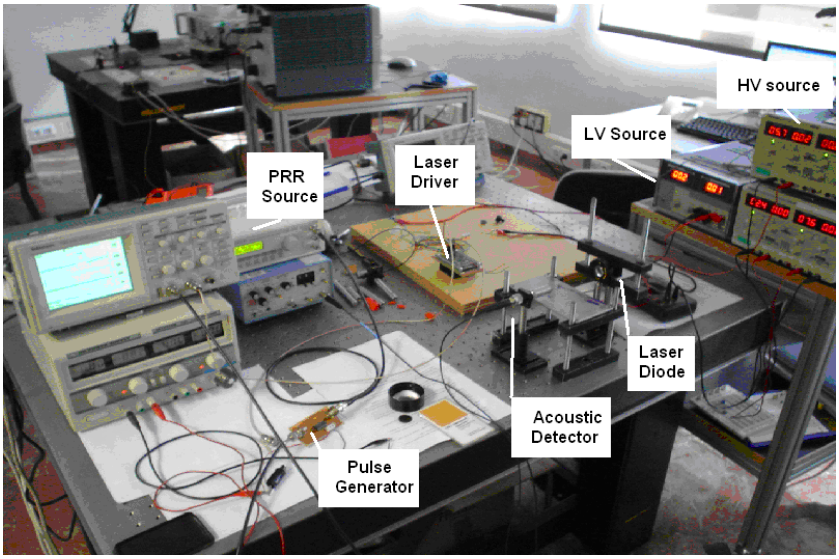

Figure B.2 Semiconductor laser optoacoustic signal generation scheme

B.2.2 Diode Laser Combination

A graphical description of the combination of both semiconductor sources is presented in Figure B.3 and a photograph in Figure B.4. The combination has been carried out using standard optical techniques. The laser sources are first collimated using a short focal length (2 mm) aspheric lens with an anti-reflection (AR) coating close to the central operating wavelength of the laser. The collimated laser beam is then focused using another aspheric lens with a larger focal distance (15 cm). The laser spot size was measured to be 3mm^2. Both laser sources are focused at the same point.

Laser

Figure B.3 Combination of two semiconductor laser sources using standard optical techniques

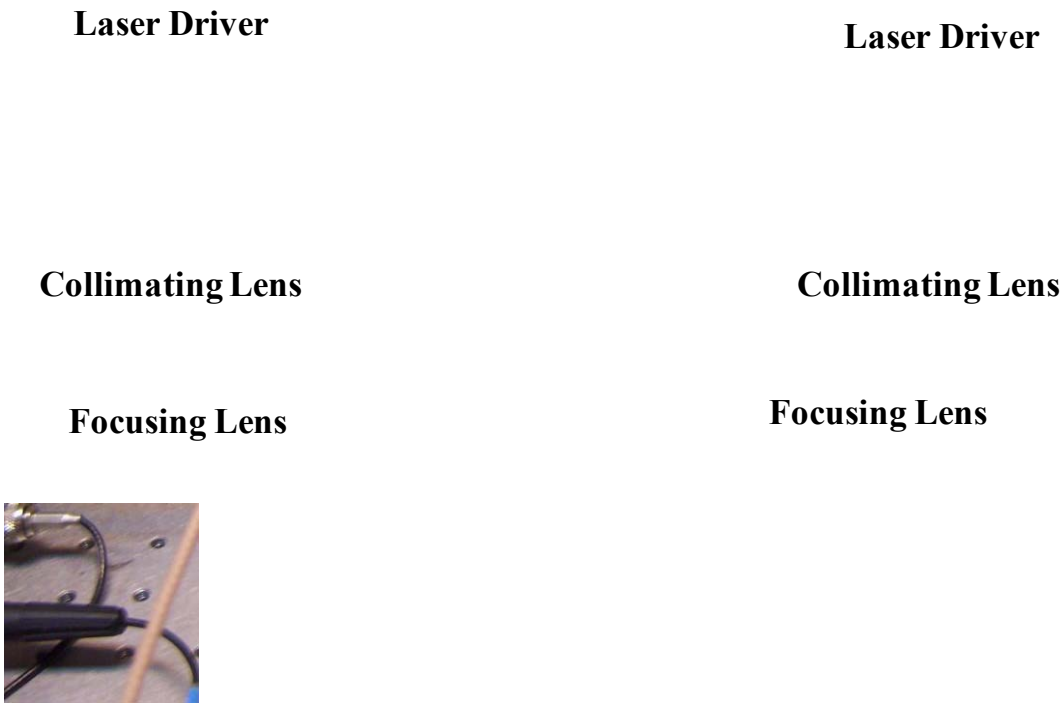

Figure B.4 Combination of two semiconductor laser sources using standard optical techniques

B.2.3 Target Material

To test the feasibility of the combined semiconductor laser scheme a pure ink absorbing solution has been used (Edding 1200 ink). This absorber has been injected into a transparent ballistic gel medium Figure B.5, commonly used in the fabrication of optical phantoms. The acoustic transducer is coupled to this gel medium containing the absorber using an impedance matching gel (i.e. between the sample and the detector).

Figure B.5 Ballistic gel containing ink absorber

B.3 Experimental Results of Combined Laser Diode Scheme

The experimental results, presented here, have been carried out to evaluate the efficiency of the combined laser source in the proposed signal generation scheme. This includes a comparative analysis of the optoacoustic signals generated from each laser A and B (see Figure B.3) operating independently to those signals obtained from the combined diode laser diodes.

To ensure a direct comparison, the optical pulses from both sources have the same average and peak power. The average power from each diode laser device has been measure separately to be 5 mW, the optical pulse repetition rate and pulsewidth were set to 2 KHz and 180 ns, respectively. This corresponds to a duty cycle of 0.036 %, peak optical power of 13.8 W, and energy 2.5 μJ. The combined laser power has been measured to be 10 mW, producing a pulse energy of 5 μJ. These preliminary measurements have confirmed the efficiency of the experimental scheme.

The optoacoustic signals generated from the thermal expansion of the ink solution within the gel medium are presented in the following FigureB.6. The initial peak to peak voltage of the acoustic signal was measured to be 42 mV from laser A and 40 mV from laser B (see FigureB.6 (left)). The difference in these signals can be explained by inhomogeneities in the gel causing differences in the attenuation to the optical propagation from each laser. The amplitude of the acoustic transients generated by the combined diode laser scheme has produced an acoustic signal amplitude of 82 mV

(FigureB. (right)). From this result the efficiency of combining laser sources is observed. Another interesting feature of the acoustic signals produced is that the waveform of the signal maintains constant for each measurement. It has been explained in Chapter 2 of this thesis that the temporal profile of the acoustic transient generated is dependent on the shape of the optical absorber.

FigureB.6 (Left) optoacoustic signals received from laser sources independently (A and B separately)(right) optoacoustic signal generated from combined laser sources (A and B together).

Appendix C

Mie Coefficients

C.1 Introduction

In this appendix a more detailed review of the Mie Coefficients used in the numerical analysis presented in Chapter 3 Section 3.4 to calculate both the absorption and scattering properties of homogenous gold spherical nanoparticles are presented.

C.2 Mie Coefficients

The key parameters for the calculation of the amplitudes of the scattered and absorbed fields are the Mie coefficients a_n and b_n. These have been presented in Chapter 3 Section 3.4 and are given by:

$$a_n = \frac{m^2 j_n(mx)\left[xj_n(x)\right]' - \mu_1 j_n(x)\left[mxj_n(mx)\right]'}{m^2 j_n(mx)\left[xh_n^{(1)}(x)\right]' - \mu_1 h_n^{(1)}(x)\left[mxj_n(mx)\right]'} \qquad \text{(C.2.1)}$$

$$b_n = \frac{\mu_1 j_n(x)\left[xj_n(x)\right]' - j_n(x)\left[mxj_n(mx)\right]'}{\mu_1 j_n(mx)\left[xh_n^{(1)}(x)\right]' - h_n^{(1)}(x)\left[mxj_n(mx)\right]'} \qquad \text{(C.2.2)}$$

Where m is the relative refractive index between the homogeneous sphere and the surrounding medium. The term x is the size parameter given by:

$$x = \frac{2\pi r}{\lambda} \qquad \text{(C.2.3),}$$

where λ is the wavelength of the incoming light and r is the radius of the particle. The term μ_1 represents the ratio of the magnetic permeability of the sphere to the magnetic permeability of the surrounding medium. The magnetic permeability of both water and gold is 1.256 x 10^{-6} (H/m) thus $\mu_1 = 1$.

The functions $j_n(z)$ and $h_n^{(1)}(z) = j_n(z) + iy_n(z)$ are spherical Bessel functions of the order n ($n = 1, 2, 3, \ldots$) and of the given argument $z = x$ or mx, respectively. The derivatives follow from the spherical Bessel functions themselves, namely:

$$\left[zj_n(z)\right]' = zj_{n-1}(z) - nj_n(z)$$
$$\left[zh_n^{(1)}(z)\right]' = zh_{n-1}^{(1)}(z) - nh_n^{(1)}(z) \tag{C.2.4}$$

The relationship between the spherical Bessel functions and the ordinary Bessel functions are given by:

$$j_n(z) = \sqrt{\frac{\pi}{2z}} J_{n+1/2}(z)$$
$$y_n(z) = \sqrt{\frac{\pi}{2z}} Y_{n+1/2}(z) \tag{C.2.5}$$

Here, *J* and *Y* are Bessel functions of the first and second kind. For *n=0* and *1* the spherical Bessel functions are given by:

$$j_0(z) = \sin\frac{z}{z}$$
$$j_1(z) = \sin\frac{z}{z^2} - \cos\frac{z}{z}$$
$$y_0(z) = -\cos\frac{z}{z} \tag{C.2.6}$$
$$y_1(z) = -\cos\frac{z}{z^2} - \sin\frac{z}{z}$$

Where the recurrence formula is: enormous

$$f_{n-1}(z) + f_{n+1}(z) = \frac{2n+1}{z} f_n(z) \tag{C.2.7}$$

The number of terms n_{max} used in the simulation presented in this thesis to calculate the attenuation coefficients has been proposed by Bohren and Huffman as [C.1]:

$$n_{\max} = x + 4x^{1/3} + 2 \tag{C.2.8}$$

Appendix D

Spherical Gold Nanoparticle Synthesis

D.1 Spherical Gold Nanoparticle Synthesis

The protocol for the synthesis of monodisperse spherical gold nanoparticles characterized in this dissertation was adapted using the Turkevich Method [D.1 - D.2]. This method is commonly used to synthesize spherical gold nanoparticles suspended in water. The procedure involves the reduction of a solution of hydrogen tetrachloroaurate acid $HAuCl_4$ (commonly referred to as gold salt) using trisodium citrate $Na_3C_6H_5O_7$ (referred to as sodium citrate). This causes the Au^{3+} ions to be reduced to highly stable neutral gold atoms (see Figure B.1). The colloidal gold is formed as the citrate ions prevent the gold particles from combining.

$$6\,Au^{3+} + C_6H_5O_7^{3-} + 15\,OH^- \longrightarrow 6\,Au + 6\,CO_2 + 10\,H_2O$$

Figure B.1

The volume of the citrate solution is used to control the diameter of the gold spheres during the synthesis where exact volumes of both the gold salt solution and reducing agent are required. An example of the volume of a 1 % (wt) Na_3-citrate solution required for the synthesis of different spherical gold nanoparticle diameters is presented in Table D.1 and presented graphically in FigureB.1 [20].

Volume of 1 % (wt)Na_3-Citrate	**Gold Sphere Diameter**
1.00 ml	16 nm
0.75 ml	24.5 nm
0.5 ml	41.0 nm
0.3 ml	71.5 nm
0.21 ml	97.5 nm
0.16 ml	147 nm

Table D.1 Data for the volumes of a 1 % (wt) Na_3-citrate solution required for the controlled nucleation and regulation of gold nanoparticle sizes in a distilled water suspension liquid. Note that the quantity of the 0.01 % (wt) $HAuCl_4$ solution is 50ml in all cases [20].

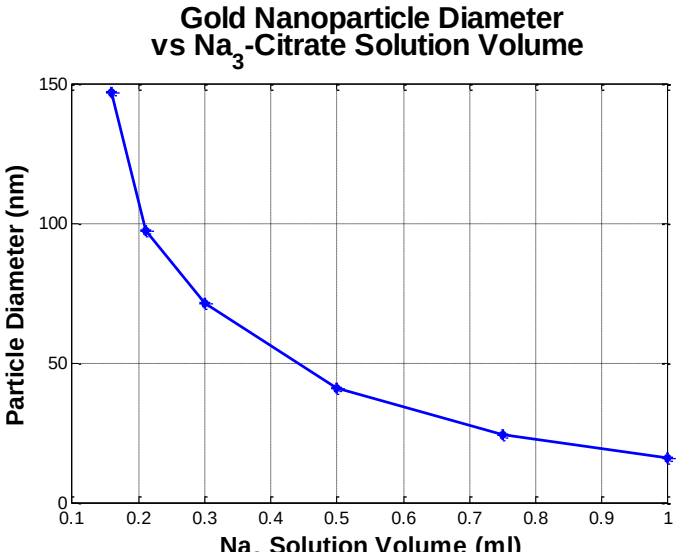

FigureB.2 Graphical representation of the data presented in Table D.1 showing the dependence the spherical nanoparticle diameter has on the volume of a 1 % (wt) Na_3-citrate solution. Note that the quantity of the gold salt was 0.01 % (wt) the $HAuCl_4$ solution is 50ml in all cases [20].

D.2 Synthesis Protocol

The protocol for the synthesis of both 15 nm and 20 nm monodisperse spherical gold nanoparticles which were characterized in this dissertation (in Chapters 5 and 6) was adapted using the Turkevich Method where the volumes of both the gold salt and citrate solution were calculated from the data presented in [20]:

- A 200 ml aqueous solution of 0.01% (wt) of $HAuCl_4$ was prepared using triple distilled water.
- This solution was brought to the boil and stirred continually to ensure homogeneity, using a hotplate and a magnetic stirrer.
- As soon as boiling commenced, a 1 % (wt) of Na_3-citrate solution was added, where the volume depends on the size of the nanoparticle required. The reaction takes place when the solution is boiling as the citrate does not significantly reduce the $HAuCl_4$ at room temperature.
- Heating and stirring of the resulting solution is continued until color change is evident.
- The observed color change to deep red was noted after approximately 6 minutes (see Figure 0.A).

- The solution was then removed from the heating element and stirred continually until it cooled to room temperature.
- Finally the solution was filtered (0.22 μm pores) to remove any large residual particle.
- The spherical nanoparticle solution is stored at 4ºC (see Figure 0.A)

Figure 0.A Spherical gold nanoparticle solution synthesized using the Turkevich method.

D.3 Preliminary Characterization

To verify the quality of the controlled synthesis of the nanoparticle solution, Transmission Electron Microscopy (TEM) has been used on a diluted sample of the 15 nm diameter spherical gold nanoparticles (see Figure 0.B) and on the 20 nm particles (see Figure 0.C). The size of both nanoparticle solutions was calculated from the TEM images using the image analysis software ImageJ (Freeware developed at the *National Institute of Health*). Both the 15 nm and 20 nm particles have an average size variation of ±2 nm.

Figure 0.B Transmission Electron Microscopy (TEM) of 15 nm spherical nanoparticles prepared using the Turkevich method.

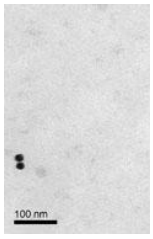

Figure 0.C Transmission Electron Microscopy (TEM) of 20 nm spherical nanoparticles prepared using the Turkevich method.

Appendix E

Optoacoustic Characterization Schemes

E.1 Introduction

Within this Appendix E information regarding recent attempts at chromophore characterization using the optoacoustic technique performed by other authors will be presented. The concepts used and the experimental schemes will be discussed for each case.

E.2 Quantitative Optoacoustic Spectroscopic Measurement Schemes[E.1]

Recent work at University College London (UCL) in the Depatment of Medical Physics and Bioengineering headed by Paul C. Beard, Ph.D. has concentrated on the quantitative analysis of chromophores in biological phantoms. The experimental scheme shown in Figure E.1 has been designed to determine tissue chromophore concentrations non-invasively using optoacoustic spectroscopy [E.1]. This scheme is applicable to measurements of the concentration of oxyhaemoglobin (HbO_2) and deoxyhaemoglobin (Hb) for oxygensaturation measurements (SO_2). The authors also state that this system can be used to quantify the local accumulation of optical contrast agents.

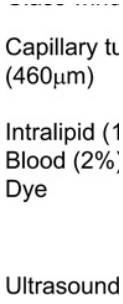

Figure E.1 Experimental setup for measuring optoacoustic spectroscopic signals [21]

The scattering of the soft tissue has been simulated using an intralipid solution (1.5 % concentration, $\mu_{sca}^{'} = 15\,\mathrm{cm}^{-1}$ and $\mu_{abs} = 0.5\,\mathrm{cm}^{-1}$ at 975 nm). This scattering liquid surrounds three different polymethyl methacrylate tubes (460 μm in diameter with a 75 μm tube wall thickness) that have been immersed at depths of 4.4, 6.7 and 8.8 mm. The absorbing chromophore in the experimental trials carried out using this scheme was a continuously circulating saline suspension of red blood cells through the tubes. The blood SO_2 within the tubes has been varied from 2 % to 100 % using a membrane oxygenator and gas mixer.

The optical source used to generate the optoacoustic signals was a Optical Parametric Oscillator (OPO) operating over the wavelength range from 740 nm to 1040 nm in wavelength steps of 10 nm (scan time 20 minutes approx.). Part of the light incident on the soft tissue phantom was sent to a spectrophotometer to measure the wavelength of the light emitted by the OPO and part of the light was directed towards an integrating sphere containing a wavelength calibrated photodiode to normalize the power.

The acoustic transients generated from the optical absorption have been measured using an interferometric Fabry-Perot polymer film broadband detector (15 MHz) [E.2]. The analysis of the measured acoustic transients has been performed by taking the amplitude corresponding to the signal generated by each of the tubes at each wavelength step. The quantification of the chromophore concentration has been performed by fitting the spectral profile obtained to results from a theoretical model.

E.3 Optoacoustic Quantitative Spectroscopy of chromophore phantoms [D.3]

More recent attempts by the same group at UCL to determine the optical properties of chromophore phantoms has involved a similar scheme to that presented in Figure E.1, shown in Figure E.2. The pure absorbers under examination have been inorganic chromophores, such as cyanine-based near infrared dyes. The optical source used, tunable OPO over the wavelength range from 740 nm to 1040 nm in steps of 10 nm, and wideband acoustic Fabry Perot transducer, are the same as those described in the previous Section E.2.

The analysis of the optoacoustic signals generated has been based on the signal amplitude and the exponential slope, see Figure , these measurement concepts have

been described in Chapter 4 Section 4.2. A comparative analysis with results from an offline spectrophotometer (Lambda 25, Perkin-Elemer) have verified the feasibility of the technique.

Figure E.2 Experimental setup for the measurement of optoacoustic signals generated in nonscattering liquid absorbers as a function of wavelength [E.3].

Figure E.3 optoacoustic signal analysis based on the amplitude of the acoustic signal and the exponential increase of the signal.

E.4 In-vivo Noninvasive Optoacoustic Spectroscopic Mapping of Gold Nanorod Contrast Agent[E.4]

The experimental scheme presented in Figure E.4 has been designed by the authors of [E.4] to perform *in-vivo* optoacoustic spectroscopy measurements of a gold nanorod solution that is used as a lymph node tracer in a rat model. This experimental procedure has been devised to replace invasive surgeries.

The optical source used in this procedure was a Ti:sapphire laser pumped by a Q-switched Nd:YAG laser. The optical pulses have a temporal width of 10 ns at a pulse repetition rate of 10 Hz. It should be indicated that the optoacoustic spectroscopic measurements have been limited to three different wavelengths, these were 757 nm, 807 nm and 820 nm.

The fluctuations in the pulse energy, thus optoacoustic signals, have been corrected using a photodiode which has measured part of the output optical energy. The optical energy was guided to the rat model by means of two prisms. A concave lens, a spherical conical lens and an optical condenser were used to form ring shaped illumination. To generate the images, a motorized XY linear translation stage was used.

The detection of the optoacoustic transients was performed using a 5 MHz immersion resonant transducer (V308, Panametrics). This transducer has been placed below a water tank in contact with a thin clear membrane. The tank, filled with water, contains the rat model. To optimize the impedance matching between the sample, thin membrane and acoustic transducer, ultrasonic gel was used.

The analysis of the signals generated and detected using the acoustic transducer was carried out by measuring the amplitude of the optoacoustic signal. However no quantitative information regarding the optical properties of the nanorod contrast agent have been provided.

Figure E.4. (A) Schematic of an optoacoustic imaging system (B) image formation A-scan: 1-D image and B-scan: 2-D image. Multiple 2-D images form a 3-D image [24].

References Chapter 1

1.1. Bell, A.G., *The Production of Sound by Radiant Energy.* Science 1881. **2**: p. 242-253.

1.2. Rabasovic, M.D., M.G. Nikolic, M.D. Dramicanin, M. Franko, and D.D. Markushev, *Low-cost, portable photoacoustic setup for solid samples.* Measurement Science & Technology, 2009. **20**(9).

1.3. Tam, A.C. and C.K.N. Patel, *Optical absorption of light and heavy-water by laser optoacousitc spectroscopy.* Applied Optics, 1979. **18**(19): p. 3348-3358.

1.4. Santiago, G., V. Slezak, and A.L. Peuriot, *Resonant photoacoustic gas sensing by PC-based audio detection.* Applied Physics B-Lasers and Optics, 2003. **77**(4): p. 463-465.

1.5. Bijnen, F.G.C., F.J.M. Harren, J.H.P. Hackstein, and J. Reuss, *Intracavity CO laser photoacoustic trace gas detection: Cyclic CH4, H2O and CO2 emission by cockroaches and scarab beetles.* Applied Optics, 1996. **35**(27): p. 5357-5368.

1.6. Oraevsky, A.A., S.L. Jacques, and F.K. Tittel. *Determination of tissue optical properties by piezoelectric detection of laser-induced stress waves*. 1993: SPIE.

1.7. Wang, L.H., *Photoacoustic Imaging and Spectroscopy*. 1 ed. Optical Science and Engineering, ed. L. Wang. 2009: CRC Press.

1.8. Xu, M.H. and L.H.V. Wang, *Photoacoustic imaging in biomedicine.* Review of Scientific Instruments, 2006. **77**(4).

1.9. Oraevsky, A. and A. Karabutov, *Optoacoustic Tomography* in *Biomedical Photonics Hanbook*, T. Vo-Dinh, Editor. 2003, CRC Press. p. 34-1 34-34.

1.10. Tuchin, V., ed. *Tissue Optics*. 2000, SPIE Press: Washington.

1.11. Marbach, R., T. Koschinsky, F.A. Gries, and H.M. Heise, *Noninvasive blood-glucose assay by near-infrared diffuse-reflectance spectroscopy of the human inner lip.* Applied Spectroscopy, 1993. **47**(7): p. 875-881.

1.12. Bigio, I.J. and J.R. Mourant, *Ultraviolet and visible spectroscopies for tissue diagnostics: Fluorescence spectroscopy and elastic-scattering spectroscopy.* Physics in Medicine and Biology, 1997. **42**(5): p. 803-814.

1.13. Haka, A.S., Z. Volynskaya, J.A. Gardecki, J. Nazemi, R. Shenk, N. Wang, R.R. Dasari, M. Fitzmaurice, and M.S. Feld, *Diagnosing breast cancer using Raman spectroscopy: prospective analysis.* Journal of Biomedical Optics, 2009. **14**(5).

1.14. Laufer, J., C. Elwell, D. Delpy, and P. Beard, *In vitro measurements of absolute blood oxygen saturation using pulsed near-infrared photoacoustic spectroscopy: accuracy and resolution.* Physics in Medicine and Biology, 2005. **50**(18): p. 4409-4428.

1.15. Cheong, W.F., S.A. Prahl, and A.J. Welch, *A review of the optical-properties of biological tissues.* Ieee Journal of Quantum Electronics, 1990. **26**(12): p. 2166-2185.

1.16. Laufer, J., D. Delpy, C. Elwell, and P. Beard, *Quantitative spatially resolved measurement of tissue chromophore concentrations using photoacoustic spectroscopy: application to the measurement of blood oxygenation and haemoglobin concentration.* Physics in Medicine and Biology, 2007. **52**(1): p. 141-168.

1.17. Berger, A.J., T.-W. Koo, I. Itzkan, G. Horowitz, and M.S. Feld, *Multicomponent Blood Analysis by Near-Infrared Raman Spectroscopy.* Appl. Opt., 1999. **38**(13): p. 2916-2926.

1.18. Bevilacqua, F., A.J. Berger, A.E. Cerussi, D. Jakubowski, and B.J. Tromberg, *Broadband absorption spectroscopy in turbid media by combined frequency-domain and steady-state methods.* Applied Optics, 2000. **39**(34): p. 6498-6507.

1.19. Pham, T.H., R. Hornung, H.P. Ha, T. Burney, D. Serna, L. Powell, M. Brenner, and B.J. Tromberg, *Noninvasive monitoring of hemodynamic stress using quantitative near-infrared frequency-domain photon migration spectroscopy.* Journal of Biomedical Optics, 2002. **7**(1): p. 34-44.

1.20. Tromberg, B.J., N. Shah, R. Lanning, A. Cerussi, J. Espinoza, T. Pham, L. Svaasand, and J. Butler, *Non-invasive in vivo characterization of breast tumors using photon migration spectroscopy.* Neoplasia, 2000. **2**(1-2): p. 26-40.

1.21. Acedo, P., A. Garcia, V. Cunningham, H. Lamela, and J.O. SantoTomas, *Preliminary tests on a low-cost and compact optoelectronic system for optical mammography.* 2005. **5969**(1): p. 59691E.

1.22. Acedo, P., A. Garcia, V. Cunningham, H. Lamela, and J.O. SantoTomas, *Conception and description of a low-cost and compact optoelectronic frequency-domain system for optical mammography.* 2005. **5959**(1): p. 595903.

1.23. Tromberg, B.J., A. Cerussi, N. Shah, M. Compton, A. Durkin, D. Hsiang, J. Butler, and R. Mehta, *Imaging in breast cancer - Diffuse optics in breast cancer: detecting tumors in pre-menopausal women and monitoring neoadjuvant chemotherapy.* Breast Cancer Research, 2005. **7**(6): p. 279-285.

1.24. Mallidi, S., T. Larson, J. Aaron, K. Sokolov, and S. Emelianov, *Molecular specific optoacoustic imaging with plasmonic nanoparticles.* Optics Express, 2007. **15**(11): p. 6583-6588.

1.25. Wang, X., Y. Pang, G. Ku, X. Xie, G. Stoica, and L.V. Wang, *Noninvasive laser-induced photoacoustic tomography for structural and functional in vivo imaging of the brain.* Nat Biotech, 2003. **21**(7): p. 803-806.

1.26. Ermilov, S.A., T. Khamapirad, A. Conjusteau, M.H. Leonard, R. Lacewell, K. Mehta, T. Miller, and A.A. Oraevsky, *Laser optoacoustic imaging system for detection of breast cancer.* J Biomed Opt, 2009. **14**(2): p. 024007.

1.27. Brecht, H.P., R. Su, M. Fronheiser, S.A. Ermilov, A. Conjusteau, and A.A. Oraevsky, *Whole-body three-dimensional optoacoustic tomography system for small animals.* Journal of Biomedical Optics, 2009. **14**(6).

1.28. Brecht, H.-P., R. Su, M. Fronheiser, S.A. Ermilov, A. Conjusteau, A. Liopo, M. Motamedi, and A.A. Oraevsky. *Optoacoustic 3D whole-body tomography: experiments in nude mice*. 2009: SPIE.

1.29. Oraevsky, A.A., *Detection, diagnostics and image-guided therapy of cancer using laser optoacoustic imaging system and gold nanoparticles.* Apbp 2004: Second Asian and Pacific Rim Symposium on Biophotonics, Proceedings, 2004: p. 250-251.

1.30. Copland, J.A., M. Eghtedari, V.L. Popov, N. Kotov, N. Mamedova, M. Motamedi, and A.A. Oraevsky, *Bioconjugated gold nanoparticles as a molecular based contrast agent: implications for imaging of deep tumors using optoacoustic tomography.* Molecular Imaging & Biology, 2004. **6**(5): p. 341-349.

1.31. Lamela, H., V. Cunningham, P. Pedreira, D.C. Gallego, P. Acedo, W. Fritzsche, A. Csaki, G. Festag, and A. Steinbruk, *Comparative analysis of optical absorption and optoacoustic signal generation in nanoparticles.* 2008. **6856**: p. 68560L-10.

1.32. Lamela, H., V. Cunningham, P. Pedreira, D.C. Gallego, P. Acedo, W. Fritzsche, A. Csaki, G. Festag, and A. Steinbruk, *Analysis of the diffuse light and optoacoustic signal generation in nanoparticles.* 2007. **7022**(1): p. 702207.

1.33. Cunningham, V., H. Lamela, P. Pedreira, D. Gallego, P. Acedo, W. Fritzsche, A. Csaki, G. Festag, and A. Steinbruk, *Optoacoustic signal generation by using nanoparticles and nanorods for biomedical imaging.* The 2nd International Topical Meeting on Optical Sensing and Artifical Vision, OSAV 2008, Saint Petersburg, Russia., 2008.

1.34. Eghtedari, M., A. Oraevsky, J.A. Copland, N.A. Kotov, A. Conjusteau, and M. Motamedi, *High sensitivity of in vivo detection of gold nanorods using a laser optoacoustic imaging system.* Nano Letters, 2007. **7**: p. 1914-1918.

1.35. Song, K.H., C. Kim, K. Maslov, and L.V. Wang, *Noninvasive in vivo spectroscopic nanorod-contrast photoacoustic mapping of sentinel lymph nodes.* European Journal of Radiology, 2009. **70**(2): p. 227-231.

1.36. Taruttis, A., E. Herzog, D. Razansky, and V. Ntziachristos, *Real-time imaging of cardiovascular dynamics and circulating gold nanorods with multispectral optoacoustic tomography.* Opt. Express, 2010. **18**(19): p. 19592-19602.

1.37. Nelayah, J., M. Kociak, O. Stephan, N. Geuquet, L. Henrard, F.J.G. de Abajo, I. Pastoriza-Santos, L.M. Liz-Marzan, and C. Colliex, *Two-Dimensional Quasistatic Stationary Short Range Surface Plasmons in Flat Nanoprisms.* Nano Letters, 2010. **10**(3): p. 902-907.

1.38. Cunningham, V., H. Lamela, P. Pedreira, D. Gallego, and P. Acedo, *Gold nanoparticles as a contrast agent in photoacoustic imaging for cancer detection.* International Conference on Molecular Plasmonics 2007 , Jena, Germany, 2007.

1.39. Perez-Juste, J., I. Pastoriza-Santos, L.M. Liz-Marzan, and P. Mulvaney, *Gold nanorods: Synthesis, characterization and applications.* Coordination Chemistry Reviews, 2005. **249**(17-18): p. 1870-1901.

1.40. Cunningham, V., H. Lamela, A. Steinbruk, A. Csaki, and W. Fritzsche, *Synthesis and characterization of gold nanoparticles for enhanced absorption and optoacoustic signal generation.* The 6th International Conference on Photonics, Devices and Systems 2008, Prague, Czech Republic., 2008.

1.41. DasGupta, D., G. von Maltzahn, S. Ghosh, S.N. Bhatia, S.K. Das, and S. Chakraborty, *Probing nanoantenna-directed photothermal destruction of tumors using noninvasive laser irradiation.* Applied Physics Letters, 2009. **95**(23).

1.42. Cox, B.T., J.G. Laufer, and P.C. Beard. *The challenges for quantitative photoacoustic imaging*. 2009: SPIE.

1.43. Cox, B.T., J.G. Laufer, and P.C. Beard, *Quantitative photoacoustic image reconstruction using fluence dependentchromophores.* Biomed. Opt. Express, 2010. **1**(1): p. 201-208.

1.44. Laufer, J., E. Zhang, and P. Beard, *Evaluation of Absorbing Chromophores Used in Tissue Phantoms for Quantitative Photoacoustic Spectroscopy and Imaging.* Ieee Journal of Selected Topics in Quantum Electronics, 2010. **16**(3): p. 600-607.

1.45. Laufer, J., E. Zhang, B. Cox, and P. Beard, *Quantitative imaging of chromophore concentrations using a photoacoustic forward model - art. no. 68560Z.* Photons Plus Ultrasound: Imaging and Sensing 2008: The Ninth Conference on Biomedical Thermoacoustics, Optoacoustics, and Acoustic-Optics, 2008. **6856**: p. Z8560-Z8560.

1.46. Cunningham, V. and H. Lamela, *Optical and optoacoustic measurements of the absorption properties of spherical gold nanoparticles within a highly scattering medium.* Optics and Laser Technology, 2010. **42**(5): p. 769-774.

1.47. Lamela, H. and V. Cunningham, *Experimental Study using Optoacoustic Spectroscopy (OAS) on Spherical Gold Nanoparticles.* Optics and Laser Technology, 2010. **43**(1): p. 143-146.

1.48. Cunningham, V. and H. Lamela, *Laser optoacoustic spectroscopy (LOS) of gold nanorods within a highly scattering medium.* Optics Letters, 2010. **35**(20).

References Chapter 2

2.1. Wang, L.V. and H.I. Wu, *Biomedical Optics Principles and Imaging*. 2007, New Jersey: John Wiley & Sons.

2.2. Lamela, H., V. Cunningham, P. Pedreira, D.C. Gallego, P. Acedo, W. Fritzsche, A. Csaki, G. Festag, and A. Steinbruk, *Comparative analysis of optical absorption and optoacoustic signal generation in nanoparticles.* Proc. SPIE, 2008. **6856**: p. 68560L-10.

2.3. Oshtrakh, M.I., *Study of the relationship of small variations of the molecular structure and the iron state in iron containing proteins by Mossbauer spectroscopy: biomedical approach.* Spectrochimica Acta Part a-Molecular and Biomolecular Spectroscopy, 2004. **60**(1-2): p. 217-234.

2.4. Wallace, V.P., P.F. Taday, A.J. Fitzgerald, R.M. Woodward, J. Cluff, R.J. Pye, and D.D. Arnone, *Terahertz pulsed imaging and spectroscopy for biomedical and pharmaceutical applications.* Faraday Discussions, 2004. **126**: p. 255-263.

2.5. Wallace, V.P., E. MacPherson, A.J. Fitzgerald, T. Lo, E. Provenzano, S. Pinder, and A. Purushotham, *Terahertz pulsed imaging and spectroscopy of breast tumors.* Optical Methods in the Life Sciences, 2006. **6386**: p. U183-U190.

2.6. Sethuraman, S., J.H. Amirian, S.H. Litovsky, R.W. Smalling, and S.Y. Emelianov, *Spectroscopic intravascular photoacoustic imaging to differentiate atherosclerotic plaques.* Optics Express, 2008. **16**(5): p. 3362-3367.

2.7. Esenaliev, R.O., I.V. Larina, K.V. Larin, D.J. Deyo, M. Motamedi, and D.S. Prough, *Optoacoustic technique for noninvasive monitoring of blood oxygenation: a feasibility study.* Applied Optics, 2002. **41**(22): p. 4722-4731.

2.8. Savateeva, E.V., A.A. Karabutov, S.V. Solomatin, and A.A. Oraevsky, *Optical properties of blood at various levels of oxygenation studied by time resolved detection of laser-induced pressure profiles.* Biomedical Optoacoustics Iii, 2002. **4618**: p. 63-75.

2.9. Bednov, A., A. Karabutov, E. Savateeva, W. March, and A. Oraevsky, *Glucose monitoring in vivo by measuring laser-induced acoustic profiles.* Biomedical Optoacoustics, 2000. **1**(10): p. 9-18.

2.10. Kinnunen, M. and R. Myllyla, *Effect of glucose on photoacoustic signals at the wavelengths of 1064 and 532 nm in pig blood and intralipid.* Journal of Physics D-Applied Physics, 2005. **38**(15): p. 2654-2661.

2.11. Rozanova, N. and J.Z. Zhang, *Photothermal ablation therapy for cancer based on metal nanostructures.* Science in China Series B-Chemistry, 2009. **52**(10): p. 1559-1575.

2.12. Fortina, P., L.J. Kricka, D.J. Graves, J. Park, T. Hyslop, F. Tam, N.J. Halas, S. Surrey, and S.A. Waldman, *Applications of nanoparticles to diagnostics and therapeutics in colorectal cancer.* Trends in Biotechnology, 2007. **25**(4): p. 145-152.

2.13. Huang, X.H., P.K. Jain, I.H. El-Sayed, and M.A. El-Sayed, *Gold nanoparticles: interesting optical properties and recent applications in cancer diagnostic and therapy.* Nanomedicine, 2007. **2**: p. 681-693.

2.14. Zhao, Z.M. and R. Myllyla, *The effects of optical scattering on pulsed photoacoustic measurement in weakly absorbing liquids.* Measurement Science & Technology, 2001. **12**(12): p. 2172-2177.

2.15. Tuchin, V., ed. *Tissue Optics*. 2000, SPIE Press: Washington.

2.16. Oraevsky, A.A., S.L. Jacques, and F.K. Tittel, *Measurement of tissue optical properties by time-resolved detection of laser-induced transient stress.* Applied Optics, 1997. **36**(1): p. 402-415.

2.17. Heusmann, H., J.G. Koelzer, and G. Mitic, *Characterization of female breasts in vivo by time-resolved and spectroscopic measurements in the near infrared spectroscopy.* Journal of Biomedical Optics, 1996. **1**(4): p. 425-434.

2.18. Fantini, S., S.A. Walker, M.A. Franceschini, M. Kaschke, P.M. Schlag, and K.T. Moesta, *Assessment of the size, position, and optical properties of breast tumors in vivo by noninvasive optical methods.* Applied Optics, 1998. **37**(10): p. 1982-1989.

2.19. Peters, V.G., D.R. Wyman, M.S. Patterson, and G.L. Frank, *Optical properties of normal and diseased human breast tissues in the visible and near-infrared.* Physics in Medicine and Biology, 1990. **35**(9): p. 1317-1334.

2.20. Durduran, T., R. Choe, W.B. Baker, and A.G. Yodh, *Diffuse optics for tissue monitoring and tomography.* Reports on Progress in Physics, 2010. **73**(7).

2.21. Vo-Dinh, T., *Biomedical Photonics*, in *Biomedical Photonics*, T. Vo-Dinh, Editor. 2003, CRC Press.

2.22. Emelianov, S.Y., S.R. Aglyamov, A.B. Karpiouk, S. Mallidi, S. Park, S. Sethuraman, J. Sbah, R.W. Smalling, J.M. Rubin, and W.G. Scott, *Synergy and Applications of Combined Ultrasound, Elasticity, and Photoacoustic Imaging.* 2006 Ieee Ultrasonics Symposium, Vols 1-5, Proceedings, 2006: p. 405-415.

2.23. Tam, A.C. and C.K.N. Patel, *Optical absorption of light and heavy-water by laser optoacousitc spectroscopy.* Applied Optics, 1979. **18**(19): p. 3348-3358.

2.24. Conway, J.M., K.H. Norris, and C.E. Bodwell, *A new approach for the estimation of body-composition - infrared interactance.* American Journal of Clinical Nutrition, 1984. **40**(6): p. 1123-1130.

2.25. Gusev, V.E. and A. Karabutov, *Laser Optoacoustics*. 1993, New York: American Institute of Physics.

2.26. Allen, T.J., B.T. Cox, and P.C. Beard, *Generating photoacoustic signals using high-peak power pulsed laser diodes.* Photons Plus Ultrasound: Imaging and Sensing 2005, 2005. **5697**: p. 233-242.

2.27. Esenaliev, R.O., A.A. Karabutov, and A.A. Oraevsky, *Sensitivity of laser opto-acoustic imaging in detection of small deeply embedded tumors.* Ieee Journal of Selected Topics in Quantum Electronics, 1999. **5**(4): p. 981-988.

2.28. Xu, M.H. and L.H.V. Wang, *Photoacoustic imaging in biomedicine.* Review of Scientific Instruments, 2006. **77**(4).

2.29. DiMarzio, C.A. and T.W. Murray, *Medical Imaging Techniques Combining Light and Ultrasound.* Subsurface Sensing Technologies and Applications, 2003. **4**(4): p. 289-309.

2.30. Oraevsky, A. and A. Karabutov, *Optoacoustic Tomography* in *Biomedical Photonics Hanbook*, T. Vo-Dinh, Editor. 2003, CRC Press. p. 34-1 34-34.

2.31. Kumar, S. and V.B. Singh, *Pseudo-Gruneisen parameter of organic liquids* Indian Journal of Pure & Applied Physics, 1992. **30**(3): p. 89-93.

2.32. Xu, M.H. and L.H.V. Wang, *Pulsed-microwave-induced thermoacoustic tomography: Filtered backprojection in a circular measurement configuration.* Medical Physics, 2002. **29**(8): p. 1661-1669.

2.33. Oraevsky, A.A. and A.A. Karabutov, *Ultimate sensitivity of time-resolved optoacoustic detection.* SPIE, 2000. **3916**(1): p. 228-239.

2.34. Cunningham, V. and H. Lamela, *Efficient combination of multiple high power semiconductor laser sources for photoacoustic signal generation in biomedical phantoms - art. no. 619106.* Biophotonics and New Therapy Frontiers, Proc. SPIE, 2006. **6191**: p. 19106-19106.

2.35. Cunningham, V. and H. Lamela, *Laser optoacoustic spectroscopy (LOS) of gold nanorods within a highly scattering medium.* Optics Letters, 2010. **35**(20).

2.36. Lamela, H. and V. Cunningham, *Experimental Study using Optoacoustic Spectroscopy (OAS) on Spherical Gold Nanoparticles.* Optics and Laser Technology, 2010. **43**(1): p. 143-146.

2.37. Eghtedari, M., A. Oraevsky, J.A. Copland, N.A. Kotov, A. Conjusteau, and M. Motamedi, *High sensitivity of in vivo detection of gold nanorods using a laser optoacoustic imaging system.* Nano Letters, 2007. **7**: p. 1914-1918.

2.38. Wang, Y., X. Xie, X. Wang, G. Ku, K.L. Gill, D.P. O'Neal, G. Stoica, and L.V. Wang, *Photoacoustic Tomography of a Nanoshell Contrast Agent in the in Vivo Rat Brain.* Nano Letters, 2004. **4**(9): p. 1689-1692.

References Chapter 3

3.1. Zsigmondy R., T.P.A., *Das Kolloid Gold.* Akad. Verlag, Leipzig, 1925.

3.2. Turkevich, J., *Colloidal Gold. Part I.* Gold Bull., 1985. **18**(3): p. 86 - 91.

3.3. Faraday, M., *The Bakerian Lecture: Experimental Relations of Gold (and Other Metals) to Light.* Philosophical Transactions of the Royal Society of London, 1857. **147**(ArticleType: primary_article / Full publication date: 1857 / Copyright © 1857 The Royal Society): p. 145-181.

3.4. Yguerabide, J. and E.E. Yguerabide, *Light-scattering submicroscopic particles as highly fluorescent analogs and their use as tracer labels in clinical and biological applications - I. Theory.* Analytical Biochemistry, 1998. **262**(2): p. 137-156.

3.5. Yguerabide, J. and E.E. Yguerabide, *Light-scattering submicroscopic particles as highly fluorescent analogs and their use as tracer labels in clinical and biological applications - II. Experimental characterization.* Analytical Biochemistry, 1998. **262**(2): p. 157-176.

3.6. Perez-Juste, J., A. Mulvaney, and L.M. Liz-Martan, *Patterning and encryption using gold nanoparticles.* International Journal of Nanotechnology, 2007. **4**(3): p. 215-225.

3.7. Jain, P.K., K.S. Lee, I.H. El-Sayed, and M.A. El-Sayed, *Calculated absorption and scattering properties of gold nanoparticles of different size, shape, and composition: Applications in biological imaging and biomedicine.* Journal of Physical Chemistry B, 2006. **110**(14): p. 7238-7248.

3.8. Myroshnychenko, V., J. Rodriguez-Fernandez, I. Pastoriza-Santos, A.M. Funston, C. Novo, P. Mulvaney, L.M. Liz-Marzan, and F.J.G. de Abajo, *Modelling the optical response of gold nanoparticles.* Chemical Society Reviews, 2008. **37**(9): p. 1792-1805.

3.9. Perez-Juste, J., I. Pastoriza-Santos, L.M. Liz-Marzan, and P. Mulvaney, *Gold nanorods: Synthesis, characterization and applications.* Coordination Chemistry Reviews, 2005. **249**(17-18): p. 1870-1901.

3.10. Purcell, E.M. and Pennypac.Cr, *Scattering and absorption of light by nonspherical dielectric grains.* Astrophysical Journal, 1973. **186**(2): p. 705-714.

3.11. Nelayah, J., M. Kociak, O. Stephan, N. Geuquet, L. Henrard, F.J.G. de Abajo, I. Pastoriza-Santos, L.M. Liz-Marzan, and C. Colliex, *Two-Dimensional Quasistatic Stationary Short Range Surface Plasmons in Flat Nanoprisms.* Nano Letters, 2010. **10**(3): p. 902-907.

3.12. Hao, E., G.C. Schatz, and J.T. Hupp, *Synthesis and optical properties of anisotropic metal nanoparticles.* Journal of Fluorescence, 2004. **14**(4): p. 331-341.

3.13. Huang, X.H., S. Neretina, and M.A. El-Sayed, *Gold Nanorods: From Synthesis and Properties to Biological and Biomedical Applications.* Advanced Materials, 2009. **21**(48): p. 4880-4910.

3.14. Johnson, P.B. and R.W. Christy, *Optical - constants of noble-metals.* Physical Review B, 1972. **6**(12): p. 4370-4379.

3.15. Weaver, J.H. and H.P.R. Frederikse, *Optical Properties of Selected Elements*, in *CRC Hanbook of Chemistry and Physics*, D.R. Lide, Editor. 2009, CRC Press. p. 12-123 12-147.

3.16. Cox, A.J., A.J. DeWeerd, and J. Linden, *An experiment to measure Mie and Rayleigh total scattering cross sections.* American Journal of Physics, 2002. **70**(6): p. 620-625.

3.17. Turkevich, J., P.C. Stevenson, and J. Hillier, *The formation of colloidal gold.* Journal of Physical Chemistry, 1953. **57**(7): p. 670-673.

3.18. Turkevich, J., P.C. Stevenson, and J. Hillier, *A study of the nucleation and growth processes in the synthesis of colloidal gold.* Discussions of the Faraday Society, 1951(11): p. 55-&.

3.19. Link, S., M.B. Mohamed, and M.A. El-Sayed, *Simulation of the optical absorption spectra of gold nanorods as a function of their aspect ratio and the effect of the medium dielectric constant.* Journal of Physical Chemistry B, 1999. **103**(16): p. 3073-3077.

3.20. van der Zande, B.M.I., L. Pages, R.A.M. Hikmet, and A. van Blaaderen, *Optical properties of aligned rod-shaped gold particles dispersed in poly(vinyl alcohol) films.* Journal of Physical Chemistry B, 1999. **103**(28): p. 5761-5767.

3.21. Ungureanu, C., R.G. Rayavarapu, S. Manohar, and T.G. van Leeuwen, *Discrete dipole approximation simulations of gold nanorod optical properties: Choice of input parameters and comparison with experiment.* Journal of Applied Physics, 2009. **105**(10).

References Chapter 4

4.1. Oraevsky, A. and A. Karabutov, *Optoacoustic Tomography* in *Biomedical Photonics Hanbook*, T. Vo-Dinh, Editor. 2003, CRC Press. p. 34-1 34-34.

4.2. Oraevsky, A.A., *Detection, diagnostics and image-guided therapy of cancer using laser optoacoustic imaging system and gold nanoparticles.* Apbp 2004: Second Asian and Pacific Rim Symposium on Biophotonics, Proceedings, 2004: p. 250-251.

4.3. Wang, X., Y. Pang, G. Ku, X. Xie, G. Stoica, and L.V. Wang, *Noninvasive laser-induced photoacoustic tomography for structural and functional in vivo imaging of the brain.* Nat Biotech, 2003. **21**(7): p. 803-806.

4.4. Lamela, H., V. Cunningham, C. Macia-Sanahuja, J.A.G. Souto, and P. Acedo, *Analysis of photoacoustic signal frequencies in deep tissue phantoms using high-sensitive interferometric optical sensors.* Proc. SPIE, 2006. **6086**(1): p. 60861O.

4.5. Oraevsky, A.A., S.L. Jacques, and F.K. Tittel, *Measurement of tissue optical properties by time-resolved detection of laser-induced transient stress.* Applied Optics, 1997. **36**(1): p. 402-415.

4.6. Esenaliev, R.O., I.V. Larina, K.V. Larin, D.J. Deyo, M. Motamedi, and D.S. Prough, *Optoacoustic technique for noninvasive monitoring of blood oxygenation: a feasibility study.* Applied Optics, 2002. **41**(22): p. 4722-4731.

4.7. Song, K.H., C. Kim, K. Maslov, and L.V. Wang, *Noninvasive in vivo spectroscopic nanorod-contrast photoacoustic mapping of sentinel lymph nodes.* European Journal of Radiology, 2009. **70**(2): p. 227-231.

4.8. Firbank, M. and D.T. Delpy, *A design for a stable and reproducible phantom for use in near-infrared imaging and spectroscopy.* Physics in Medicine and Biology, 1993. **38**(6): p. 847-853.

4.9. Firbank, M., M. Oda, and D.T. Delpy, *An improved design for a stable and reproducible phantom material for use in near-infrared spectroscopy and imaging* Physics in Medicine and Biology, 1995. **40**(5): p. 955-961.

4.10. Wang, L.H. and X.M. Zhao, *Ultrasound-modulated optical tomography of absorbing objects buried in dense tissue-simulating turbid media.* Applied Optics, 1997. **36**(28): p. 7277-7282.

4.11. Ma, R., A. Taruttis, V. Ntziachristos, and D. Razansky, *Multispectral optoacoustic tomography (MSOT) scanner for whole-body small animal imaging.* Opt. Express, 2009. **17**(24): p. 21414-21426.

4.12. Razansky, D., M. Distel, C. Vinegoni, R. Ma, N. Perrimon, R.W. Koster, and V. Ntziachristos, *Multispectral opto-acoustic tomography of deep-seated fluorescent proteins in vivo.* Nat Photon, 2009. **3**(7): p. 412-417.

4.13. Laufer, J., E. Zhang, and P. Beard, *Evaluation of Absorbing Chromophores Used in Tissue Phantoms for Quantitative Photoacoustic Spectroscopy and Imaging.* Ieee Journal of Selected Topics in Quantum Electronics, 2010. **16**(3): p. 600-607.

4.14. Michels, R., F. Foschum, and A. Kienle, *Optical properties of fat emulsions.* Opt. Express, 2008. **16**(8): p. 5907-5925.

4.15. Su, J.L.S., B. Wang, and S.Y. Emelianov, *Photoacoustic imaging of coronary artery stents.* Optics Express, 2009. **17**(22): p. 19894-19901.

4.16. Rajian, J.R., P.L. Carson, and X.D. Wang, *Quantitative photoacoustic measurement of tissue optical absorption spectrum aided by an optical contrast agent.* Optics Express, 2009. **17**(6): p. 4879-4889.

4.17. Liu, T.-Y., S.-W. Huang, and H.K. Chiang, *Synthetic Aperture Photoacoustic Imaging on Small Vessel Phantom Study.* Journal of Medical and Biological Engineering, 2005. **25**(4): p. 179 - 183.

4.18. Cunningham, V. and H. Lamela, *Optical and optoacoustic measurements of the absorption properties of spherical gold nanoparticles within a highly scattering medium.* Optics and Laser Technology, 2010. **42**(5): p. 769-774.

4.19. Cunningham, V. and H. Lamela, *Laser optoacoustic spectroscopy (LOS) of gold nanorods within a highly scattering medium.* Optics Letters, 2010. **35**(20).

4.20. Pravdin, A.B., S.P. Chernova, T.G. Papazoglou, and V. Tuchin, *Tissue Phantoms*, in *Handbook of Biomedical Diagnostics*, V. Tuchin, Editor. 2002, SPIE Press Book. p. 1110.

4.21. Wabnitz, H. and H. Rinneberg, *Imaging in turbid media by photon density waves: spatial resolution and scaling relations.* Appl. Opt., 1997. **36**(1): p. 64-74.

4.22. Li, H. and L.V. Wang, *Autocorrelation of scattered laser light for ultrasound-modulated optical tomography in dense turbid media.* Applied Optics, 2002. **41**(22): p. 4739-4742.

4.23. Wang, L.H. and S.L. Jacques, *Error estimation of measureing total interaction coefficients of turbid media using collimated light transmission* Physics in Medicine and Biology, 1994. **39**(12): p. 2349-2354.

4.24. Acedo, P., A. Garcia, V. Cunningham, H. Lamela, and J.O. SantoTomas, *Preliminary tests on a low-cost and compact optoelectronic system for optical mammography.* Proc. SPIE, 2005. **5969**(1): p. 59691E.

References Chapter 5

5.1. Allen, T.J., B.T. Cox, and P.C. Beard, *Generating photoacoustic signals using high-peak power pulsed laser diodes.* Photons Plus Ultrasound: Imaging and Sensing 2005, 2005. **5697**: p. 233-242.

5.2. Beard, P.C., F. Perennes, E. Draguioti, and T.N. Mills, *Optical fiber photoacoustic-photothermal probe.* Optics Letters, 1998. **23**(15): p. 1235-1237.

5.3. Vaithilingam, S., I.O. Wygant, P.S. Kuo, X.F. Zhuang, O. Oralkan, P.D. Olcott, and B.T. Khuri-Yakub, *Capacitive micromachined ultrasonic transducers (CMUTs) for photoacoustic imaging - art. no. 608603.* Photons Plus Ultrasound: Imaging and Sensing 2006, 2006. **6086**: p. 8603-8603.

5.4. Funke, A.R., J.F. Aubry, M. Fink, A.C. Boccara, and E. Bossy, *Photoacoustic guidance of high intensity focused ultrasound with selective optical contrasts and time-reversal.* Applied Physics Letters, 2009. **94**(5).

5.5. Razansky, D., M. Distel, C. Vinegoni, R. Ma, N. Perrimon, R.W. Koster, and V. Ntziachristos, *Multispectral opto-acoustic tomography of deep-seated fluorescent proteins in vivo.* Nat Photon, 2009. **3**(7): p. 412-417.

5.6. Lamela, H., V. Cunningham, P. Pedreira, D.C. Gallego, P. Acedo, W. Fritzsche, A. Csaki, G. Festag, and A. Steinbruk, *Comparative analysis of optical absorption and optoacoustic signal generation in nanoparticles.* Proc. SPIE, 2008. **6856**: p. 68560L-10.

5.7. Dodgson, J.T., A. Mandelis, and C. Andreetta, *Optical-absorption coefficient measurements in solids and liquids using correlation photoacoustic-spectroscopy.* Canadian Journal of Physics, 1986. **64**(9): p. 1074-1080.

5.8. Turkevich, J., P.C. Stevenson, and J. Hillier, *A study of the nucleation and growth processes in the synthesis of colloidal gold.* Discussions of the Faraday Society, 1951(11): p. 55-&.

5.9. Jain, P.K., K.S. Lee, I.H. El-Sayed, and M.A. El-Sayed, *Calculated absorption and scattering properties of gold nanoparticles of different size, shape, and composition: Applications in biological imaging and biomedicine.* Journal of Physical Chemistry B, 2006. **110**(14): p. 7238-7248.

5.10. Karabutov, A.A., I.M. Pelivanov, N.B. Podymova, and S.E. Skipetrov, *Determination of the optical characteristics of turbid media by the laser optoacoustic method.* Quantum Electronics, 1999. **29**(12): p. 1054-1059.

5.11. Tuchin, V., ed. *Tissue Optics*. 2000, SPIE Press: Washington.

5.12. Lamela, H., V. Cunningham, C. Macia-Sanahuja, J.A.G. Souto, and P. Acedo, *Analysis of photoacoustic signal frequencies in deep tissue phantoms using high-sensitive interferometric optical sensors.* Proc. SPIE, 2006. **6086**(1): p. 60861O.

5.13. Cunningham, V. and H. Lamela, *Optical and optoacoustic measurements of the absorption properties of spherical gold nanoparticles within a highly scattering medium.* Optics and Laser Technology, 2010. **42**(5): p. 769-774.

5.14. Oraevsky, A. and A. Karabutov, *Optoacoustic Tomography* in *Biomedical Photonics Hanbook*, T. Vo-Dinh, Editor. 2003, CRC Press. p. 34-1 34-34.

5.15. Oraevsky, A.A., A.A. Karabutov, S.V. Solomatin, E.V. Savateeva, V.G. Andreev, Z. Gatalica, H. Singh, and R.D. Fleming, *Laser optoacoustic imaging of breast cancer in vivo.* Biomedical Optoacoustics Ii, 2001. **2**(13): p. 6-15.

5.16. Joshi, N., C. Donner, and H.W. Jensen, *Noninvasive measurement of scattering anisotropy in turbid materials by nonnormal incident illumination.* Optics Letters, 2006. **31**(7): p. 936-938.

References Chapter 6

6.1. Song, K.H., C. Kim, K. Maslov, and L.V. Wang, *Noninvasive in vivo spectroscopic nanorod-contrast photoacoustic mapping of sentinel lymph nodes.* European Journal of Radiology, 2009. **70**(2): p. 227-231.

6.2. Laufer, J., E. Zhang, and P. Beard, *Quantitative in vivo measurements of blood oxygen saturation using multiwavelength photoacoustic imaging - art. no. 64371Z.* Photons Plus Ultrasound: Imaging and Sensing 2007, 2007. **6437**: p. Z4371-Z4371.

6.3. Beard, P.C., *Interrogation of free-space Fabry-Perot sensing interferometers by angle tuning.* Measurement Science & Technology, 2003. **14**(11): p. 1998-2005.

6.4. Huang, X.H., P.K. Jain, I.H. El-Sayed, and M.A. El-Sayed, *Gold nanoparticles: interesting optical properties and recent applications in cancer diagnostic and therapy.* Nanomedicine, 2007. **2**: p. 681-693.

6.5. Haiss, W., N.T.K. Thanh, J. Aveyard, and D.G. Fernig, *Determination of size and concentration of gold nanoparticles from UV-Vis spectra.* Analytical Chemistry, 2007. **79**(11): p. 4215-4221.

6.6. Link, S. and M.A. El-Sayed, *Size and temperature dependence of the plasmon absorption of colloidal gold nanoparticles.* Journal of Physical Chemistry B, 1999. **103**(21): p. 4212-4217.

6.7. Ganeev, R.A., M. Baba, A.I. Ryasnyansky, M. Suzuki, and H. Kuroda, *Characterization of optical and nonlinear optical properties of silver nanoparticles prepared by laser ablation in various liquids.* Optics Communications, 2004. **240**(4-6): p. 437-448.

6.8. Letfullin, R.R., C. Joenathan, T.F. George, and V.P. Zharov, *Laser-induced explosion of gold nanoparticles: potential role for nanophotothermolysis of cancer.* Nanomedicine, 2006. **1**(4): p. 473-480.

6.9. Larina, I.V., K.V. Larin, and R.O. Esenaliev, *Real-time optoacoustic monitoring of temperature in tissues.* Journal of Physics D-Applied Physics, 2005. **38**(15): p. 2633-2639.

6.10. Emelianov, S.Y., P.C. Li, and M. O'Donnell, *Photoacoustics for molecular imaging and therapy.* Physics Today, 2009. **62**(5): p. 34-39.

6.11. Xu, M.H. and L.H.V. Wang, *Pulsed-microwave-induced thermoacoustic tomography: Filtered backprojection in a circular measurement configuration.* Medical Physics, 2002. **29**(8): p. 1661-1669.

6.12. Kumar, S. and V.B. Singh, *Pseudo-Gruneisen parameter of organic liquids* Indian Journal of Pure & Applied Physics, 1992. **30**(3): p. 89-93.

6.13. Lamela, H. and V. Cunningham, *Experimental Study using Optoacoustic Spectroscopy (OAS) on Spherical Gold Nanoparticles.* Optics and Laser Technology, 2010. **43**(1): p. 143-146.

6.14. Cunningham, V. and H. Lamela, *Laser optoacoustic spectroscopy (LOS) of gold nanorods within a highly scattering medium.* Optics Letters, 2010. **35**(20).

References Appendix A

A.1. Valery, T., *Tissue Optics*. 2007: SPIE Press.

A.2. Cheong, W.F., S.A. Prahl, and A.J. Welch, *A review of the optical-properties of biological tissues.* Ieee Journal of Quantum Electronics, 1990. **26**(12): p. 2166-2185.

A.3. Oraevsky, A.A., et al., *Laser optoacoustic imaging of breast cancer in vivo.* Biomedical Optoacoustics Ii, 2001. **2**(13): p. 6-15.

A.4. Ermilov, S.A., et al., *Laser optoacoustic imaging system for detection of breast cancer.* J Biomed Opt, 2009. **14**(2): p. 024007.

A.5. Ermilov, S.A., et al., *128-channel laser optoacoustic imaging system (LOIS-128) for breast cancer diagnostics - art. no. 608609.* Photons Plus Ultrasound: Imaging and Sensing 2006, 2006. **6086**: p. 8609-8609.

A.6. Suzuki, K., et al., *Quantitative measurement of optical parameters in normal breasts using time-resolved spectroscopy: in vivo results of 30 Japanese women.* Journal of Biomedical Optics, 1996. **1**(3): p. 330-334.

A.7. Heusmann, H., J.G. Koelzer, and G. Mitic, *Characterization of female breasts in vivo by time-resolved and spectroscopic measurements in the near infrared spectroscopy.* Journal of Biomedical Optics, 1996. **1**(4): p. 425-434.

A.8. Key, H., et al., *Optical attenuation characteristics of breast tissue at visible and near-infrared wavelengths* Physics in Medicine and Biology, 1991. **36**(5): p. 579-590.

A.9. Driver, I., C.P. Lowdell, and D.V. Ash, *In vivo measurement of the optical interaction coefficients of human tumors at 630 nm.* Physics in Medicine and Biology, 1991. **36**(6): p. 805-813.

A.10. Vo-Dinh, T., *Biomedical Photonics*, in *Biomedical Photonics*, T. Vo-Dinh, Editor. 2003, CRC Press.

A.11. Saloma, C., C. Palmes-Saloma, and H. Kondoh, *Site-specific confocal fluorescence imaging of biological microstructures in a turbid medium.* Physics in Medicine and Biology, 1998. **43**(6): p. 1741-1759.

References Appendix B

B.1. Cunningham, V. and H. Lamela, *Efficient combination of multiple high power semiconductor laser sources for photoacoustic signal generation in biomedical phantoms - art. no. 619106.* Biophotonics and New Therapy Frontiers, 2006. **6191**: p. 19106-19106.

B.2. Pifferi, A., et al., *Four-wavelength time-resolved optical mammography in the 680 980-nm range.* Opt. Lett., 2003. **28**(13): p. 1138-1140.

B.3. Zeng, L., et al. *Design of a portable noninvasive photoacoustic glucose monitoring system integrated laser diode excitation with annular array detection*. 2008: SPIE.

B.4. Allen, T.J., B.T. Cox, and P.C. Beard, *Generating photoacoustic signals using high-peak power pulsed laser diodes.* Photons Plus Ultrasound: Imaging and Sensing 2005, 2005. **5697**: p. 233-242.

B.5. Esenaliev, R.O., et al., *Continuous, Noninvasive Monitoring of Total Hemoglobin Concentration by an Optoacoustic Technique.* Appl. Opt., 2004. **43**(17): p. 3401-3407.

References Appendix C

C.1. Bohren, C.F. and D.R. Huffman, *Absorption and scattering of light by small particles*, ed. J.W.a. Sons. 1983, New York.

References Appendix D

D.1. Turkevich, J., P.C. Stevenson, and J. Hillier, *The formation of colloidal gold.* Journal of Physical Chemistry, 1953. **57**(7): p. 670-673.

D.2. Turkevich, J., P.C. Stevenson, and J. Hillier, *A study of the nucleation and growth processes in the synthesis of colloidal gold.* Discussions of the Faraday Society, 1951(11): p. 55-&.

D.3. Frens, G., *Controlled nucleation for regulation of particle-size in monodisperse gold suspensions.* Nature-Physical Science, 1973. **241**(105): p. 20-22.

References Appendix E

E.1. Laufer, J., et al., *Quantitative spatially resolved measurement of tissue chromophore concentrations using photoacoustic spectroscopy: application to the measurement of blood oxygenation and haemoglobin concentration.* Physics in Medicine and Biology, 2007. **52**(1): p. 141-168.

E.2. Beard, P.C., *Interrogation of free-space Fabry-Perot sensing interferometers by angle tuning.* Measurement Science & Technology, 2003. **14**(11): p. 1998-2005.

E.3. Laufer, J., E. Zhang, and P. Beard, *Evaluation of Absorbing Chromophores Used in Tissue Phantoms for Quantitative Photoacoustic Spectroscopy and*

Imaging. Ieee Journal of Selected Topics in Quantum Electronics, 2010. **16**(3): p. 600-607.

E.4. Song, K.H., et al., *Noninvasive in vivo spectroscopic nanorod-contrast photoacoustic mapping of sentinel lymph nodes.* European Journal of Radiology, 2009. **70**(2): p. 227-231.